# A Parity-Violating Spin Rotation Measurement of Transversely Polarized Cold Neutrons Through a Liquid Helium Target

by Kangfei Gan

B.S. in Physics, June 2001, Fudan University

M.Phil. in Physics, May 2008, The George Washington University

A Dissertation submitted to
The Faculty of
The Columbian College of Arts and Sciences
of The George Washington University
in partial fulfillment of the requirements for the degree of
*Doctor of Philosophy*

May 15, 2011

Dissertation directed by

Allena K. Opper
Associate Professor of Physics

The Columbian College of Arts and Sciences of The George Washington University certifies that Kangfei Gan has passed the Final Examination for the degree of Doctor of Philosophy as of January 25, 2011. This is the final and approved form of the dissertation.

# A Parity-Violating Spin Rotation Measurement of Transversely Polarized Cold Neutrons Through a Liquid Helium Target

Kangfei Gan

Dissertation Research Committee:

Allena K. Opper, Associate Professor of Physics, Dissertation Director

Harald W. Grießhammer, Assistant Professor of Physics, Committee Member

Gerald Feldman, Professor of Physics, Committee Member

# Acknowledgements

It's such a pleasure to finally finish my Ph.D. dissertation by writing this page. I would like to thank my advisor, Professor Allena Opper, for reading my numerous revisions and providing feedback. This dissertation would not have been possible without her guidance and motivation through all the years.

I want to thank all our collaborators. Thanks to Professor Mike Snow for organizing the Neutron Spin Rotation collaboration, so that I had a dissertation project to join in the first place. I'm grateful to have Dr. Jeff Nico as my supervisor when I was stationed at NIST. This experiment could not have run without him. I would like to thank Diane Markoff, who worked on the first generation experiment so we have a lot to build on. I also want to thank Chris Bass, Da Luo and Anna Micherdzinska for their help when they worked with me at NIST. And I want to thank Murad Sarsour and Bret Crawford for working with me on the simulation project.

I would like to thank Professors Harald Grießhammer, Gerald Feldman, William Briscoe and Elizabeth Beise for serving on my dissertation committee. Thanks to the readers, Harald and Jerry, for providing feedback to improve my dissertation.

I have to say sorry to my parents for being so far away from home, and to my wife, BeiBei, for making her cross the ocean to be with me. She always offered her support and encouragement during the long writing process of my dissertation.

# Abstract of Dissertation

A Parity-Violating Spin Rotation Measurement of Transversely Polarized Cold Neutrons Through a Liquid Helium Target

The nucleon-nucleon (NN) weak interaction is one of the more poorly understood areas of the Standard Model. A quantitative description of the NN interaction is needed to describe weak interaction phenomenon in atomic, nuclear, and hadronic systems. This Ph.D. dissertation is based on a high precision measurement of the parity-violating (PV) spin rotation for transversely polarized cold neutrons passing through a liquid $^4$He target, which will support a quantitative interpretation of the NN weak interaction. The PV rotation angle was measured to be $d\phi/dz = (5.8 \pm 8.7(stat) \pm 1.3(sys)) \times 10^{-7}$ rad/m. This result is the most precise PV spin rotation measurement to date and the uncertainty is smaller than current estimates of the range of possible values of $d\phi/dz$ in the n-$^4$He system.

My contribution to the experiment includes (1) constructing a feedback system for active shielding of magnetic fields, (2) taking and analyzing data for both production and systematic effect measurements, and (3) expanding the Monte-Carlo simulation to study systematic effects from neutron scattering and magnetic fields.

# Contents

Acknowledgements . . . iii
Abstract of Dissertation . . . iv
List of Figures . . . viii
List of Tables . . . xv

**1 Introduction and Theoretical Background 1**
1.1 Introduction . . . 1
1.2 Theoretical Background . . . 2
1.2.1 Parity-violating nucleon-nucleon (NN) weak interaction . . . 2
1.2.2 Experimental studies of weak NN interaction . . . 5
1.2.3 Neutron spin rotation theory . . . 7

**2 Experimental Overview 12**
2.1 Apparatus overview . . . 12
2.2 NCNR cold neutron beam and beam guide . . . 17
2.3 Supermirror polarizer and analyzer . . . 18
2.4 Input coil . . . 19
2.5 Spin coil . . . 22
2.6 Cryostat and liquid helium target . . . 23
2.7 $\pi$-coil . . . 24
2.8 Output coil . . . 27
2.9 Ion chamber . . . 28

**3 Magnetic Compensation System** **32**
3.1 Overview of the compensation system . . . . . 32
3.2 The compensation coil, fluxgate sensor and magnetometer . . . . . 34
3.3 The difference amplifier . . . . . 36
3.4 The proportional-integral-derivative (PID) controller . . . . . 36
3.5 The result of compensation . . . . . 37

**4 Data Measurements** **39**
4.1 Characterization of the neutron beam . . . . . 39
4.1.1 Initial neutron spectrum . . . . . 39
4.1.2 Spatial distribution of neutron intensity . . . . . 40
4.1.3 Neutron fluence measurement . . . . . 41
4.1.4 Polarimeter measurements . . . . . 43
4.2 Data acquisition and control with the liquid $^4$He target . . . . . 43
4.3 Polarization product runs with liquid $^4$He . . . . . 46

**5 Data Analysis** **50**
5.1 Raw parity-non-conserving angle (PNCA) analysis . . . . . 50
5.1.1 From count-rate asymmetry to PNCA . . . . . 50
5.1.2 Identifying and removing data with non-zero target asymmetry (TA) 52
5.1.3 Preliminary PNCA results for the liquid $^4$He target . . . . . 52
5.2 Regression technique with internal magnetic field drift . . . . . 55
5.3 Application of polarization product . . . . . 58

**6 Computer Simulation** **63**
6.1 Introduction . . . . . 63
6.2 Neutron transport and spin rotation calculation . . . . . 64
6.3 Scattering in the liquid $^4$He target . . . . . 67
6.4 Ion chamber detector simulation . . . . . 70

**7 Systematic Effects** **72**

7.1 Analytical calculation and estimation . . . . . 74

7.1.1 Diamagnetism of liquid $^4$He . . . . . 74

7.1.2 Optical potential of liquid $^4$He . . . . . 74

7.1.3 Shift in neutron energy spectrum . . . . . 75

7.1.4 Small angle scattering . . . . . 75

7.1.5 Change of neutron path due to gravity or reflection . . . . . 76

7.1.6 Non-uniformities in the polarization product . . . . . 76

7.2 Systematic measurements with liquid $^4$He . . . . . 77

7.2.1 Large B field . . . . . 78

7.2.2 Large B field gradient . . . . . 80

7.2.3 Polarization product non-uniformity . . . . . 82

7.3 Simulation with magnetic fields . . . . . 82

7.3.1 Simulation for gradient systematic runs . . . . . 83

7.3.2 Simulation for a production data run with the greatest recorded field gradient . . . . . 85

7.3.3 Simulation for data taken with large uniform field . . . . . 86

7.4 Simulation with misalignments . . . . . 87

7.5 Summary of errors . . . . . 89

**8 Discussion** **91**

8.1 Final value and error budget . . . . . 91

8.2 Contribution of the measurement to understanding weak nucleon-nucleon (NN) physics . . . . . 92

8.2.1 Theoretical predictions for PNC neutron spin rotation in $^4$He . . . . . 92

8.2.2 Constraint from the measurement on weak meson-exchange coefficients 93

8.3 Improvements for future measurements . . . . . 95

8.3.1 Current experimental difficulties and possible remedies . . . . . 95

8.3.2 Next generation neutron spin rotation at NIST . . . . . 96

8.3.3 PNC neutron Spin rotation in liquid $^4$He at the Spallation Neutron Source (SNS) . . . . . 98
8.3.4 PNC neutron spin rotation in liquid hydrogen . . . . . 99
Bibliography . . . . . 100

# List of Figures

1.1 Weak interaction meson exchange diagram. The strong vertex is described by the well known strong coupling constants, $g_{\pi NN}$, $g_{\omega}$, $g_{\rho}$,. The weak couplings, $f_{\pi}$, $h_{\rho}$, $h_{\omega}$, are not well known. . . . . 3

1.2 Experimental constraints on DDH coupling coefficients. The bottom left plot shows the constraints from atomic parity violation. The bottom right shows the constraints from measurements in nucleons and nuclei ($P_{\gamma}$ for $^{18}F$, $A_{\gamma}$ for $^{19}F$ and $A_L$ for p-p system). The upper plot shows the 1996 spin rotation experiment in the n-$^4He$ system and proposed $P_{\gamma}$ measurement in the n-p system. . . . . 6

2.1 Experiment Layout . . . . . 13

2.2 Simplified representation of an experiment for measuring the spin rotation angle [5]. The target of length z is placed between a polarizer in the $\hat{x}$ direction and an analyzer in the $\hat{y}$ direction. The initial spin $\vec{\sigma}$ is a combination of 2 opposite helicity states that accumulate different phases due to the parity-non-conserving (PNC) weak interaction ($H_{PNC}$). The neutron spin also precesses in the residual magnetic field ($H_{mag}$) with a rate $\omega$ proportional to the B field. . . . . 14

2.3 Schematic diagram of the neutron spin through the polarimeter. The projection of the rotation angle onto the y-axis is shown at various positions along the apparatus. $\theta$ is the rotation due to magnetic background, L and R refer to the left and right sides of the experiment, F and B refer to the front and back target regions, and 0 and 1 refer to the target state. . . . . 16

2.4 Top schematic view and photographs of the supermirror polarizer. The cross sectional area shown in the photographs is 55 mm wide and 45 mm tall. . . . . 20

2.5 Input glass beam guide. The outer layer is Pyrex glass and the inner layer is Borofloat glass. . . . . 21

2.6 Diagram of the input coil [5] . . . . . 21

2.7 Diagram of the spin coil. . . . . 22

2.8 Downstream photo of the cryostat with the target insert with the end flanges and thermal shields removed. Both the 4K and 77K volumes are suspended by G10 straps, with the target insert resting within the 4K bore. Also shown on the face of the target insert are the electrical feedthroughs and the G10 tube for the pump drive shaft and the drain pipe control strings. An indium sealed aluminum window (0.8 mm thick, 38 mm radius) is at the center of the target insert face, in the neutron path. . . . . 23

2.9 The top figure shows a schematic side view of the liquid helium target with the $\pi$-coil installed [17]. The photo in the bottom shows the chamber on the left (upstream) with the lid open, and the Li collimators can be seen. . . . . 25

2.10 Diagram of the target collimation geometry. The width is at least 2 mm (at the septum); The separation is 1/4 of the target length, 104 mm; $\theta_c$, the critical angle, is 0.679 (0.798) mrad/$\mathring{A}$ between aluminum 6061 and helium interface at 4K for liquid (gas) He [16]. . . . . 26

2.11 $\pi$-coil (180° rotator coil) on the right. The ruler is 6" long and shown for scale. Half-toroid coils shown on the left. . . . . 26

2.12 Winding scheme of the $\pi$-coil [5]. On the outside edge, half the wires are wrapped down the coil and the other half progress up the coil. The arrows show the current direction. . . . . 27

2.13 Magnetic field map of the output coil. The increasing vertical field is generated by the rotator coil and the flipping coil generates the horizontal field. The sign of the horizontal field flips at a rate of 1 Hz (thus the name flipping coil), rotating the spin vector alternately $\pm\pi/2$ radians into the polarization analyzer in the vertical direction. . . . . 28

2.14 Cross section of the output guide. The shaded outer layer is Pyrex glass and the inner layer is Borofloat glass. . . . . 29

2.15 Side view of the ionization chamber with 4 detection segments. . . . . 30

2.16 Frontal view of the signal plates divided into 4 quadrants [17]. The inner circle marks the opening for the beam and the small shaded circles are supporting posts. 31

3.1 Longitudinal magnetic field measured inside the $\mu$-metal shields [17]. The innermost shield is right outside of the target insert. The end caps have been removed in the photo. . . . . 33

3.2 Compensation system . . . . . 34

3.3 Bartington Mag-01H fluxgate magnetometer with sensor placed on the top. . . . . 35

3.4 Difference amplifier circuit diagram . . . . . 35
3.5 Magnetic field measurement inside the target insert with the compensation system off (top plot) and on (bottom plot). . . . . 38

4.1 Initial wavelength distribution before NG-6 neutron beam enters our apparatus. . 40
4.2 Beam images taken downstream of the PSM (top left), input coil (top right) and output guide (bottom) [18]. All images are looking upstream into the beam so that the left side of the image represents the right side of the beam. . . . . 42
4.3 Measured polarization product PA as a function of neutron wavelength at the middle, west and east parts of the beam [18]. . . . . 44
4.4 Tagword illustrating the apparatus state control sequence. The top plot shows 1 complete target cycle with 2 target states, 3 $\pi$-coil states and 2 output coil flipping states. . . . . 47
4.5 Polarization product PA measured throughout all 3 beam cycles when production data runs were taken. Measurements for the east and west sides of the experiment and with the $\pi$-coil on and off are shown. . . . . 49

5.1 The top plot shows the TA for the East and West sides; the bottom plot shows the difference of the TA's and the TagWord as a function of time. The 2 target cycles after 7200 s were removed from the final data set. . . . . 53
5.2 Preliminary run-by-run PNCA results with $\pi$-coil on (P02) and off (P1). A total of 242 runs, 22.0 days of live data were taken in 118 calendar days of beam time. . 54
5.3 The spin angle from an individual run before (top plot) and after regression (bottom plot). . . . . 57
5.4 The PNC angle after regression with spin angle and polarization product application. 61

6.1 Top view of neutron transport through the apparatus . . . . . 64
6.2 Relative neutron flux (100% after the PSM) vs. input critical angle. Both the experiment and simulated flux are with He gas in the target. . . . . 65
6.3 Initial neutron counts vs. wave length . . . . . 65
6.4 Cross-sectional dimensions of beam along apparatus . . . . . 66
6.5 Neutron energy-dependent scattering cross section in liquid $^4$He. . . . . 68
6.6 $S(q,\omega)$ 3D plot. . . . . 69
6.7 Measured n-$^3$He absorption cross section as a function of neutron energy with a fit to the data. . . . . 70
6.8 Simulated spectra into the detector and after each of the 4 segments. . . . . 71

7.1 Measured spin rotation angles in the West (blue), East (red) and difference between West and East (black). Noise from beam intensity fluctuations is suppressed and width of W-E difference of rotation angles is $\sim \sqrt{N}$ statistics. . . . . 73
7.2 Trim coil positions relative to the liquid He targets. The 4 fluxgate sensors (M0, M1, M2 and M3) are located on top of the 2 targets. . . . . 78
7.3 Large B field in the target area produced by trim coils. . . . . 79
7.4 PNC angle measurements with large B fields in the target area. . . . . 79
7.5 Current for each trim coil to produce a large B field gradient. . . . . 80
7.6 Large B field gradient in the target area produced by trim coils. . . . . 81
7.7 PNC angle measurements with a large B field gradient. . . . . 81
7.8 PNC angle measurements with a large B field gradient. . . . . 82

7.9 Field profile for gradient systematic runs. The calculated field from trim coil currents is corrected by multiplying a factor of 1.24 to match the fluxgate readings. The large scale of the integrated field $Bdz$ is reduced so it can be shown on the same figure. The target positions upstream and downstream of the $\pi$-coil are also shown. . . . . 84

7.10 B field gradient for data run 1154. The fluxgate readings are fit with a 3rd order polynomial. . . . . 86

7.11 Field spatial profile for data runs with a large uniform field in the target region. . 87

7.12 Top view of misalignment 0.5 cm to the west from target downstream. . . . . 88

7.13 Top view of misalignment 0.01 rad to the east from target downstream. . . . . 89

8.1 Experimental constraints on weak meson-exchange coupling coefficients from measurements of PNC neutron spin rotation in liquid $^4$He. Both measurements are consistent with each other and the DDH reasonable range. . . . . 94

8.2 Use of the 120 days of beam time at NIST [32]. The time to collect the analyzed production data is about 22 days. . . . . 95

8.3 Count rate relative to the 2nd generation Neutron Spin Rotation (NSR II) measurement in 2008 with beam guide NG-6. NG-6 Max size uses the largest target that will fit with the NG-6 beam guide, 7 $\times$ 7 cm. A larger target (10 $\times$ 10 cm) will be needed to use the larger NG-C beam, as well as new input/output beam guides with larger m values to accommodate the larger NG-C m value of 3.6. . . . 97

# List of Tables

1.1 Meson exchange model in NN system . . . . . 4

4.1 Average neutron capture flux measured at various positions along the apparatus [18]. Capture flux is the integral of the flux over the velocity distribution weighted by a factor of $\frac{v_0}{v}$ to take into account the velocity dependence for neutron absorption, $v_0 = 2200$ m/s by convention. . . . . 41

5.1 Measured polarization product for each data run group. . . . . 59

6.1 Percentage of neutron beam absorbed in each detector segment. . . . . 71

7.1 Simulated spin angle and PNC angle compared to data for run 1154 . . . . . 85

7.2 Summary of experimental errors . . . . . 90

8.1 Weak meson-exchange coupling coefficients predicted by Desplanques, Donoghue and Holstein [8]. Strengths are in units of the sum rule value $g_{\pi NN} = 3.8 \times 10^{-8}$. 93

# Chapter 1

# Introduction and Theoretical Background

## 1.1 Introduction

In the quest to understand the four forces in nature (gravity, electromagnetism, weak and strong forces) physicists have always studied conservation laws and symmetries. Mathematically, there is a conserved quantity for each invariance of the Hamiltonian. For example, energy conservation arises from invariance under time reversal and momentum conservation from invariance under linear spatial translations. For invariance of the Hamiltonian under spatial inversion, the corresponding conserved quantity is parity.

In 3 dimensions, a parity transformation reflects the coordinates of a system through the origin, $P(\vec{r}) \rightarrow -\vec{r}$. Although previous experimental evidence in nuclear physics upheld the concept of parity conservation, Lee and Yang presented a theoretical argument in 1956 [1] that parity violation is possible under the weak interaction. Wu *et al.* measured a non-zero asymmetry of electrons emitted in the $\beta$-decay of polarized $^{60}$Co nuclei in 1957 [2]. This measurement was the first definitive evidence that the weak interaction violates parity, and it is the only known force to do that.

The weak interaction is well understood in leptonic systems with point particles such as electrons and neutrinos. Only the electromagnetic and weak interactions are involved for these systems. However, for systems with hadrons, composite particles constructed from quarks, weak interaction processes are very difficult to compute due to the complicating presence of the strong interaction. Because the strength of the weak interaction is about a factor of $10^7$ smaller than that of the strong nuclear force, we must exploit its symmetry-breaking properties to study the weak force between hadrons.

One example of a parity-violating (PV) observable in a hadronic system is the rotation of the transverse spin vector of very low energy ($\sim 10^{-3}$ eV) spin 1/2 hadrons, such as neutrons, that can be treated as waves as they travel through a spin-zero material. This extremely small, parity-violating rotation ($\sim 10^{-5}$ radians per meter of target) was first observed in heavy isotopes of tin (Sn) [3] and lanthanum (La) [4]. Nuclear structure calculations in heavy nuclei can be difficult and inhibit the ability to extract direct NN weak interaction information, so it is beneficial to examine light nuclear systems. However, the neutron spin rotation in light nuclear systems is smaller than in heavy nuclei, which is an experimental disadvantage. This Ph.D. dissertation research is the second generation measurement of the PV neutron spin rotation in liquid Helium ($^4_2He$). The first measurement was conducted in 1996 [5].

## 1.2 Theoretical Background

### 1.2.1 Parity-violating nucleon-nucleon (NN) weak interaction

The direct exchange of the short-ranged, weak vector bosons (W, Z) between low energy nucleons is suppressed by the repulsive strong interaction in the core. A representation of the NN weak interaction uses the meson exchange model which successfully describes

the low-energy strong interaction between nucleons. The parity-conserving strong NN interaction can for example be described phenomenologically by the sum of meson exchange diagrams in which the $\pi$, $\eta$, $\rho$, $\omega$, $\sigma$... mesons couple strongly to the NN vertices. Similarly, the weak NN interaction can be modeled as an exchange of light mesons ($\pi$,$\rho$,$\omega$) where the diagram has one weak interaction vertex and one strong vertex, as shown in Figure 1.1 [7].

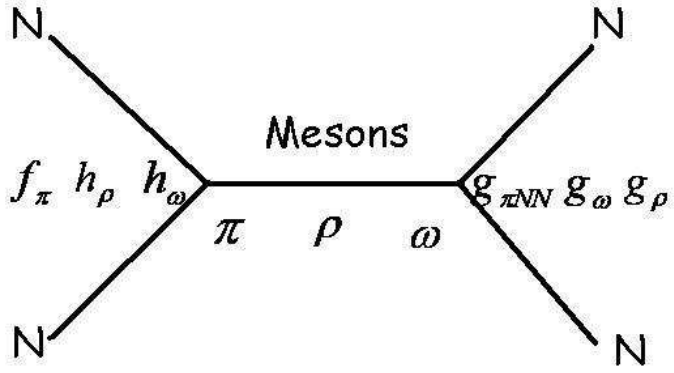


Figure 1.1: Weak interaction meson exchange diagram. The strong vertex is described by the well known strong coupling constants, $g_{\pi NN}$, $g_\omega$, $g_\rho$,. The weak couplings, $f_\pi$, $h_\rho$, $h_\omega$, are not well known.

The weak interaction physics is contained in the weak vertex, and is expressed in the values of the PV nucleon-nucleon-meson (NNM) coupling constants. The weak NNM matrix elements, $< MN|H_{wk}|N >$, for both the charged and neutral current contributions were estimated by Desplanques, Donoghue and Holstein (DDH) in 1980 [8]. Table 1.1 lists the 6 non-negligible meson exchange coefficients and their associated transition properties [9].

Recently, the NN weak interaction has been studied using effective field theory (EFT), which is ideally suited to situations with a distinct hierarchy of scales. In the present instance, the relevant scales are: the weak scale $v = (\sqrt{2}G_F)^{1/2} = 246\ GeV$ ($G_F$ is the Fermi constant); the hadronic scale $\Lambda_{HAD} \approx 1\ GeV$; the pion mass and decay constant, $m_\pi \approx 140\ MeV$ and $F_\pi = 93\ MeV$, respectively; and the typical momentum Q relevant for a PV hadronic or nuclear process. The distance at which the strong NN potential starts to

Table 1.1: Meson exchange model in NN system

| Isospin | NN system | | | Meson | Coupling |
|---|---|---|---|---|---|
| $\Delta$I | nn | np | pp | Exchanged | Coefficient |
| 0 | X | X | X | $\rho$, $\omega$ | $h^0_\rho$, $h^0_\omega$ |
| 1 | X | | X | $\rho$, $\omega$ | $h^1_\rho$, $h^1_\omega$ |
| 1 | | X | | $\pi^\pm$, $\rho$, $\omega$ | $f_\pi$, $h^1_\rho$, $h^1_\omega$ |
| 2 | X | X | X | $\rho$ | $h^2_\rho$ |

dominate, $r \leq 0.4\ fm$, corresponds to a mass scale of $\geq 500\ MeV$, which is comparable to the scale of $\Lambda_{HAD}$. The size of hadronic weak interaction matrix elements is governed by the ratio of $F_\pi^2$ to $v^2$, typically normalized to $g_{\pi NN}$.

The remaining scales can be used to construct an effective Lagrangian out of nucleon and pion fields, where the operators are organized according to the powers of $Q/\Lambda$. For processes with $Q \ll m_\pi$, the pion is treated as a heavy particle ($\Lambda = m_\pi$) and "integrated out" of the effective theory. For $Q \geq m_\pi$, the pion must be kept as an explicit degree of freedom and $\Lambda = \Lambda_{HAD}$. Thus the two different regimes of Q correspond to two versions of the EFT: the pionless and pionful EFT [34]. In 2005 Zhu *et al.* formulated the PV NN interaction in the EFT framework with and without pions [35]. The pionless version only contains the short-range interaction and is specified by five low-energy constants at the leading order.

In 2007 Liu used a hybrid EFT approach for low-energy weak NN processes, which combines the wave functions from phenomenological potential model calculations and the most general EFT operator structure [31]. Liu found that the PV NN interaction can be specified by a set of six parameters, including five S-P scattering amplitudes first pointed out by Danilov [36], and an additional parameter proportional to the PV pion-nucleon coupling coefficient $f_\pi$ that characterizes the long-range one-pion exchange.

### 1.2.2 Experimental studies of weak NN interaction

Since the weak interaction violates parity, NN weak interaction experiments involve the measurement of observables that are odd under spatial inversion. Observables proportional to $(\vec{\sigma} \cdot \vec{p})$ are parity violating, because momentum changes sign under parity but spin does not.

One PV observable is the circular polarization of gamma rays emitted by an unpolarized nuclear state with mixed parity: $P_\gamma = \langle \vec{\sigma}_\gamma \cdot \hat{p}_\gamma \rangle$. Unfortunately circular polarization experiments have restricted precision due to the low efficiency of circular polarization analyzers for few MeV photons (about 4%). The angular distribution of photons emitted along the polarization direction of a nucleus is also parity-violating. It is related to the nuclear polarization $\vec{J}$ by $A_\gamma = \langle \vec{J} \cdot \hat{p}_\gamma \rangle$. Another common PV observable is the longitudinal analyzing power $A_L$ of reactions initiated by nucleons that are spin-polarized parallel or anti-parallel to their momentum. The analyzing power is proportional to the asymmetry of cross sections for incident nucleons in forward and backward helicity states. The next sub-section discusses the observable measured for this dissertation: the PV neutron spin rotation $\phi_{PV}(\vec{n},^4 He)$.

Figure 1.2 shows the experimental constraints on the weak coupling coefficients. It is helpful to use a simplified two-dimensional subspace in isospin space to present the results. The linear combination $h^0_\rho + 0.6 h^0_\omega$ is an isoscalar contribution in most nuclei and the isovector contribution is dominated by $f_\pi$. The DDH reasonable range is calculated with the best values for the other coupling constants [8]. A measurement of $\phi_{PV}(\vec{n}, \alpha)$ in 1996 has the result [5]:

$$\phi_{PV}(\vec{n}, \alpha) = [8.0 \pm 14(stat) \pm 2.2(syst)] \times 10^{-7}\ rad/m \tag{1.1}$$

In Chapter 8 the result of the new measurement for this dissertation will be presented along with the error budget that significantly cuts into the DDH reasonable range.

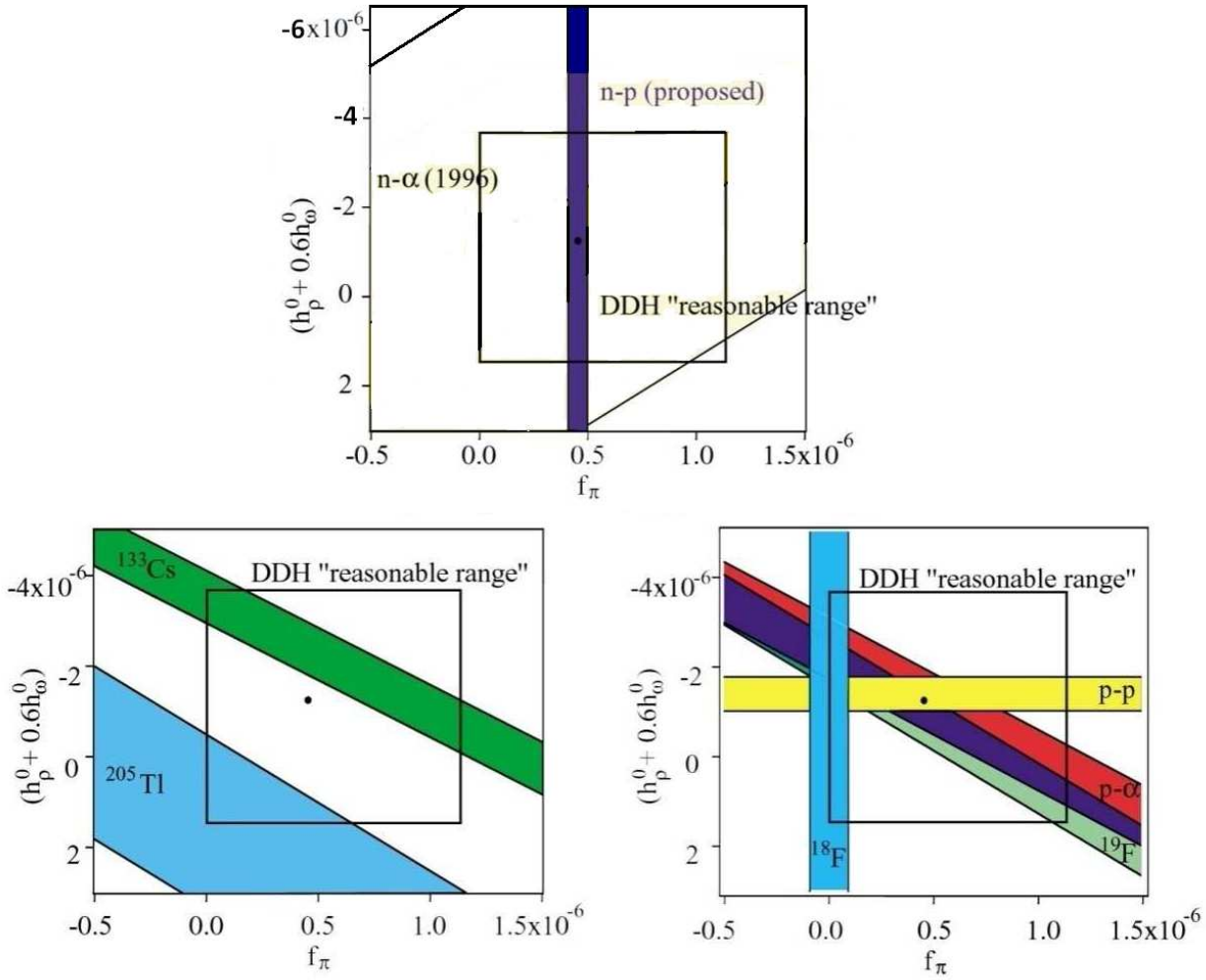


Figure 1.2: Experimental constraints on DDH coupling coefficients. The bottom left plot shows the constraints from atomic parity violation. The bottom right shows the constraints from measurements in nucleons and nuclei ($P_\gamma$ for $^{18}F$, $A_\gamma$ for $^{19}F$ and $A_L$ for p-p system). The upper plot shows the 1996 spin rotation experiment in the n-$^4He$ system and proposed $P_\gamma$ measurement in the n-p system.

### 1.2.3 Neutron spin rotation theory

In 1964, Michel first proposed that the weak interaction could produce an observable effect with neutrons that is analogous to the optical rotation of polarized photons propagating through a "handed" medium [10]. Cold neutrons traveling through a spin-zero nuclear target experience a PV rotation of the spin vector. The Coulomb, magnetic, and spin-dependent nuclear interaction are absent under these conditions.

For $E \leq 0.025\ eV$, the de Broglie wavelength of neutrons ($\lambda = h/p$) is on the order of, or greater than, the interatomic spacing in materials. At these wavelengths ($\lambda > 1\mathring{A}$), the wave properties of neutrons dominate over their particle properties and neutron optics theory can be applied. For a single scattering center, the neutron wave function outside of the potential well can be written as the sum of the incident plane wave and the scattered wave:

$$\psi_n = e^{i\vec{k}\cdot\vec{r}} + f(\theta)\frac{e^{ikr}}{r} \tag{1.2}$$

where $f(\theta)$ is the scattering amplitude, and $\vec{k}$ is the neutron wave vector given by

$$\mid \vec{k} \mid = (2\pi)/\lambda = \mid \vec{p} \mid /\hbar \tag{1.3}$$

With the neutron wavelength $\lambda > 1\mathring{A}$, it is greater than the relatively short range of the strong nuclear force, and the scattering is predominantly s-wave and isotropic. As a result, the scattered wave amplitude is independent of angle [11]. This leads to

$$f(\theta) = f(0) = -a \tag{1.4}$$

where $a$ is the scattering length.

By analogy with geometric optics for light, an incident neutron plane wave is refracted in a medium. The effective index of refraction can be derived from the coherent forward scattering amplitude, $f(0)$. For a collection of nuclei, the quantum mechanical wave equation satisfied by a neutron can be written as

$$[\nabla^2 + k^2] < \psi_n >= 0. \tag{1.5}$$

where $< \psi_n >$ is the energy-averaged wave function for the neutron. Outside the medium the wave number is given by

$$k^2 = {k_o}^2 = \frac{2mE}{\hbar^2} \tag{1.6}$$

and inside the medium it is

$$k^2 = {k_i}^2 = \frac{2m}{\hbar^2}(E - (V + iW)) \tag{1.7}$$

where $V$ and $W$ are the real and imaginary parts of the effective scattering potential for the medium. For slow neutrons, $E < 1eV$, the scattering potential is independent of the wavelength of the incident neutron. We can derive the effective index of refraction by the ratio of wave numbers

$$n^2 = \frac{{k_i}^2}{{k_o}^2} = (1 - \frac{V + iW}{E}) \tag{1.8}$$

similar to the ratio of velocities inside and outside the medium in geometric optics. The wave equation inside the medium is expressed as

$$[\nabla^2 + {k_o}^2 n^2] < \psi_n >= 0. \tag{1.9}$$

The familiar plane wave form of the wave function satisfies this wave equation

$$< \psi_n > \sim e^{i\vec{k}\cdot\vec{r}} \sim e^{in\vec{k_o}\cdot\vec{z}} \sim e^{-Im(n)\vec{k_o}\cdot\vec{z}} e^{iRe(n)\vec{k_o}\cdot\vec{z}}. \tag{1.10}$$

If the imaginary part of the potential is nonzero ($W \neq 0$), the wave is attenuated as it passes through the medium. The real part of the potential contributes a phase to the neutron wave as it travels through the medium, given by

$$\varphi = Re(n)k_o z \tag{1.11}$$

for $\vec{k_o} = k_o\hat{z}$ where $\hat{z}$ is defined as the incident neutron (beam) direction.

The phase shift of the wave function can be related to the depth of the scattering potential well quantum mechanically for an individual nucleus. The average of this potential over the nuclei in the medium gives the average scattering potential as [12] [13]

$$V \approx \bar{V} = (\frac{2\pi\rho\hbar^2}{m})a \tag{1.12}$$

where $\rho$ is the material number density and $a$ is the scattering length defined in Equation 1.4. This expression can be obtained by integrating the effective Fermi potential (a non-physical step potential) over an isotropic distribution of scatterers [14].

If we only consider non-absorptive media where $W = 0$, we can substitute Equation 1.12 into Equation 1.8 and use the low-energy relation between the neutron energy and momentum ($E = p^2/2m$) to get the following relationship between the index of refraction and the scattering length:

$$n^2 = (1 - \frac{4\pi\rho\hbar^2 a}{p^2}) \tag{1.13}$$

Taking the square root of Equation 1.13, and using Equation 1.4 with $p = \hbar k$, the index of refraction can be expressed in terms of the forward scattering amplitude

$$n = 1 - \frac{2\pi\rho\hbar^2 a}{p^2} = 1 + (\frac{2\pi}{k^2})\rho f(0). \tag{1.14}$$

For low-energy neutrons, the most general form of the coherent forward scattering amplitude is given by

$$f(0) = A + B\vec{\sigma}_n \cdot \vec{S}_N + C\vec{\sigma}_n \cdot \vec{k}_n + D\vec{S}_N \cdot \vec{k}_n + E\vec{\sigma}_n \cdot (\vec{k}_n \times \vec{S}_N) \tag{1.15}$$

where $\vec{\sigma}_n$ and $\vec{k}_n$ are the neutron spin and wave vector respectively, $\vec{S}_N$ is the spin of the target nucleus, and higher order terms in the neutron momentum have been neglected. For unpolarized nuclear spin systems ($< \vec{S}_N >= 0$), the amplitude is reduced to two terms.

The parity-conserving term, $A$, contains contributions from the strong and electromagnetic interactions. The second term, proportional to $\vec{\sigma}_n \cdot \vec{k}_n$, is odd under parity transformations and thus contains only contributions from the weak interaction. We express Equation 1.15 in parity-conserving (PC) and parity-violating (PV) terms as

$$f(0) = f_{PC} + f_{PV}(\vec{\sigma}_n \cdot \vec{k}_n) \tag{1.16}$$

There is a different scattering amplitude, $f_\pm$, for the opposite helicity states $\vec{\sigma}_n \cdot \vec{k}_n = \pm k$. As a result, the two helicity states have different indices of refraction, $n_+$ and $n_-$, and they accumulate different phases as the neutron wave propagates in a medium. We combine Equations 1.11, 1.14, 1.16 to obtain an expression for the two phases and identify the PC and PV terms

$$\varphi_\pm = \varphi_{PC} \pm \varphi_{PV} \tag{1.17}$$

where

$$\varphi_{PC} = kz(1 + \frac{2\pi\rho}{k^2} f_{PC}) \tag{1.18}$$

and

$$\varphi_{PV} = 2\pi\rho z f_{PV} \tag{1.19}$$

In these approximations, the PV contribution to the phase is independent of neutron energy and directly proportional to the weak interaction matrix elements through the PV part of the forward scattering amplitude.

Transverse polarization is a linear combination of equal contributions from the two helicity states. For the spin "up" state

$$|\uparrow> = \frac{1}{\sqrt{2}}(|+> + |->) \rightarrow \frac{1}{\sqrt{2}}(e^{i\varphi_+}|+> + e^{i\varphi_-}|->) \tag{1.20}$$

With Equation 1.17 we can see that the PC phase contributes an overall phase factor and the PV phase produces a rotation about the propagation axis. The PV rotation angle of the transverse spin, $\varphi_{PV}$, is therefore the accumulated difference in phase between the two helicity states

$$\phi_{PV} = \varphi_+ - \varphi_- = 2\varphi_{PV} = 4\pi\rho z f_{PV} \tag{1.21}$$

We can write $f_{PV}$ in terms of the weak matrix elements:

$$f_{PV} = -\frac{M}{2\pi} Re < He, \psi_i \mid H_{wk} \mid \psi_o, He > \tag{1.22}$$

where $M$ is the neutron mass and $\psi_i$ and $\psi_o$ are incoming and outgoing neutron wave functions. The weak matrix elements can be calculated and expressed in terms of the weak coupling constants $h_\rho^0$, $h_\omega^0$, $f_\pi$, $h_\rho^1$, $h_\omega^1$, and $h_\rho^2$. Dmitriev and collaborators obtained an expression for the neutron spin rotation in liquid $^4$He in terms of the coupling constants [28]: $-(0.97 f_\pi + 0.22 h_\omega^0 - 0.22 h_\omega^1 + 0.32 h_\rho^0 - 0.11 h_\rho^1)$ rad/m. Measuring the PV rotation angle thus puts constraints on those constants. The next chapter will describe the apparatus for the measurement.

# Chapter 2

# Experimental Overview

## 2.1 Apparatus overview

In this chapter each component of the apparatus for our experiment at the National Institute of Standards and Technology (NIST) will be reviewed. Those components are shown in Figure 2.1. The neutrons become transversely polarized as they pass through the polarizing supermirror (PSM), and they travel to the low magnetic field target region through a glass guide tube in the input coil, which preserves the spin polarization in the vertical direction. The PV interaction then rotates the neutron spin as the neutrons traverse the liquid $^4$He target. The neutrons leave the target region and pass through the glass guide of the output coil which preserves the horizontal component of the spin, and then enter the analyzing supermirror (ASM). A detector behind the analyzer measures the count rate which is proportional to the spin rotation angle. The entire target region is shielded by $\mu$-metal shields from Earth's ambient magnetic field and compensation coils are used for active shielding.

The neutron spin rotation is measured with the transmitted neutrons passing through an analyzer whose polarization direction is rotated 90° with respect to the initial polarization axis, similar to optical polarization experiments. Our polarizer has a 90° offset to be linearly sensitive to the neutron spin-rotation angle. A schematic representation is given in

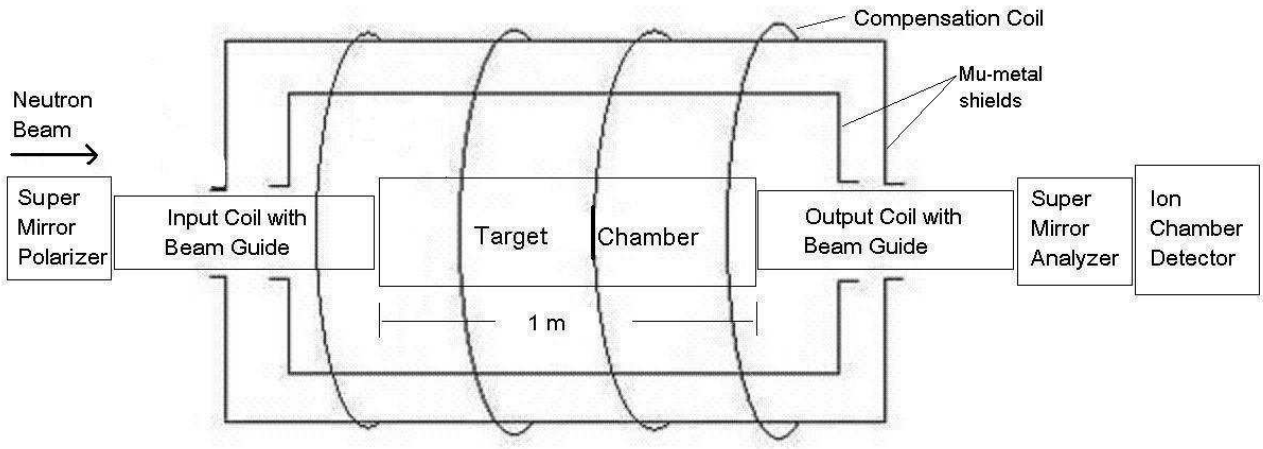


Figure 2.1: Experiment Layout

Figure 2.2.

From Equation 1.20, we can describe a neutron initially transversely polarized in the spin-up state, along $\hat{x}$, by a linear combination of helicity states along the beam direction, $\hat{z}$.

$$| +\hat{x} >= \frac{1}{\sqrt{2}}(| + > + | - >) \tag{2.1}$$

The new state of the rotated polarization vector at a distance z about the momentum axis $\hat{z}$ is given by

$$| \varphi >= \frac{1}{\sqrt{2}}(e^{\frac{i\varphi}{2}} | + > + e^{-\frac{i\varphi}{2}} | - >) \tag{2.2}$$

from Equation 1.20, where $\varphi$ is the rotated angle.

The expression for the "up" state in the analyzer direction $+\hat{y}$, which is transverse to both the momentum and the initial polarization, is given by a 90° rotation of the $\hat{x}$ state about the z axis

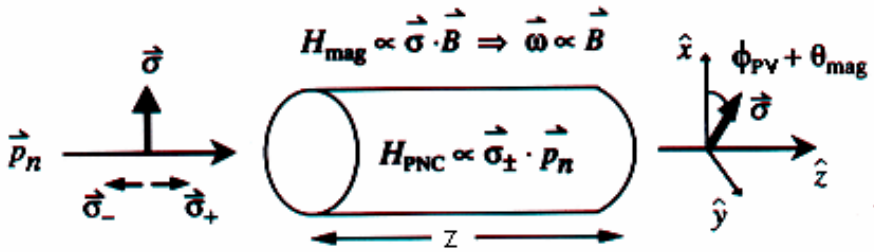


Figure 2.2: Simplified representation of an experiment for measuring the spin rotation angle [5]. The target of length z is placed between a polarizer in the $\hat{x}$ direction and an analyzer in the $\hat{y}$ direction. The initial spin $\vec{\sigma}$ is a combination of 2 opposite helicity states that accumulate different phases due to the parity-non-conserving (PNC) weak interaction ($H_{PNC}$). The neutron spin also precesses in the residual magnetic field ($H_{mag}$) with a rate $\omega$ proportional to the B field.

$$| +\hat{y} >= \frac{1}{2}[(1-i) \mid + > +(1+i) \mid - >] \tag{2.3}$$

The neutron count rate in the $+\hat{y}$ state is thus given by

$$N_+ = |< +\hat{y} \mid \varphi >|^2 = \frac{1}{2}(1 + \sin\varphi) \tag{2.4}$$

Similarly the count rate for the $-\hat{y}$ state is

$$N_- = \frac{1}{2}(1 - \sin\varphi) \tag{2.5}$$

So the rotation angle of the spin about the momentum axis is

$$\sin\varphi = \frac{N_+ - N_-}{N_+ + N_-} \tag{2.6}$$

To measure the neutron spin rotation, the experiment involves counting neutrons from a crossed polarizer ($\hat{x}$) and analyzer ($\hat{y}$) system, in which the final analyzer direction alternates between $+\hat{y}$ and $-\hat{y}$.

Heckel *et al.* [15] developed a polarimeter for measuring the spin rotation for transversely polarized neutrons through solid targets. That polarimeter had a target region located between a crossed polarizer and analyzer pair. The target region was divided into upstream and downstream positions by a "$\pi$-coil", a coil with a magnetic field aligned along $\hat{x}$ and field strength set for the neutron spin to precess about $\hat{x}$ by 180° as it passed through the coil. When the target alternated between upstream and downstream positions relative to the $\pi$-coil, the PV signal alternated in sign while any constant residual magnetic field produced a steady background rotation. Subtracting the measurements from the two target positions eliminated the background rotation, leaving twice the value of the PV rotation. This assumed that the rotation due to background fields was independent of the target.

The measurements on which this dissertation is based used the techniques developed by Markoff *et al.* [5] to measure $\phi_{PV}$ in liquid $^4$He. Markoff *et al.* modified the polarimeter to measure the PV signal from both the front and back target positions simultaneously. The apparatus, shown schematically in Figure 2.3, is divided into two side-by-side sections and each half effectively is a separate experiment under the same conditions. The targets are alternately filled in a diagonal pattern so that the PV rotation has opposite signs on the two sides of the apparatus due to the $\pi$-coil. While the front target chamber contains liquid on one side, the other beam side has the back target chamber filled, where front (upstream) and back (downstream) is defined with respect to the $\pi$-coil. The target state then alternates with the flipped state in which the previously empty diagonally positioned target chambers are filled. The beam line, the target chambers, the $\pi$-coil, and the detector are all divided into two side-by-side regions to prevent neutrons from crossing over from one side to the other.

The two diagonally positioned target states are labeled with subscripts 0 and 1, where the 0 state has the downstream left and upstream right positions filled with liquid $^4$He and state 1 the other configuration. If the rotations due to background fields, $\theta$, are independent of target state, we have

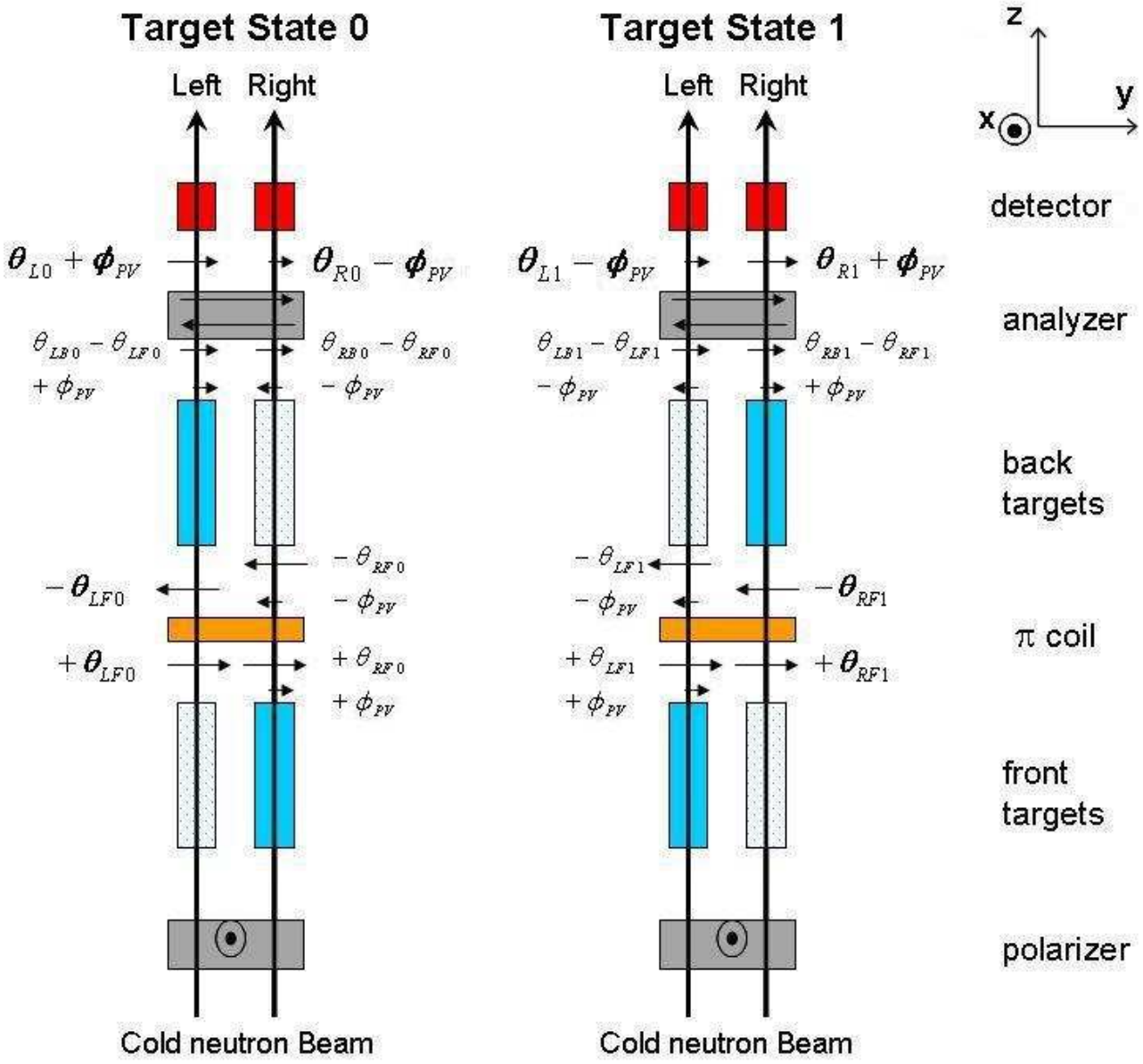


Figure 2.3: Schematic diagram of the neutron spin through the polarimeter. The projection of the rotation angle onto the y-axis is shown at various positions along the apparatus. $\theta$ is the rotation due to magnetic background, L and R refer to the left and right sides of the experiment, F and B refer to the front and back target regions, and 0 and 1 refer to the target state.

$$\theta_{L0} = \theta_{LB0} - \theta_{LF0} = \theta_{LB1} - \theta_{LF1} = \theta_{L1} \tag{2.7}$$

for the left side. L and R refer to the left and right sides of the experiment, F and B refer to the front and back target regions, and 0 and 1 refer to the target state. The total rotation due to both parity-violation and background fields for the left side is $\theta_{L0} + \phi_{PV}$ for target state 0 and $\theta_{L1} - \phi_{PV}$ for target state 1. Thus subtracting the measured rotation of target state 1 from state 0 gives twice the PV rotation:

$$(\theta_{L0} + \phi_{PV}) - (\theta_{L1} - \phi_{PV}) = 2\phi_{PV} \tag{2.8}$$

Doing the same analysis for the right side yields $-2\phi_{PV}$. Splitting the beam and measuring both the left and the right side simultaneously leads to noise cancelation from factors such as beam intensity fluctuation, and dividing the target into upstream and downstream halves of the $\pi$-coil cancels background rotations from ambient fields.

## 2.2 NCNR cold neutron beam and beam guide

At the NIST Center for Neutron Research (NCNR), neutrons are generated by a 20-MW research reactor. Fission neutrons from the reactor are slowed down to cold neutrons in two steps. First they are moderated to thermal energies (0.025eV, corresponding temperature 300K, wavelength 1.7$\mathring{A}$) by a $D_2O$ primary reactor coolant, then the neutrons pass through a cold source which is 5 liters of liquid hydrogen in an ellipsoidal shape maintained at a temperature of 20K to moderate the neutrons to cold energies (6meV, 75K, 7$\mathring{A}$)[6]. After leaving the cold source, neutrons enter evacuated rectangular guides (15 cm tall and 6 cm wide) coated with $^{58}$Ni, which transport the neutrons approximately 68 m from the cold source to Neutron Guide 6 (NG-6). $^{58}$Ni, with an effective neutron potential of 335 neV and a critical angle of 2.1 mrad/$\mathring{A}$, efficiently transports the cold neutrons through long distances with minimal losses. At the end of NG-6, the beam is split into upper and lower halves for

independent use. We use the upper part, and the lower part is devoted to other experiments.

The upper part of the neutron beam passes through a thin Mg window past the remote controlled beam shutter. Then the beam enters the experimental area where the equipment is assembled and aligned. After the shutter, the beam goes through a filter Dewar maintained at 77K with liquid nitrogen (LN). In the filter Dewar there are 2 blocks of Bi, each 5 cm thick, and one block of Be, 10 cm thick, which act as filters. Be is noncrystalline and scatters neutrons with wavelengths smaller than its interpolar spacing. This removes neutrons with wavelengths smaller than $\lambda = 3.96\mathring{A}$. Bi is a single crystal to stop gamma rays. The filters are placed in a sandwich orientation, Bi - Be - Bi, to keep the filters mechanically stable (Bi is much heavier and stronger than Be). Transmission through the filters is temperature dependent; lower temperature leads to less phonon scattering so both filters are kept at LN temperature (77K). Upon exiting the filter, the neutrons pass through a 50 mm tall by 60 mm wide $^6$LiF glass collimator that defines the beam cross-sectional area before entering the Supermirror Polarizer (SMP).

## 2.3 Supermirror polarizer and analyzer

The neutrons are polarized through spin-dependent scattering from magnetized mirrors. The magnetic contribution to the index of refraction is proportional to the local magnetization of the material [19] so that when neutrons are incident on a magnetized material equation 1.14 becomes

$$n = 1 - [\frac{2\pi\rho\hbar^2 a}{p^2} \pm \frac{\mu(B-H)m}{p^2}] \equiv 1 - \frac{\theta_{c\pm}^2}{2} \tag{2.9}$$

where $p$, $\mu$, and $m$ are the momentum, magnetic moment and mass of the neutron, $\rho$, $a$, and $B$ are the nuclear density, average bound coherent scattering amplitude and magnetic induction of the magnetic material, and $H$ is the applied field in the plane of the reflecting surface. The positive (negative) sign refers to the neutron magnetic moment, $\mu$, being parallel (antiparallel) to the magnetization, $(\vec{B} - \vec{H})$, of the reflecting medium. The critical

glancing angle, $\theta^2_{c\pm}$, is defined in Equation 2.9 as the maximum incident angle at which neutrons of the given spin state, ($\pm$), will reflect from the surface. The convention used here defines the incident and reflected angles, $\theta$, with respect to the reflecting surface.

The neutron supermirror is based on a multilayered design in which plates consisting of thin-film polarizing material laid on an absorptive substrate are stacked and bent into a curve with a large radius. A schematic diagram of the supermirror and photographs are given in Figure 2.4. The materials and thicknesses are chosen so that one spin state is preferentially reflected by the mirror surface ($\theta_c$ is large) and the other is transmitted ($\theta_c$ nearly zero) and absorbed in the underlying layers. The radius of curvature and plate spacing are chosen so that the neutrons must undergo at least one interaction with the ferromagnetic substance comprising the mirror surface. Typical polarization for these supermirrors is 98% and typical transmission through the supermirrors is about 30%. There are two supermirrors at NIST, and they are used as the polarizer and analyzer of our experiment.

## 2.4 Input coil

The input coil maintains the vertical spin polarization of the neutrons with a 5G vertical magnetic field as the neutrons exit the supermirror polarizer, and traverse the glass beam guide (shown in Figure 2.5) before entering the target region. The glass beam guide fits inside the input coil, and its outer layer is Pyrex glass and inner layer is Borofloat glass. Shown schematically in Figure 2.6, the input coil consists of windings on a 32-in long main core and two return cores on each side of the main core. The cores are made of non-magnetic G-10 circuit board material. The opening at one end of the main core allows the beam guide to pass through.

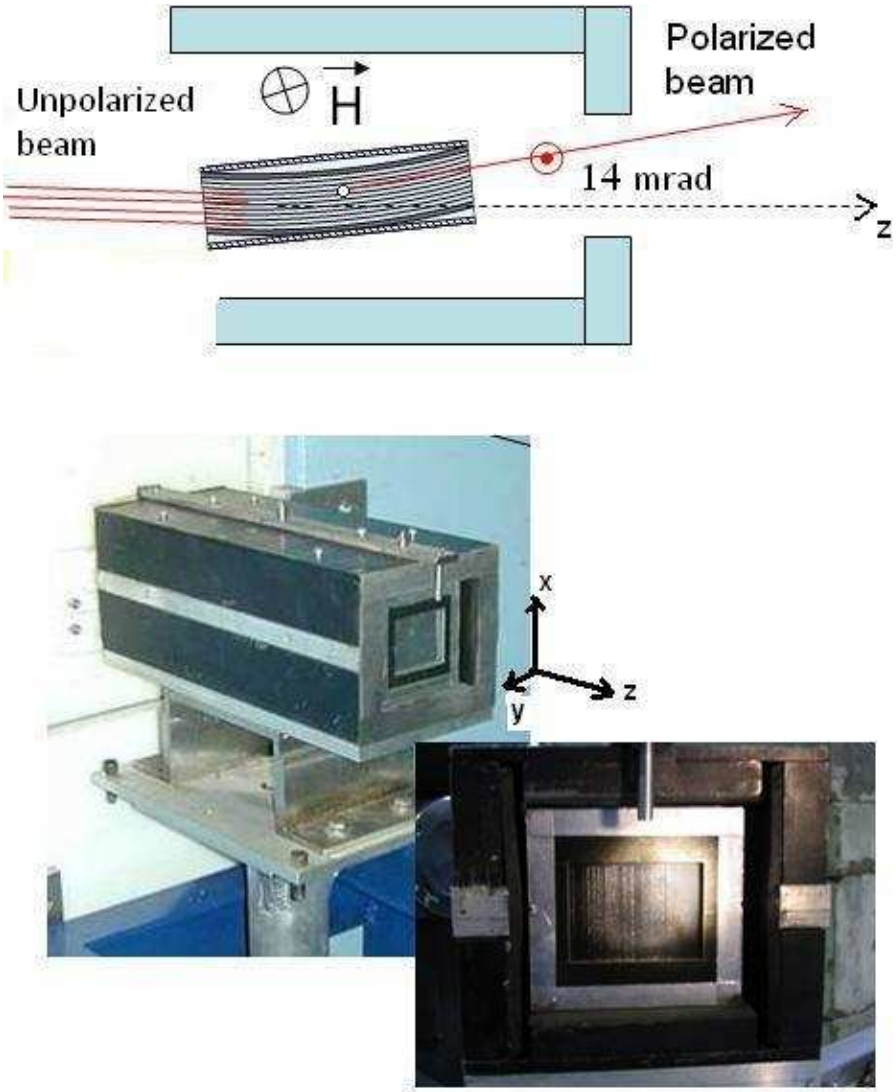


Figure 2.4: Top schematic view and photographs of the supermirror polarizer. The cross sectional area shown in the photographs is 55 mm wide and 45 mm tall.

Figure 2.5: Input glass beam guide. The outer layer is Pyrex glass and the inner layer is Borofloat glass.

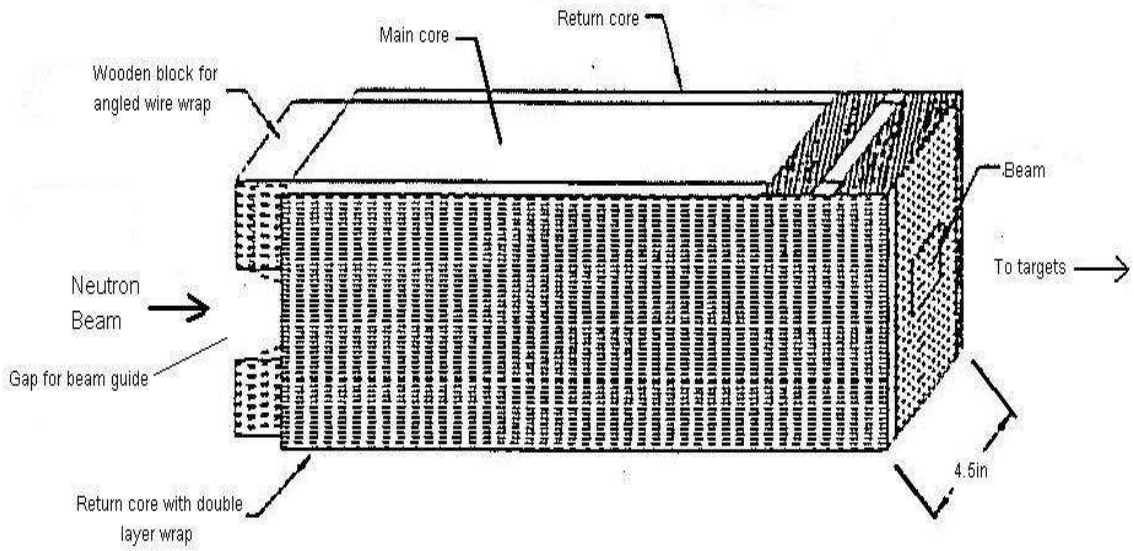


Figure 2.6: Diagram of the input coil [5]

## 2.5 Spin coil

When the neutrons exit the input coil, we found that the spin polarization had a slight forward tilt. This may have been caused by transverse non-uniformities in the input coil leakage field. This tilt would lead to a spin vector component that would be rotated 180° by the $\pi$-coil and add to the spin rotation inside the target area from the residue field and PV weak interaction.

To reduce this observed forward tilt of the neutron polarization, a "spin coil" was placed between the input coil and the target. The spin coil is a clean-up device with two side-by-side solenoid coils, shown in Figure 2.7. Each solenoid serves as a return coil for the other coil with equal and antiparallel vertical magnetic fields. Large fields (15G) are used to precess the non-vertical spin components of neutrons with different wavelengths many turns so the forward tilt is evened out. Therefore the average spin alignment of the whole spectrum is reset to vertical, although with a slightly lower polarization value.

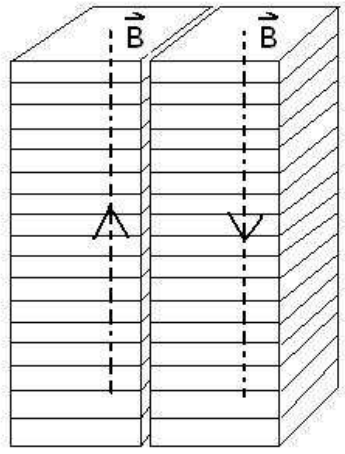


Figure 2.7: Diagram of the spin coil.

## 2.6 Cryostat and liquid helium target

The liquid He target is housed in a horizontal bore, nonmagnetic cryostat built by Oxford Instruments, Inc. This cryostat has two coaxial annular aluminum vessels in a cylindrical main vacuum as shown in Figure 2.8 with the target insert. The outer 77K volume can hold 50L of liquid nitrogen, and the inner 4K volume can hold 30 L of liquid helium [16].

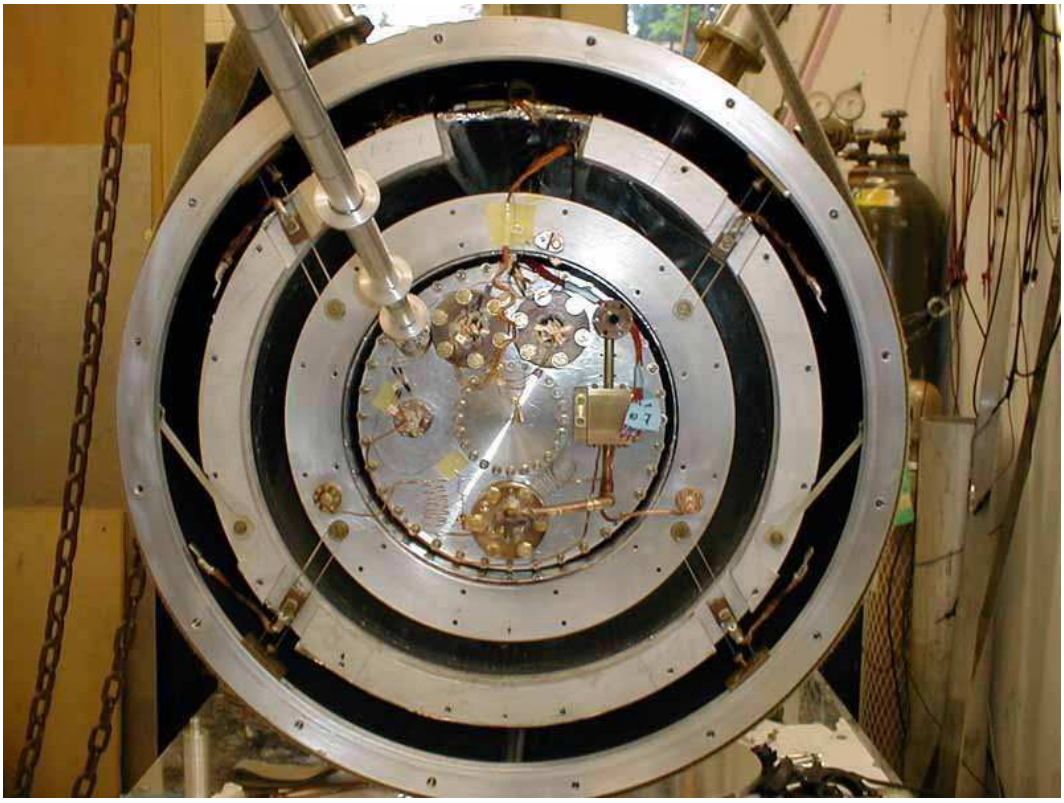

Figure 2.8: Downstream photo of the cryostat with the target insert with the end flanges and thermal shields removed. Both the 4K and 77K volumes are suspended by G10 straps, with the target insert resting within the 4K bore. Also shown on the face of the target insert are the electrical feedthroughs and the G10 tube for the pump drive shaft and the drain pipe control strings. An indium sealed aluminum window (0.8 mm thick, 38 mm radius) is at the center of the target insert face, in the neutron path.

Resting in the target insert is the liquid He target, shown in Figure 2.9. The target is built from completely non-magnetic materials, and all components produce field changes

less than $10\mu G$ when moved past a fluxgate magnetometer sensor at 1 cm distance. The target has identical upstream and downstream chambers 416 mm long, 70 mm wide and 60 mm tall. Each chamber is separated into left and right halves by a 3 mm wall in the middle. The target body is milled with a wire electrical discharge machine (EDM) from a solid 6061 aluminum billet with sufficient precision that the length difference of the 4 chambers is less than 0.01 mm over the $\sim$1 m target length [16].

The centrifugal pump and plumbing to pump liquid He into the chambers are also shown in Figure 2.9. The target insert is sealed and serves as a liquid He reservoir. The drain pipes can be pulled up and down by strings controlled by the DAQ program, so that the left-upstream/right-downstream chambers can be filled for target state 0 and the right-upstream/left-downstream chambers for target state 1, shown in Figure 2.3. Liquid level sensors and fluxgate sensors are located on the target for liquid He level and magnetic field measurements.

Inside of each target chamber, 3 Li collimators positioned at 1/4, 1/2 and 3/4 length prevented neutrons from reflecting off the chamber walls and reaching the detector. Each collimator is 5 mm wide along the top, bottom and outer chamber walls and 2 mm wide along the septum, defining a beam 26.5 mm side and 50 mm tall for the left and right targets [16]. Shown in Figure 2.10, the geometry and spacing of the collimators are designed to prevent 20 $\mathring{A}$ or shorter wavelength neutrons from reflecting off the chamber walls and coming back into the target.

## 2.7 $\pi$-coil

As shown in Figure 2.11, the $\pi$-coil consists of two side-by-side rectangular coils, 16 cm high, 4 cm wide and 6 cm deep. The two solenoid coils (each associated with one side of the experiment) carry equal currents in opposite directions, producing equal and opposite vertical magnetic fields in the two halves of the beam. The neutron spin vector precesses

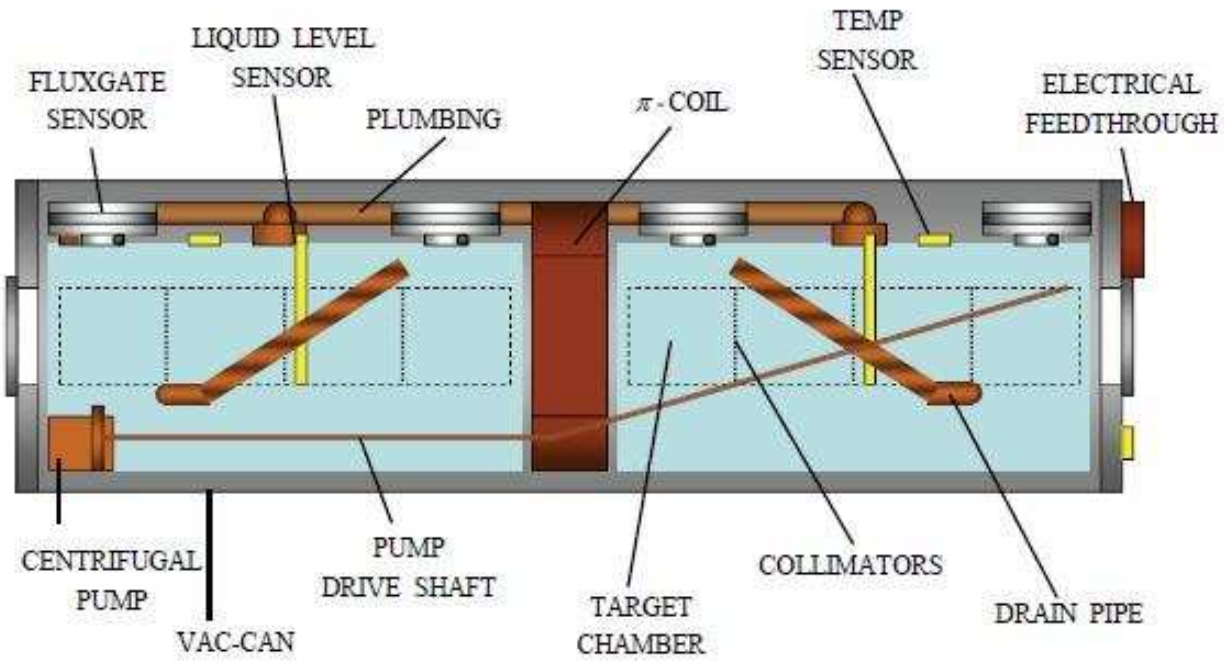


Figure 2.9: The top figure shows a schematic side view of the liquid helium target with the $\pi$-coil installed [17]. The photo in the bottom shows the chamber on the left (upstream) with the lid open, and the Li collimators can be seen.

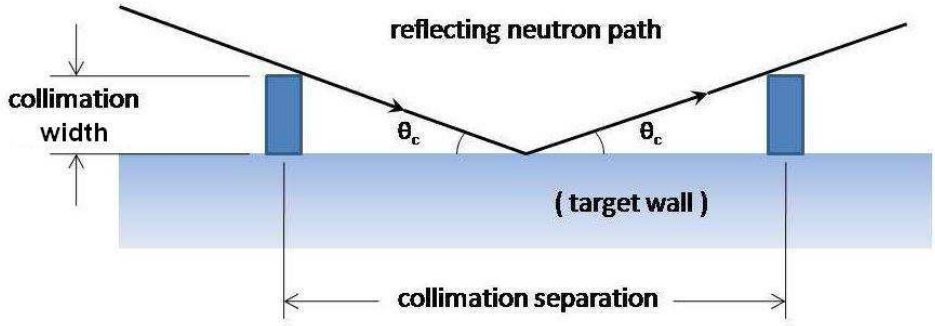


$$\text{separation} = 2\frac{(\text{ width })}{\tan(\theta_c \cdot \lambda)}$$

Figure 2.10: Diagram of the target collimation geometry. The width is at least 2 mm (at the septum); The separation is 1/4 of the target length, 104 mm; $\theta_c$, the critical angle, is 0.679 (0.798) mrad/$\mathring{A}$ between aluminum 6061 and helium interface at 4K for liquid (gas) He [16].

around the fields by 180°, hence the name $\pi$-coil. Figure 2.12 shows the winding scheme, with the wire wrap for two solenoid cylinders and the resulting overlap pattern on the side to suppress leakage fields. Each solenoid serves as a return coil for the magnetic flux of the other coil. Half-toroid coils located above and below the cylinders assist the return flux of the solenoid fields.

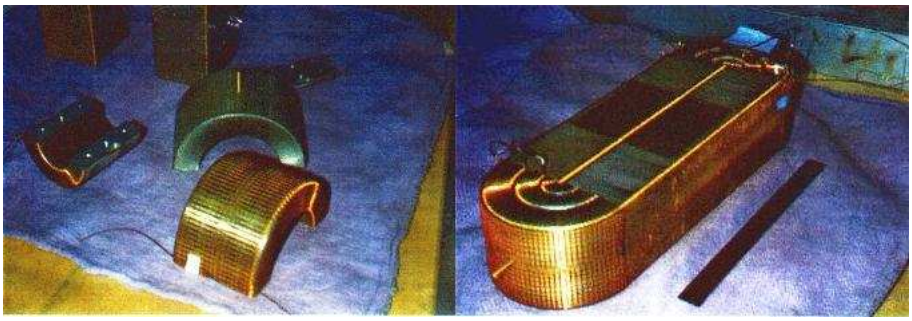

Figure 2.11: $\pi$-coil (180° rotator coil) on the right. The ruler is 6" long and shown for scale. Half-toroid coils shown on the left.

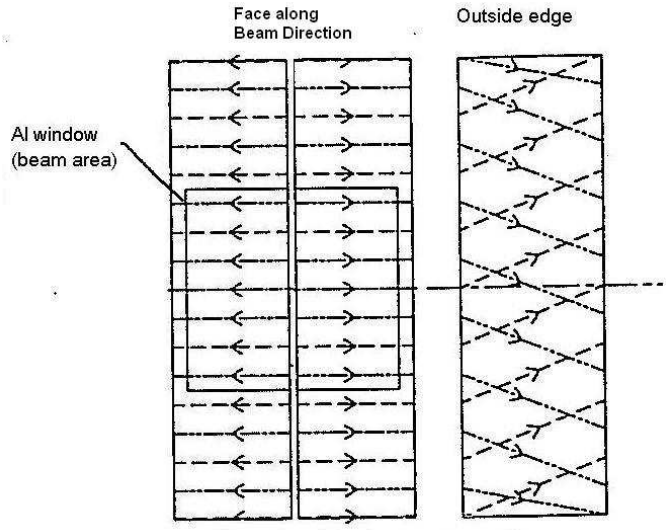


Figure 2.12: Winding scheme of the $\pi$-coil [5]. On the outside edge, half the wires are wrapped down the coil and the other half progress up the coil. The arrows show the current direction.

## 2.8 Output coil

The output coil is positioned between the downstream end of the field free target region and the suppermirror analyzer. It has two components: the rotator coil with an increasing field in the vertical ($\hat{x}$) direction, and the flipping coil similar in form and construction to the input coil, with a main core of length 38 inches and its field axis in the horizontal ($\hat{y}$) direction. Figure 2.13 shows the field map of the output coil. The rotator coil is epoxied onto the flipping coil so that the two fields are perpendicular, independent of the output coil rotation position.

The neutrons pass from the field-free region into the homogeneous magnetic field of the flipping coil in the $\hat{y}$ direction. This preserves the transverse component of the neutron spin, which carries the information of the spin-rotation angle in the transition from the target region. The rotator coil gradually rotates the magnetic field from the $\hat{y}$ direction of the flipping coil to the $\hat{x}$ direction of the supermirror analyzer. As the flipping coil field falls off, the field of the rotator coil in the vertical direction increases so that the neutron

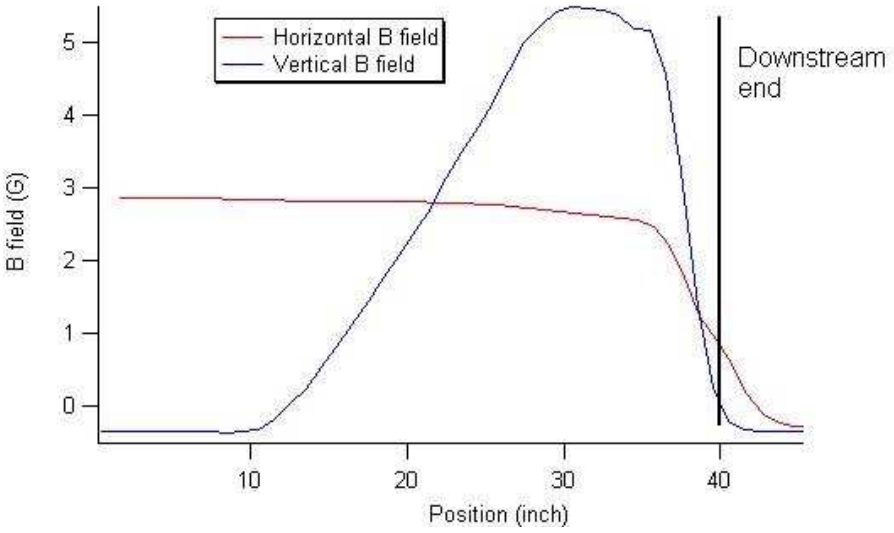


Figure 2.13: Magnetic field map of the output coil. The increasing vertical field is generated by the rotator coil and the flipping coil generates the horizontal field. The sign of the horizontal field flips at a rate of 1 Hz (thus the name flipping coil), rotating the spin vector alternately $\pm\pi/2$ radians into the polarization analyzer in the vertical direction.

spin adiabatically rotates by 90°. Alternating the current direction of the flipping coil effectively alternates the analyzer direction to measure the spin rotation angle (see Equation 2.6).

Similar to the input coil, the output coil also encloses a glass neutron transport guide (output guide) constructed from the same materials as the input guide. The difference is that the output guide has a 3.5 mm thick vertical partition, as shown in Figure 2.14, to separate the beam exiting from the left and right sides of the target chambers.

## 2.9 Ion chamber

To measure the neutron flux after the beam passes through the supermirror analyzer, we integrate the charge collected in a segmented ionization chamber filled with a $^3He$ and Ar gas mixture. Argon acts as a buffer gas to reduce the range of ions in the gas with a negligible effect on the neutron absorption and a low gamma sensitivity. The neutrons are

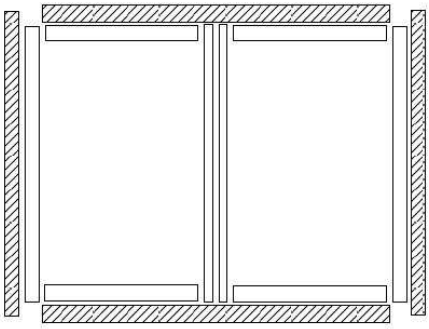

Figure 2.14: Cross section of the output guide. The shaded outer layer is Pyrex glass and the inner layer is Borofloat glass.

detected through the following reaction:

$$n + {}^3He \rightarrow {}^3H + {}^1H + 750keV \tag{2.10}$$

which produces charged reaction products that ionize the gas mixture. The average energy to produce an ion pair in the gas is 28 eV so approximately $2.5 \times 10^4$ ion pairs on average are produced per neutron absorbed.

As shown in Figure 2.15, a series of interspaced high-voltage (HV) and grounded charge collecting plates divide the detector into four collection segments. The charge collecting plates are the signal plates. This design was chosen to absorb neutrons of different velocities in different segments as lower-energy neutrons will be preferentially detected in the upstream segments. The PV contribution of the neutron spin rotation does not depend on neutron energy so the segmented design can be used to verify this property. Half voltage rings are placed between the collecting plates and the HV plates to help shape the electric field and reduce fringing fields and sparking.

Another unique design of this detector is that the collecting plates are each divided into four quadrants to detect neutrons from different parts of the beam, as shown in Figure 2.16. The left-right separation of the signal plates monitors the two sides of the experi-

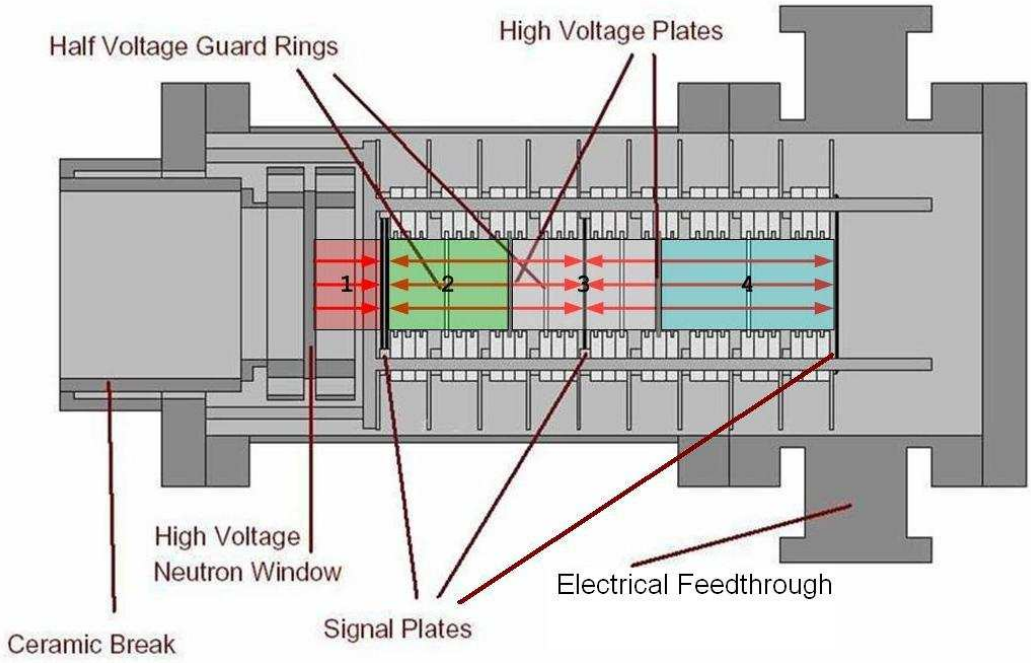


Figure 2.15: Side view of the ionization chamber with 4 detection segments.

ment separately. The up-down separation monitors the liquid He level and helps with the alignment.

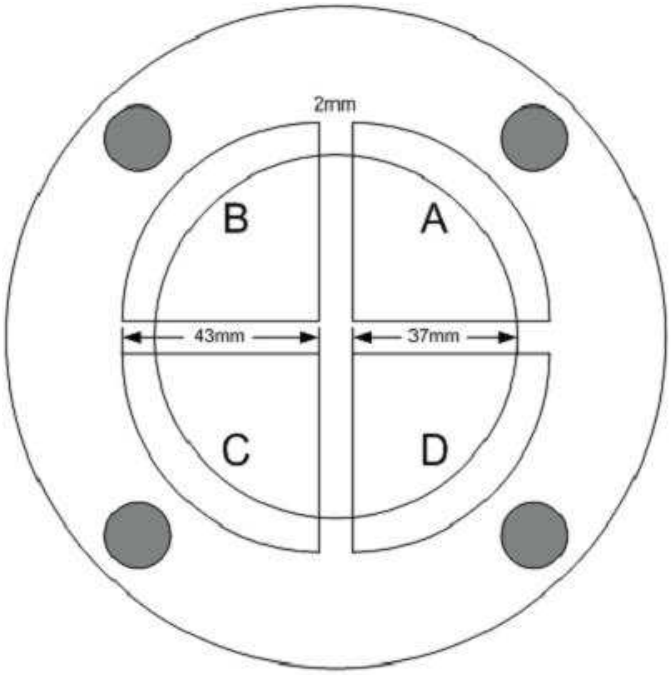


Figure 2.16: Frontal view of the signal plates divided into 4 quadrants [17]. The inner circle marks the opening for the beam and the small shaded circles are supporting posts.

# Chapter 3

# Magnetic Compensation System

## 3.1 Overview of the compensation system

Ambient magnetic fields can cause the neutron spin to precess, which can mimic the PV signal. To shield the experiment from Earth's magnetic field, 3 cylindrical $\mu$-metal shields were installed to reduce the longitudinal residual field to less than 50 $\mu$G in the target area, as shown in Figure 3.1. For our beam of neutrons with wavelengths between 2 $\mathring{A}$ and 14 $\mathring{A}$, a field of this size would cause the neutron spin to precess up to $3 \times 10^{-3}$ rad/m. This is extremely large compared to a PV rotation of a few $10^{-7}$ rad/m. The field also fluctuated on a time scale ranging from minutes to hours, due to the magnet fields from nearby experiments. I built a compensation system to keep the internal B field as low as 100 $\mu$G and suppress fluctuations. The schematic layout of the experiment in Figure 2.1 shows the compensation coil wound on the outer $\mu$-metal shield.

Figure 3.2 is a sketch of the compensation system, which is essentially a feedback loop. The fluxgate magnetometer was positioned inside the 2nd $\mu$-metal shield and the output was read by a proportional-integral-derivative (PID) controller through a buffer amplifier. The PID then controlled the current through the compensation coil to suppress the B field fluctuations. The DAQ also recorded the output of one of the internal fluxgates in the target

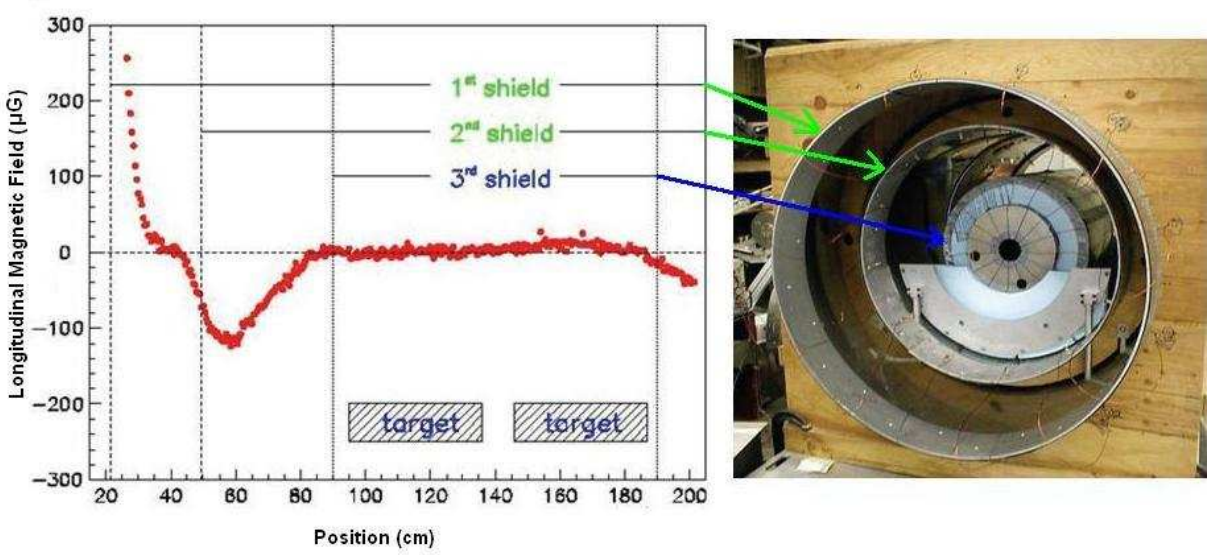


Figure 3.1: Longitudinal magnetic field measured inside the $\mu$-metal shields [17]. The innermost shield is right outside of the target insert. The end caps have been removed in the photo.

insert.

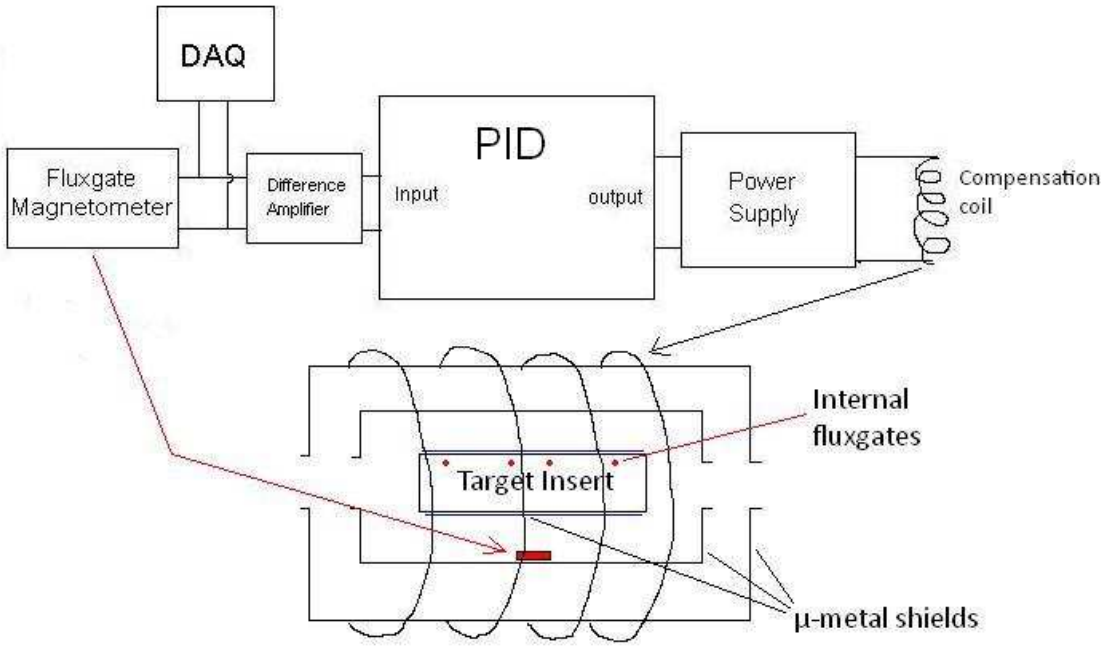


Figure 3.2: Compensation system

## 3.2 The compensation coil, fluxgate sensor and magnetometer

The compensation coil consisted of 14 turns of 1.5 mm diameter copper wires wound on the outer shield of the 2.4 m-long apparatus. The feedback flux sensor was placed inside the coils and the two outer shields, and oriented along the longitudinal axis. The single-axis fluxgate magnetometer is model Mag-01H from Bartington, shown in Figure 3.3. Its flux measure range is -0.5 G to 0.5 G with a resolution of 10 $\mu$G. The calibration of the magnetometer analog output is 0.1 G/V with a sensitivity setting at 10.

Figure 3.3: Bartington Mag-01H fluxgate magnetometer with sensor placed on the top.

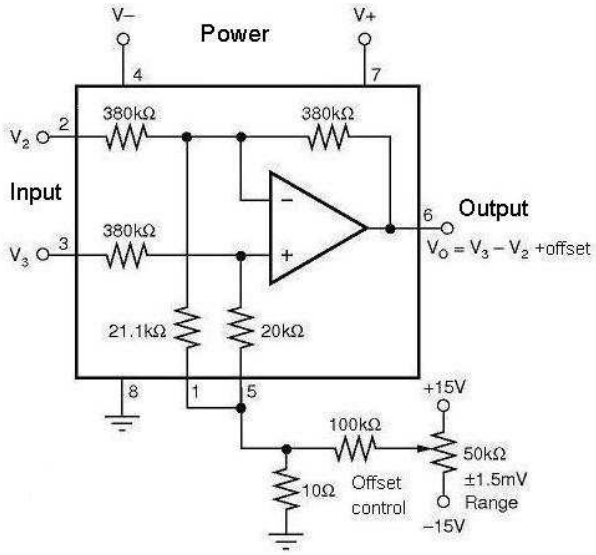


Figure 3.4: Difference amplifier circuit diagram

## 3.3 The difference amplifier

In order to record the B field, the DAQ had to read the magnetometer output in differential mode, which doesn't have a ground reference (neither of its 2 output leads is ground). Thus the PID, with a ground reference, had to be isolated from the rest of the system. The difference amplifier with unity gain acted as a buffer and provided a ground reference to the magnetometer output signal.

In the circuit diagram of Figure 3.4, $V_+$ and $V_-$ are $\pm$ 15V power for the amplifier. $V_2$ and $V_3$ are the input of the amplifier and were connected to the 2 output leads of the magnetometer, neither of which saw ground. The amplifier took the voltage difference between the 2 inputs, which is proportional to the measured B field, added a controllable offset to the difference and output the signal as $V_0$ in the figure. The PID read in $V_0$ with a reference to ground.

## 3.4 The proportional-integral-derivative (PID) controller

The PID controller takes a measured value from a process or other apparatus and compares it with a reference setpoint value. The difference, or "error" signal, is then used to adjust the PID output to the process in order to bring the measured value to its desired setpoint. Unlike simpler controllers, a PID can produce an output based on the history and rate of change of the error signal, which gives more accurate and stable control. The output of the PID controller is given by

$$Output = P \times (e + I\int edt + D\frac{de}{dt}), \tag{3.1}$$

where P, I and D are gains of the proportional, integral and derivative parts of the controller respectively. The error signal $e$ = Setpoint - Measure.

The integral term reflects the average of $e$ over the integral time, which is inversely proportional to the integral gain $I$. The derivative term reflects the rate of change of the error signal over the derivative time which is proportional to $D$. Reducing $D$ and increasing $I$ makes the PID more sensitive to rapid input changes, but a shorter history of the changes will be taken into account. Increasing $D$ and reducing $I$ has the opposite effect. Our PID controller had the following gain ranges: P = 0.1 to $10^3$; I = $10^{-2}$ to $5\times10^5$ $s^{-1}$; D = $10^{-6}$ to 10 s. Both the input and output ranges are -10 V to 10 V.

## 3.5 The result of compensation

Nearby experiments generated magnetic field fluctuations up to 100 $\mu$G in the target area and caused target state dependent B fields that would lead to a false PV signal, as discussed in Chapter 2.1. The top plot in Figure 3.5 shows the field fluctuations measured by the internal fluxgate with the PID loop inactive and the bottom plot shows the same conditions with the PID loop active. The compensation system successfully removes the field fluctuations and keeps the internal field stable at $\sim$100 $\mu$G. The PID controller was configured with P, I and D gains to be 1.6, 100 $s^{-1}$, and 1.1 ms respectively. For all production data runs the PID controller gains remained the same.

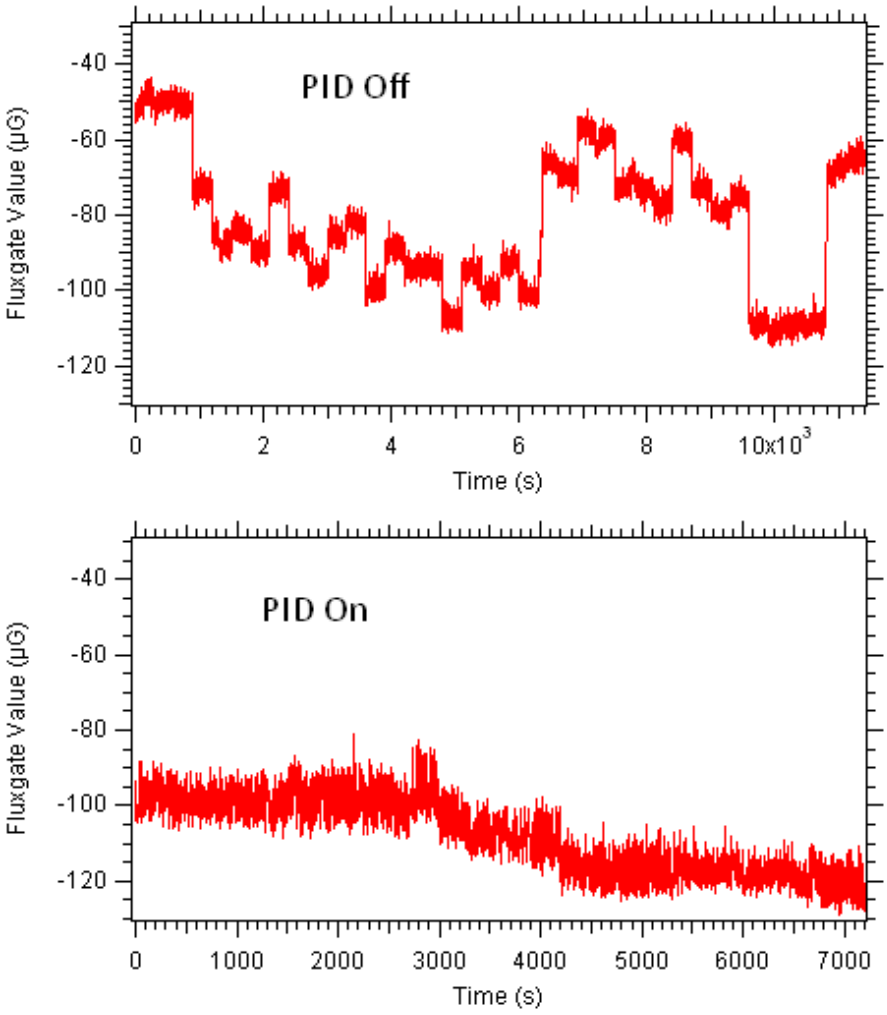


Figure 3.5: Magnetic field measurement inside the target insert with the compensation system off (top plot) and on (bottom plot).

# Chapter 4

# Data Measurements

## 4.1 Characterization of the neutron beam

Before the apparatus went online at NIST for production runs of PV spin rotation data, a series of measurements were performed to characterize the cold neutron beam. The initial neutron spectrum was measured as well as the total neutron fluence and beam intensity spatial distribution at various points along the beam line. The NCNR neutron beam is considered stable so that its characteristics are not expected to change in the production data period from January to June 2008.

### 4.1.1 Initial neutron spectrum

The initial neutron spectrum was measured by chopping the beam and measuring the time dependence of neutron intensity at a known distance. The chopper is made of $^6$LiF plastic glued to a phenolic disk that has two apertures 3.8 mm wide located at a radius of 15 cm. The disk rotated at 60 Hz and the neutrons were detected by a 10 cm by 10 cm, 0.4 mm thick $^6$Li/ZnS(Ag) scintillator coupled to a photomultiplier tube, through the reaction [18]

$$n +^6 Li \rightarrow^4 He +^3 H + 4.8MeV \tag{4.1}$$

The time-of-flight spectrum is converted to a beam wavelength distribution by using both the beam-line geometry and our prior knowledge of the origin of various features of the spectrum. Certain notches and discontinuities in the NG-6 spectrum are caused by diffraction from upstream materials, such as Mg in the beam windows, a graphite monochromator with wavelength selections at 4.8$\mathring{A}$ and 6$\mathring{A}$, a Be filter with cutoff wavelength at 3.98$\mathring{A}$, and a Bi filter. Figure 4.1 shows the measured neutron wavelength distribution with and without the Polarizing Super Mirror (PSM).

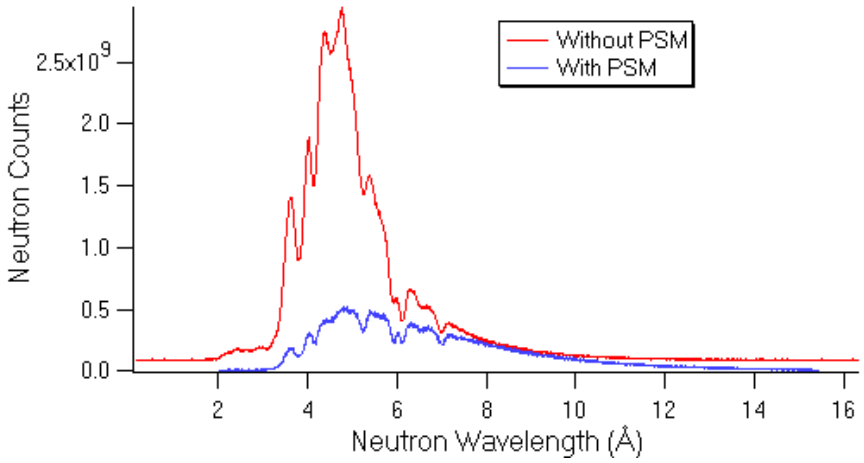


Figure 4.1: Initial wavelength distribution before NG-6 neutron beam enters our apparatus.

### 4.1.2 Spatial distribution of neutron intensity

Two methods of developing neutron images were employed [18]. One method uses an image plate with a powder mixture of BaFBr:$Eu^{2+}$ and $Gd_2O_3$ dispersed in a polymer matrix and supported by a flexible polymer sheet. This image plate material only needs a one-step process to extract the image but is sensitive to $\gamma$ radiation that is always present as background radiation in neutron experiments. The other method uses a natural dysprosium image plate with a high neutron capture cross section and a convenient half-life of 2.35 h.

After irradiation, the decay electrons from neutron absorption in $^{164}$Dy are exposed to a film that is sensitive to electrons and can be read out by an image reader.

Images were taken after the PSM, input coil and output coil. The intensity of the images shown in Figure 4.2 is linearly proportional to the neutron fluence but the proportionality factor is different for each image due to the different irradiation times. The top left image in Figure 4.2 shows the PSM blades and the top right image shows the input coil wires. The image after the output guide shows that the right side is more intense than the left side, consistent with the initial non-uniformity in the beam just after the PSM. In Chapter 6 the computer simulation shows that a gradient in the intensity across the beam will not cause a systematic effect as long as data are taken in both target states.

### 4.1.3 Neutron fluence measurement

A calibrated $^{235}$U fission chamber was used to measure the neutron fluence at various points along the apparatus. Because the fission chamber did not cover the full beam, two different methods were used to extrapolate the measurements to equivalent full-beam values: (1) measurements were performed at different locations across the beam and averaged, (2) measurements performed at known locations in the beam were combined with a full-beam image to determine the relative intensities. Table 4.1 shows the average neutron flux at various points along the apparatus.

Table 4.1: Average neutron capture flux measured at various positions along the apparatus [18]. Capture flux is the integral of the flux over the velocity distribution weighted by a factor of $\frac{v_0}{v}$ to take into account the velocity dependence for neutron absorption, $v_0 = 2200$ m/s by convention.

| Measurement position | Neutron flux ($\mathrm{cm^{-2}s^{-1}}$) |
|---|---|
| Before PSM | $1.2 \times 10^9$ |
| After PSM | $3.1 \times 10^8$ |
| After input coil | $1.5 \times 10^8$ |
| After output guide | $0.5 \times 10^8$ |

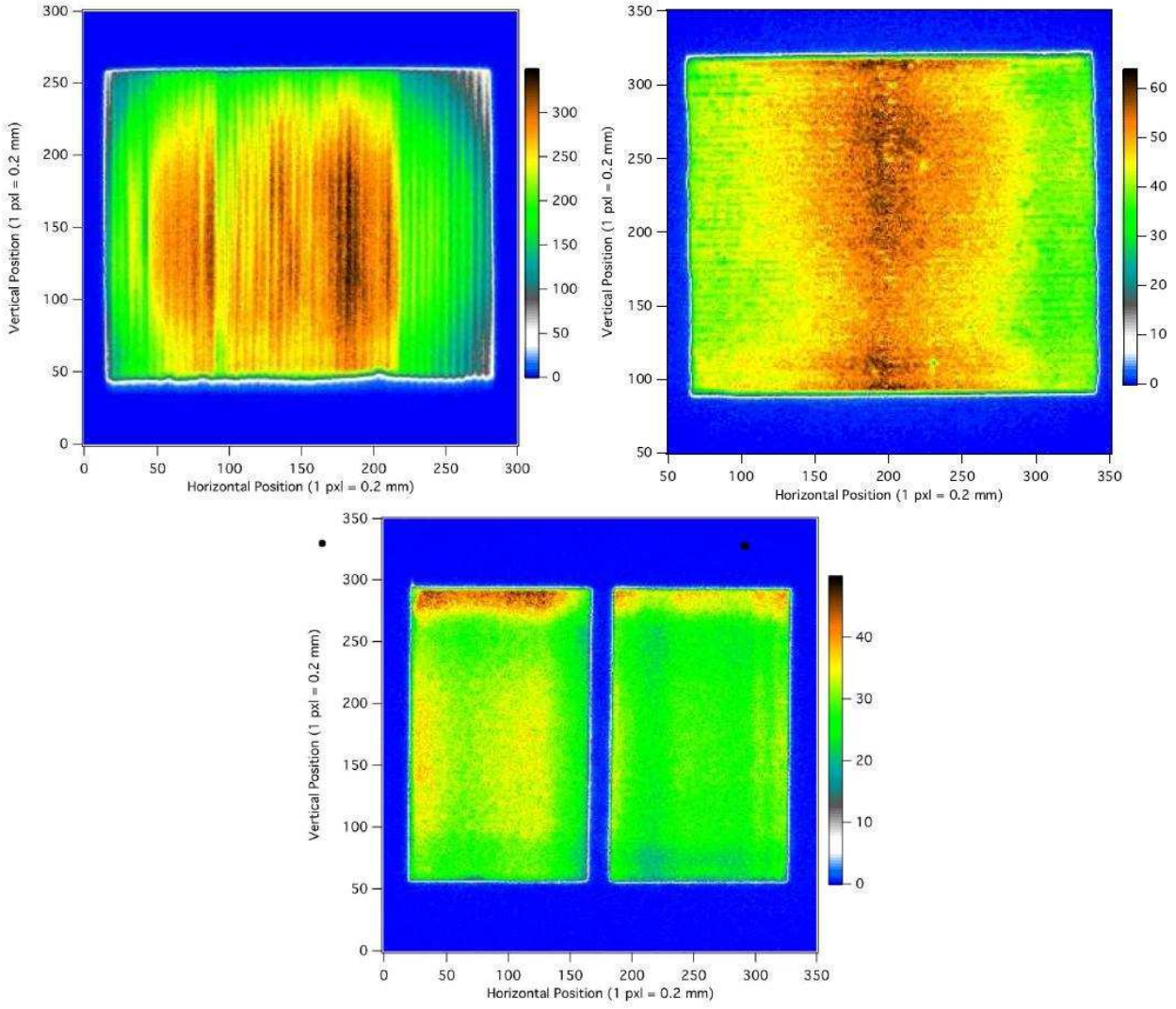


Figure 4.2: Beam images taken downstream of the PSM (top left), input coil (top right) and output guide (bottom) [18]. All images are looking upstream into the beam so that the left side of the image represents the right side of the beam.

### 4.1.4 Polarimeter measurements

Our spin rotation apparatus is essentially a polarimeter with the liquid He target between the polarizer-analyzer pair. The most important parameter for neutron polarimetry is the polarization product PA, the product of the polarizing power P and the analyzing power A. A PA measurement was conducted with the PSM and ASM to test our polarimeter without the liquid He target. The PA was measured by placing a non-adiabatic neutron spin flipper of known spin-flip efficiency [24] between the PSM and ASM and measuring transmission rates with the flipper off and on:

$$PA = \frac{N_u - N_f}{sN_u + N_f} \tag{4.2}$$

where $N_u$ and $N_f$ are the transmitted neutron intensities through the polarimeter with the spin flipper off and on, respectively, and $s$ is the spin-flip efficiency.

Figure 4.3 shows the wavelength-dependent PA measured with a chopper. A collimator was placed between the ASM and the detector to sample different parts of the beam (east, west and middle). These data show that the PA is a function of the neutron wavelength as well as the location across the beam. Section 7.3.1 will simulate the effect of the non-uniform PA on the PV spin rotation measurement and show that it does not increase the systematic error.

## 4.2 Data acquisition and control with the liquid $^4$He target

The spin rotation data were taken for each apparatus state determined by target state, $\pi$-coil state and output coil flipping state. Erik Swanson, a research professor at the University of Washington, wrote the computer program for data acquisition and control: NSAC (Neutron Spin-Rotation Acquisition and Control). It's written in Visual C++ with National Instruments Lab Windows CVI 7.0 for the graphical user interface (GUI) routines. A Dell

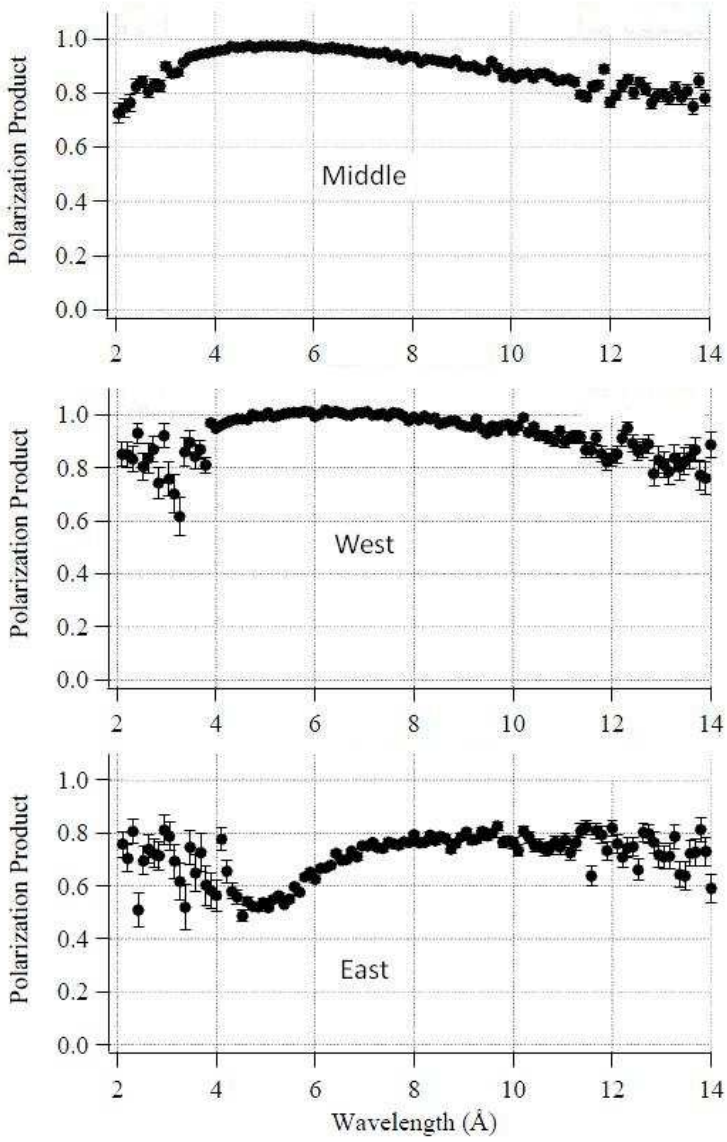


Figure 4.3: Measured polarization product PA as a function of neutron wavelength at the middle, west and east parts of the beam [18].

Dimension 8200 2.5GHz Pentium 4 computer with 512 MB of memory was used for data acquisition and experiment control.

The NSAC program controlled the output flipping coil state (+ and −) by reversing the current direction once every second. According to equation 2.6, measuring the neutron count rate at the detector for the + and − states and then calculating the asymmetry give the spin rotation angle

$$\varphi \approx \sin\varphi = \frac{N_+ - N_-}{N_+ + N_-} \tag{4.3}$$

where $N_+$ and $N_-$ are count rates for the + and − output flipping states, respectively.

The NSAC program also controlled the target state (0 and 1) described in Figure 2.3 by moving the drain pipes in the target (shown in Figure 2.9) so that the proper chambers were filled with liquid He. Because the detector is divided into left and right sides, the spin rotation angle (abbreviated as spin angle or rotation angle from here on) can be measured for each side and each target state. From the schematic diagram of the neutron spin in Figure 2.3 and equation 2.8, subtracting the spin angle of target state 1 from that of target state 0 gives 2 times the PV rotation ($2\varphi_{PV}$) for the left side, and $-2\varphi_{PV}$ for the right side, assuming the background magnetic field is independent of target state. Thus the difference between the PV signals from the left and right sides of the experiment is 4 times the PV spin rotation.

The NSAC program also controlled the current through the $\pi$-coil to step through the 3 $\pi$-coil states (0, 1, 2). States 0 and 2 had equal amounts of current in opposite directions, so that the effect of $\pi$-coil leakage fields is canceled. State 1 turned the current off for a null run: Revisiting Figure 2.3, turning the $\pi$-coil off will lead to the PV rotation getting canceled when subtracting the spin angle of target state 1 from that of target state 0, for both the left and right sides. Running in $\pi$-coil state 1 to see if a zero result is achieved is a systematic check on the apparatus.

Figure 4.4 shows the tagword for one complete target cycle. The apparatus state is associated with a tagword number for data recording. Each target cycle had 2 target states (0 and 1), 3 $\pi$-coils states (0, 1, and 2) cycled through 5 times for each target state, and 2 output flipping states (+, −). The output flipping coil flipped its current direction once every second and a total of 20 s (10 s for + and 10 s for −) of data were taken for each $\pi$-coil state. So each target state lasted 300 s and a target cycle contains 600 s of data. At the end of each target state, the NSAC program controlled the pump and drain pipes in the target to drain and fill the proper target chambers to switch to the other target state. The drain and fill time lasted 350 s for most of the production data runs. The target cycle was repeated until the end of a run when the liquid He was replenished in the target insert. The spin coil current direction was reversed from run to run to cancel any effects from its leakage field.

## 4.3 Polarization product runs with liquid $^4$He

The spin rotation angle calculated in Equation 4.3 assumes our apparatus is an ideal polarimeter but in reality it is not. Neither the polarizing power P of the PSM nor the analyzing power A of the ASM is 100%, so the rotation angle measured from the count rate asymmetry should be written as

$$PA \sin\varphi = \frac{N_+ - N_-}{N_+ + N_-} \tag{4.4}$$

which means that the actual rotation angle is the count-rate asymmetry divided by the polarization product PA. For an ideal polarimeter, PA is 1.

Because the PV rotation is calculated from the spin rotation angle $\varphi$ in Equation 4.4, the polarization product needed to be periodically measured during the time when the production data runs were taken. The PA was measured by rotating the spin coil around the beam axis, thus rotating the incoming neutron spin vector by a known angle, then

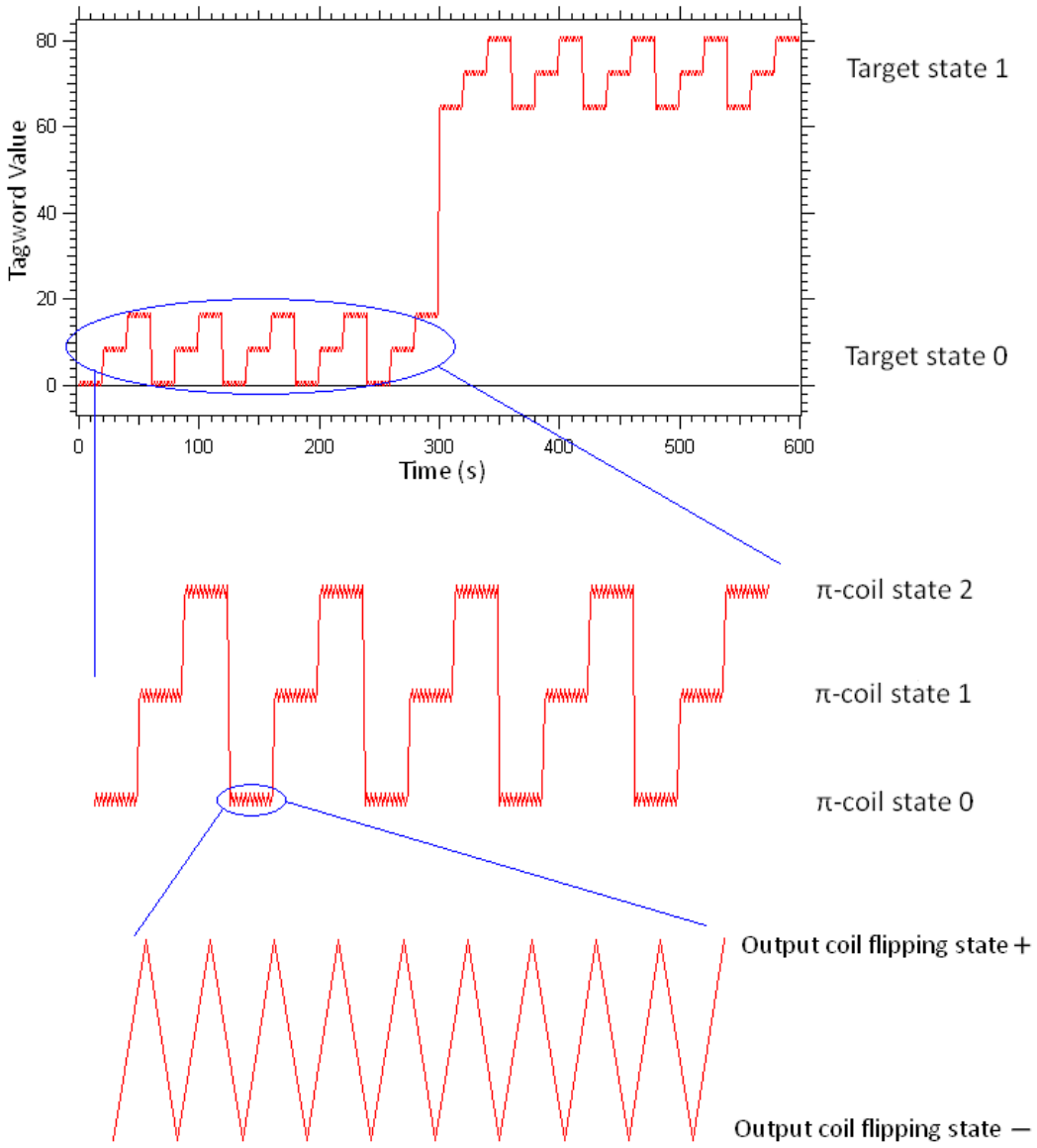


Figure 4.4: Tagword illustrating the apparatus state control sequence. The top plot shows 1 complete target cycle with 2 target states, 3 $\pi$-coil states and 2 output coil flipping states.

measuring the count-rate asymmetries before and after the rotation:

$$PA = \frac{(\frac{N_+ - N_-}{N_+ + N_-})_1 - (\frac{N_+ - N_-}{N_+ + N_-})_2}{\sin\varphi_1 - \sin\varphi_2} \tag{4.5}$$

where subscripts 1 and 2 refer to the spin coil positions before and after the rotation. Because the difference $\varphi_1 - \varphi_2$ indicates the amount by which the incoming neutron spin is rotated from the spin coil rotation, the polarization product can be calculated from the measured count-rate asymmetries before and after the spin coil rotation.

Figure 4.5 shows the measured PA during the period of liquid He production data runs. Changes made to the polarimeter, especially rocking and moving the analyzing supermirror (ASM), affect the polarization product value. Most observed changes in the PA had been identified by logbook entries. With this information, each block of data with constant run conditions was identified and had corresponding PA values. The PA for our polarizer-analyzer pair is about 75%. The $\pi$-coil reduces the polarization so the PA drops to $\sim$46% with the $\pi$-coil on.

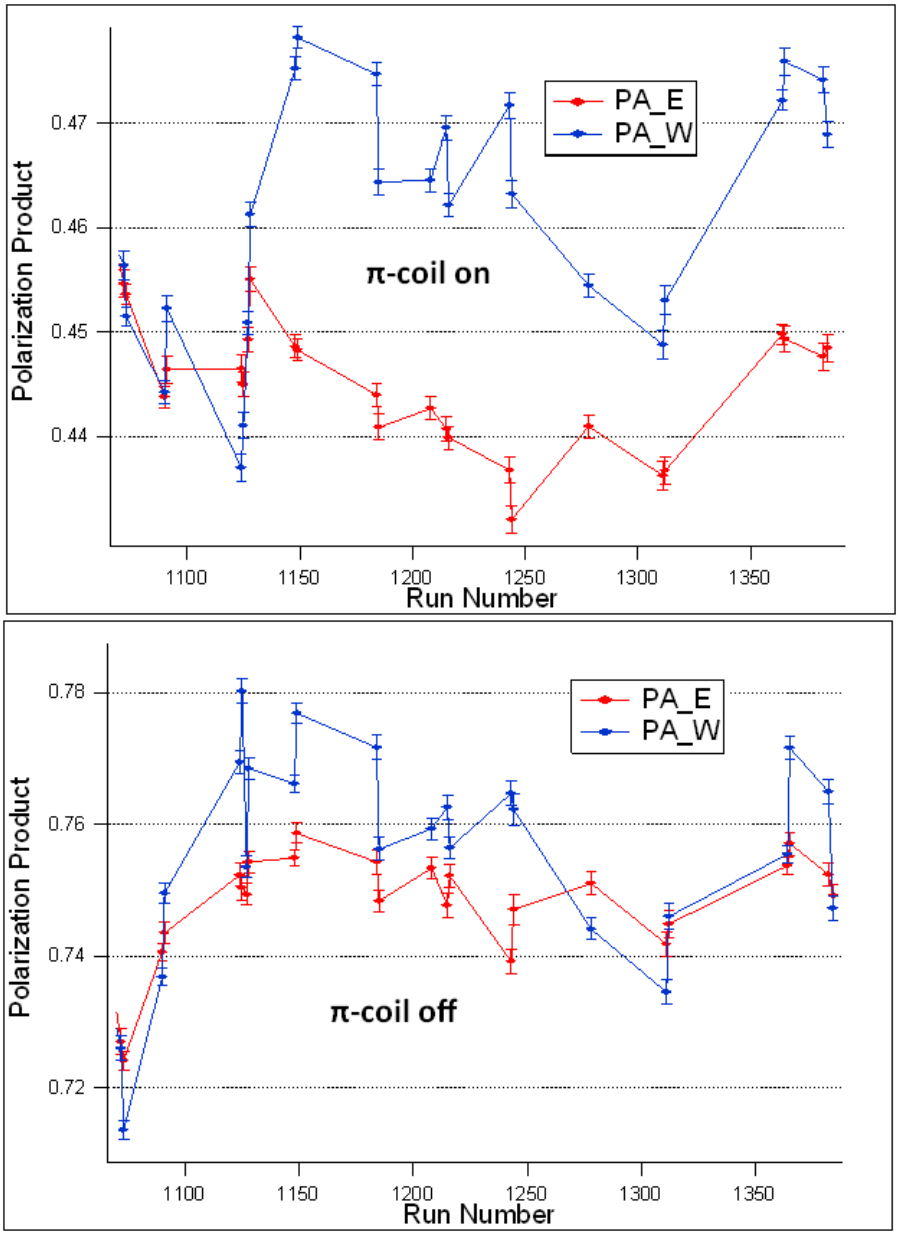


Figure 4.5: Polarization product PA measured throughout all 3 beam cycles when production data runs were taken. Measurements for the east and west sides of the experiment and with the $\pi$-coil on and off are shown.

# Chapter 5

# Data Analysis

## 5.1 Raw parity-non-conserving angle (PNCA) analysis

I used scientific data analysis software Igor Pro 5.01 to analyze the time series neutron count-rate data recorded by the NSAC program. The parity-non-conserving angle (PNCA) was extracted to find the PV neutron spin rotation through the liquid $^4$He target.

### 5.1.1 From count-rate asymmetry to PNCA

The time series count rate was recorded according to the apparatus status illustrated by the tagword shown in Figure 4.4 (2 target states, 3 $\pi$-coil states and 2 output flipping coil states). The count-rate asymmetry $A$ is calculated by

$$A(E,T,P) = \frac{N_+(E,T,P) - N_-(E,T,P)}{N_+(E,T,P) + N_-(E,T,P)} \tag{5.1}$$

$$A(W,T,P) = \frac{N_+(W,T,P) - N_-(W,T,P)}{N_+(W,T,P) + N_-(W,T,P)} \tag{5.2}$$

where $N_+$ and $N_-$ are the count rates for the 2 output flipping coil states, $E$ and $W$ refer to the east and west halves of the detector, $T$ is the target state ($T0$ and $T1$), and $P$ is the $\pi$-coil state ($P0$,$P1$,$P2$). Target state $T0$ has the east-upstream and west-downstream

target chambers filled with liquid He, while target state $T1$ has the west-upstream and east-downstream chambers filled. The $\pi$-coil is turned on in states $P0$ and $P2$ with the current in opposite directions, and state $P1$ has the current off.

According to Equation 4.3, the count-rate asymmetry $A$ is the spin rotation angle for various apparatus states. From the discussion in Chapters 2.1 and 4.2, the PNCA involves differences in asymmetries of the detector halves and target states. The $\pi$-on ($\pi$-coil turned on) $PNCA$ is

$$PNCA(E, P02) = \frac{1}{4}[A(E, T0, P0) - A(E, T1, P0) + A(E, T0, P2) - A(E, T1, P2)] \quad (5.3)$$

$$PNCA(W, P02) = \frac{1}{4}[A(W, T0, P0) - A(W, T1, P0) + A(W, T0, P2) - A(W, T1, P2)] \quad (5.4)$$

where $P02$ includes both $\pi$-on states ($P0$ and $P2$). And the $\pi$-on PNCA of the total detector is

$$PNCA(Total, P02) = \frac{1}{2}[PNCA(E, P02) - PNCA(W, P02)] \quad (5.5)$$

The $\pi$-off ($\pi$-coil turned off) $PNCA$ is

$$PNCA(E, P1) = \frac{1}{2}[A(E, T0, P1) - A(E, T1, P1)] \quad (5.6)$$

$$PNCA(W, P1) = \frac{1}{2}[A(W, T0, P1) - A(W, T1, P1)] \quad (5.7)$$

$$PNCA(Total, P1) = \frac{1}{2}[PNCA(E, P1) - PNCA(W, P1)] \quad (5.8)$$

for the east, west, and total detector.

### 5.1.2 Identifying and removing data with non-zero target asymmetry (TA)

Liquid He boiled off continuously during the course of the experiment, so that at the end of each production data run the liquid volume in the target insert was usually not sufficient for a proper fill. When that happened, the liquid level in the target chambers was not high enough to cover the whole neutron beam, and the data taken under this condition had to be removed from the final data set. The quantity most sensitive to the liquid level is the target asymmetry (TA), defined as the asymmetry between neutron count rates of the 2 target states:

$$TA(E) = \frac{N(E,T0) - N(E,T1)}{N(E,T0) + N(E,T1)} \tag{5.9}$$

$$TA(W) = \frac{N(W,T0) - N(W,T1)}{N(W,T0) + N(W,T1)} \tag{5.10}$$

where $N$ is the count rate. If the target chambers are filled properly the $TA$ should be zero.

Figure 5.1 shows the target asymmetries for the east and west halves of the detector and the $TA$ difference between the east and west for a typical production data run. After 7200 s the $TA$ deviates from zero which means the liquid He level is too low, and the data after that were not included in the final analysis.

### 5.1.3 Preliminary PNCA results for the liquid $^4$He target

Figure 5.2 shows the preliminary run-by-run PNCA results calculated with Equations 5.5 and 5.8 from the count-rate asymmetries. Each production data run only includes data that satisfy the TA condition discussed above. The weighted average PNCA with the $\pi$-coil on is

$$PNCA(Total, P02) = (-3.02 \pm 1.96) \times 10^{-7} rad \tag{5.11}$$

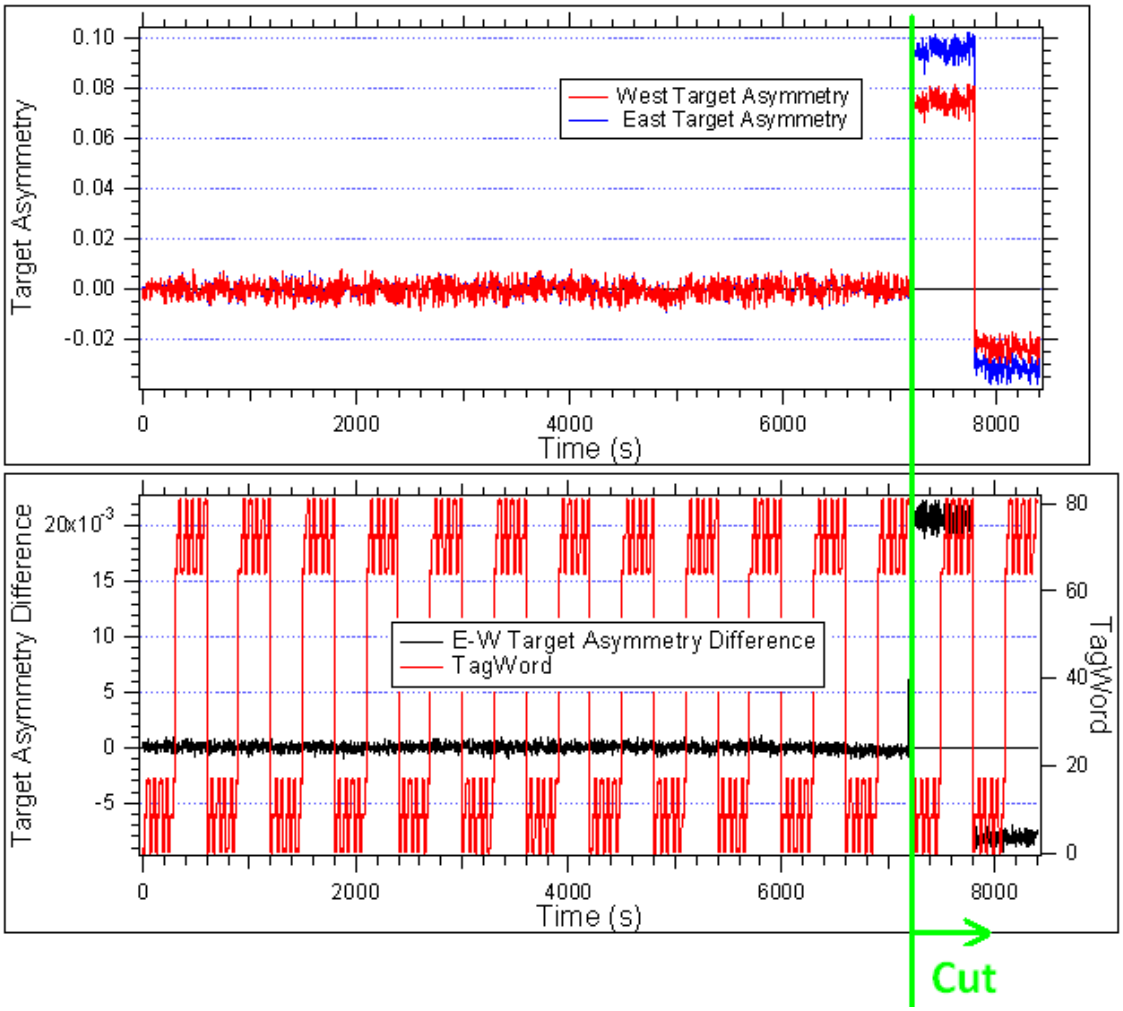


Figure 5.1: The top plot shows the TA for the East and West sides; the bottom plot shows the difference of the TA's and the TagWord as a function of time. The 2 target cycles after 7200 s were removed from the final data set.

with a total $\chi^2$ of 384 and 240 degrees of freedom (242 runs, $\chi^2/DoF = 1.6$). The $\chi^2$ statistics indicate the raw PNCA data set is noisy, i.e. the excessive spread of the PNCA from each data run suggests that it is very unlikely that the probability of the uncertainty in the data set is solely due to statistics.

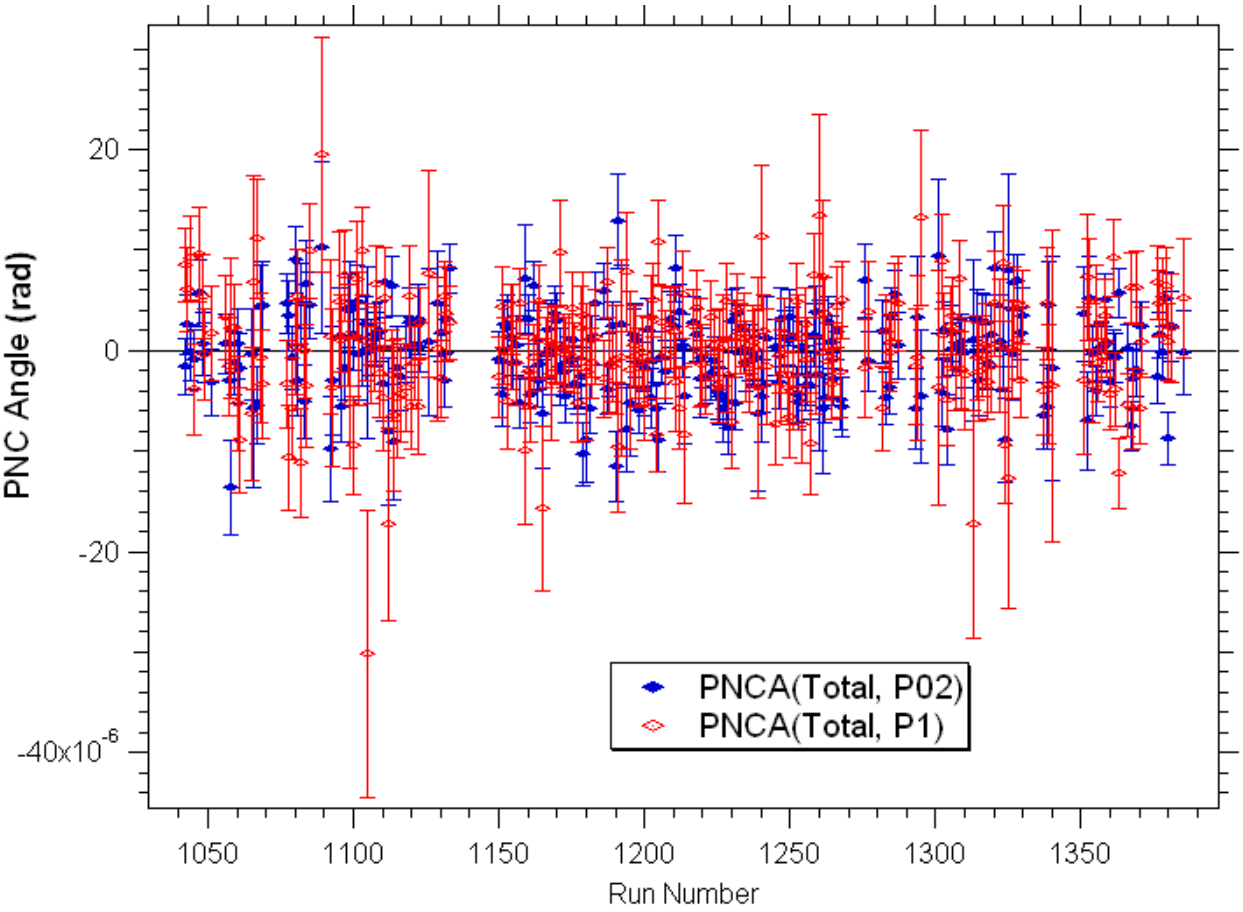


Figure 5.2: Preliminary run-by-run PNCA results with $\pi$-coil on (P02) and off (P1). A total of 242 runs, 22.0 days of live data were taken in 118 calendar days of beam time.

The weighted average $\pi$-off PNCA is

$$PNCA(Total, P1) = (3.58 \pm 2.77) \times 10^{-7} rad \tag{5.12}$$

with a with a total $\chi^2$ of 274 and 240 degrees of freedom ($\chi^2/DoF = 1.14$). The statistical

uncertainty in the $\pi$-off data set is much more probable (7%) than the $\pi$-on set but the central value is $1.3\sigma$ from zero. From the discussion in section 4.2, the $\pi$-off data should be zero and is a systematic check. This and the low probability of the $\pi$-on data set means further analysis was needed.

## 5.2 Regression technique with internal magnetic field drift

The count-rate asymmetry shown in Equations 5.1 and 5.2 are the spin rotation angles (SA) for various apparatus states. Note that SA only involves the addition of the asymmetries and no subtraction:

$$SA(E, P02) = \frac{1}{4}[A(E, T0, P0) + A(E, T1, P0) + A(E, T0, P2) + A(E, T1, P2)] \quad (5.13)$$

$$SA(W, P02) = \frac{1}{4}[A(W, T0, P0) + A(W, T1, P0) + A(W, T0, P2) + A(W, T1, P2)] \quad (5.14)$$

The $SA$ for the total detector with the $\pi$-coil on is

$$SA(Total, P02) = \frac{1}{2}[SA(E, P02) + SA(W, P02)] \quad (5.15)$$

The $\pi$-off spin angle is

$$SA(E, P1) = \frac{1}{2}[A(E, T0, P1) + A(E, T1, P1)] \quad (5.16)$$

$$SA(W, P1) = \frac{1}{2}[A(W, T0, P1) + A(W, T1, P1)] \quad (5.17)$$

$$SA(Total, P1) = \frac{1}{2}[SA(E, P1) + SA(W, P1)] \quad (5.18)$$

The value of spin angle shows how much the neutron spin rotates, thus it is an indication of the magnetic field condition. The top plot of Figure 5.3 shows the SA vs. time for a

typical run with a drift in the spin angle during the course of the run. Whatever caused this drift was apparently reset between runs because the SA of the following run returned to the lower value and then drifted up. This drift over the time of a run was present in all production data runs.

There are various mechanisms that could cause such a drift. One of the most likely is from the innermost $\mu$-metal shield. Unlike the other 2 shields, which are at room temperature, the inner shield is installed inside the 4K bore in the cryostat and its magnetic permeability is temperature-sensitive. During the course of a run, the liquid He level in the 4K volume and the target insert decreased due to boil off, creating a temperature gradient in the shield. That may have changed the shielding ability of the $\mu$-metal and caused the spin angle to drift. Recall that the liquid He was replenished between runs.

Another possible cause of the drift from the innermost $\mu$-metal shield is the change of stress in it. The shield is wrapped right outside of the target insert and the insert with the shield rests in the 4K volume. During the course of a run, the weight of the insert gets lighter due to the liquid He boil off, which changes the stress on the shield. The permeability of $\mu$-metal is known to depend on the stress in the metal, so that may also have caused the the spin angle drift.

The exact cause of the drift is not known, but it did cause each target state to have a slightly different B field condition than the target state right before it. This target-state dependence of B field condition will produce a false PNC angle (PNCA). To address this problem, a regression technique was used to eliminate the spin angle drift. As shown in Figure 5.3, the spin angle was fit with a 5th order polynomial, and the residual value of the fit for each point of the time series data was given to the new count-rate asymmetries. As shown in the bottom plot of Figure 5.3, the resulting spin angle no longer has the drift.

The PNCA was then calculated with the new regressed asymmetries, from Equations

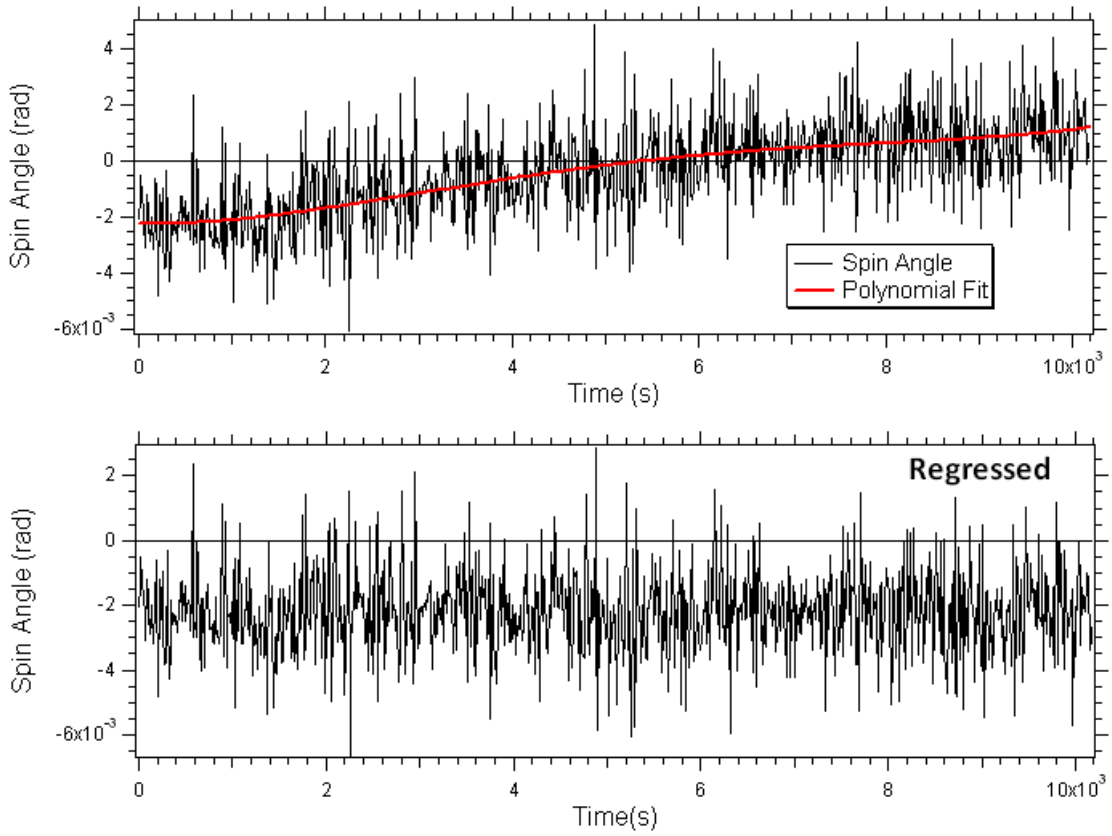


Figure 5.3: The spin angle from an individual run before (top plot) and after regression (bottom plot).

5.3 to 5.8. The weighted average PNCA for $\pi$-coil on is:

$$PNCA(Total, P02) = (-2.26 \pm 1.96) \times 10^{-7} rad \tag{5.19}$$

with a total $\chi^2$ of 317 and 240 degrees of freedom ($\chi^2/DoF = 1.32$). The 0.06% probability of this being random is still low, although it is a vast improvement from the result without regression (Equation 5.11). The $\pi$-off weighted average PNCA is:

$$PNCA(Total, P1) = (1.76 \pm 2.77) \times 10^{-7} rad \tag{5.20}$$

with a total $\chi^2$ of 233 and 240 degrees of freedom ($\chi^2/DoF = 0.97$). This is a significant improvement from the result without regression (Equation 5.12), as the $\pi$-off PNCA is now consistent with zero and the probability of randomness in the data set has increased from 7% to 62%.

## 5.3 Application of polarization product

Our apparatus is a non-ideal polarimeter, so the PV rotation measured by the apparatus (Equations 5.19 and 5.20) needs to be corrected by the polarization product. The PA values were measured frequently in all 3 reactor cycles when the production data runs were taken. As shown in Figure 4.5, the east and west sides of the experiment generally had slightly different polarization products. Additionally the PA values changed from one measurement to the next, sometimes with a fluctuation greater than the statistical uncertainty.

The PA fluctuations are due to changes made to the apparatus such as rocking the supermirror analyzer or tweaking the spin transport plates and magnets. For this reason I divided the data runs into groups according to beam-line events that may lead to a change in the polarization product. Each group of runs has a corresponding PA measurement and its PA value to correct their PNCA. Because the spin coil current is reversed after each data run, the PA measurement was always taken for both spin coil polarities. Table 5.1 shows

the measured PA values for their corresponding groups of runs.

Table 5.1: Measured polarization product for each data run group.

| Run number | Spin coil polarity | East $\pi$-on PA | West $\pi$-on PA | East $\pi$-off PA | West $\pi$-off PA |
|---|---|---|---|---|---|
| 1042 to 1069 | + | 0.4536 | 0.4515 | 0.7242 | 0.7136 |
| 1042 to 1069 | − | 0.4546 | 0.4664 | 0.7270 | 0.7260 |
| 1077 to 1089 | + | 0.4464 | 0.4523 | 0.7435 | 0.7495 |
| 1077 to 1089 | − | 0.4438 | 0.4442 | 0.7406 | 0.7369 |
| 1092 to 1123 | + | 0.4465 | 0.4370 | 0.7523 | 0.7695 |
| 1092 to 1123 | − | 0.4450 | 0.4410 | 0.7504 | 0.7802 |
| 1129 to 1133 | + | 0.4493 | 0.4509 | 0.7494 | 0.7536 |
| 1129 to 1133 | − | 0.4551 | 0.4613 | 0.7543 | 0.7685 |
| 1150 to 1183 | + | 0.4448 | 0.4698 | 0.7517 | 0.7613 |
| 1150 to 1183 | − | 0.4462 | 0.4765 | 0.7566 | 0.7743 |
| 1186 to 1214 | + | 0.4404 | 0.4633 | 0.7503 | 0.7564 |
| 1186 to 1214 | − | 0.4424 | 0.4722 | 0.7511 | 0.7672 |
| 1217 to 1242 | + | 0.4360 | 0.4627 | 0.7497 | 0.7594 |
| 1217 to 1242 | − | 0.4388 | 0.4707 | 0.7434 | 0.7638 |
| 1245 to 1268 | + | 0.4321 | 0.4632 | 0.7471 | 0.7623 |
| 1245 to 1268 | − | 0.4368 | 0.4717 | 0.7392 | 0.7648 |
| 1276 to 1323 | + | 0.4362 | 0.4488 | 0.7418 | 0.7346 |
| 1276 to 1323 | − | 0.4367 | 0.4531 | 0.7449 | 0.7460 |
| 1324 to 1363 | + | 0.4498 | 0.4722 | 0.7538 | 0.7555 |
| 1324 to 1363 | − | 0.4493 | 0.4759 | 0.7571 | 0.7717 |
| 1366 to 1385 | + | 0.4485 | 0.4689 | 0.7492 | 0.7473 |
| 1366 to 1385 | − | 0.4477 | 0.4742 | 0.7524 | 0.7650 |

From Equation 4.4, the actual neutron spin rotation angle is the measured rotation angle divided by the polarization product. However, our PNCA measurement requires both the east and west sides of the experiment and the PA is different for the 2 sides, so the west PNCA is normalized to the east. In the case of $\pi$-coil on, PNCA(W,P02) is divided by the ratio of the west product by the east product, before the total PNC angle is calculated from the difference between PNCA(E,P02) and PNCA(W,P02). The total PNCA is then:

$$PNCA(Total, P02) = \frac{1}{2}\left[PNCA(E, P02) - \frac{PNCA(W, P02)}{PA(W, P02)/PA(E, P02)}\right] \tag{5.21}$$

Since the west PNCA is normalized to the east side, both sides can be treated as having the same $\pi$-on product, i.e. the PA of the east side. The target downstream of the $\pi$-coil always sees a $\pi$-off polarimeter because the neutron beam carrying the downstream target's PV rotation doesn't get depolarized by the $\pi$-coil since the beam has already passed it. The PNCA from the upstream target, however, feels the depolarization from the $\pi$-coil because the beam goes through it while it is on. To get the actual PNC rotation angle $\phi_{PNC}$, the total PNC angle needs to be divided by the average polarization product from $\pi$-on and $\pi$-off:

$$\phi_{PNC} = \frac{PNCA(Total, P02)}{\frac{1}{2}[PA(E, P02) + \frac{1}{2}(PA(W, P1) + PA(E, P1))]} \tag{5.22}$$

With the $\pi$-coil off, the total PNCA is

$$PNCA(Total, P1) = \frac{1}{2}[PNCA(E, P1) - \frac{PNCA(W, P1)}{PA(W, P1)/PA(E, P1)}] \tag{5.23}$$

and the actual PNC rotation is

$$\phi_{PNC}(P1) = \frac{PNCA(Total, P1)}{\frac{1}{2}[PA(W, P1) + PA(E, P1)]} \tag{5.24}$$

Figure 5.4 shows the $\pi$-on and $\pi$-off PNC angles after spin angle regression and polarization product application. The weighted average PNC angle with the $\pi$-coil on is

$$\phi_{PNC} = (2.39 \pm 3.44) \times 10^{-7} rad \tag{5.25}$$

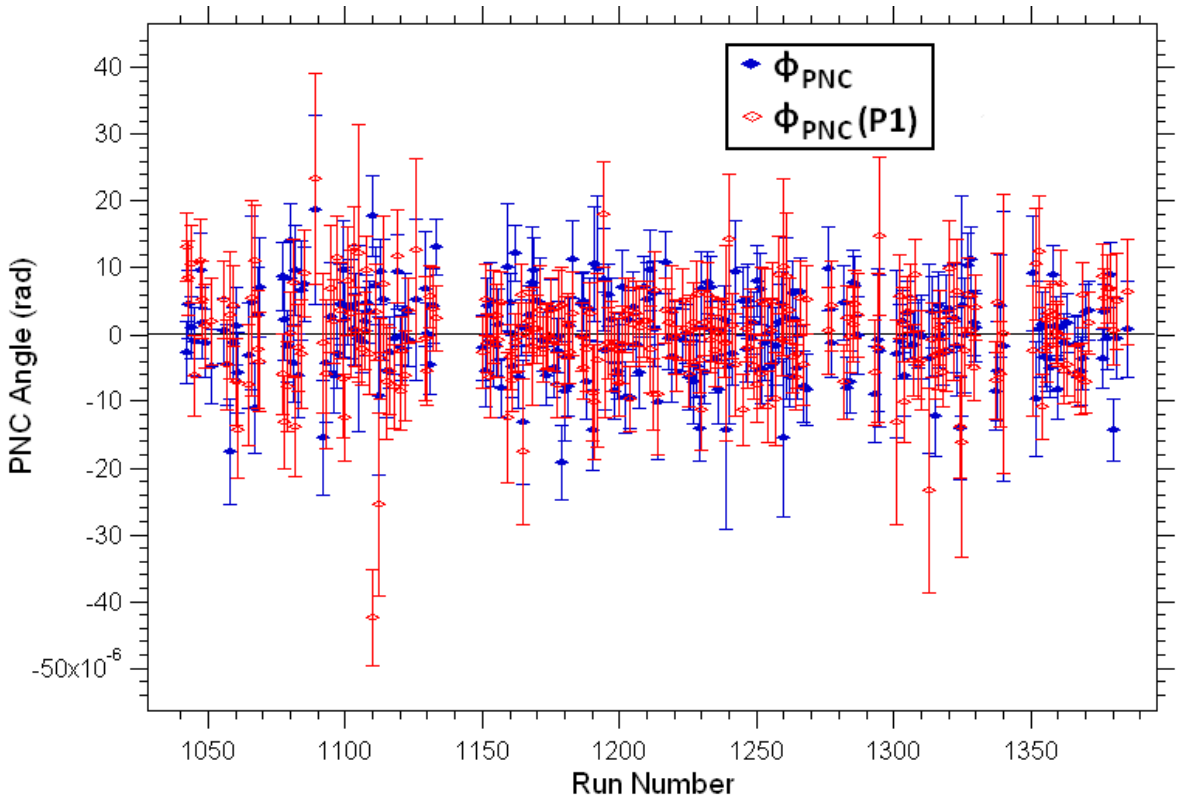


Figure 5.4: The PNC angle after regression with spin angle and polarization product application.

with a total $\chi^2$ of 297.6 and 240 degrees of freedom ($\chi^2/DoF = 1.24$). Compared to the result before PA application (Equation 5.19), the size of the error bar is inflated by roughly a factor of $\frac{1}{0.6} = 1.67$, the inverse of the average of $\pi$-on and $\pi$-off polarization products, and the central value is now consistent with zero. The $\chi^2$ probability has increased by an order of magnitude to 0.66%.

The weighted average $\pi$-off PNC angle is

$$\phi_{PNC}(P1) = (-1.06 \pm 3.73) \times 10^{-7} rad \tag{5.26}$$

with a total $\chi^2$ of 261.6 and 240 degrees of freedom ($\chi^2/DoF = 1.09$). Compared to Equation 5.20, the error bar is inflated by roughly a factor of $\frac{1}{0.75} = 1.33$, the inverse of the $\pi$-off PA, and the central value is still consistent with zero with a $\chi^2$ probability of 16.2%.

All the data runs have one of the two opposite spin coil polarities, which may explain the low $\chi^2$ probability of the $\pi$-on PNC rotation angle. To investigate this, the runs were divided into 2 groups with + and − spin coil (SC) polarities and the weighted average PNC angle calculated for each group:

$$\phi_{PNC}(SC+) = (2.18 \pm 4.85) \times 10^{-7} rad \tag{5.27}$$

$$\phi_{PNC}(SC-) = (2.59 \pm 4.87) \times 10^{-7} rad \tag{5.28}$$

the $\chi^2$ probability is 2.9% for the SC+ group and 4.5% for the SC− group.

To express the measured PNC neutron spin rotation in liquid $^4$He in rad/m, Equation 5.25 is divided by the length of the 4 target chambers (0.416 m):

$$\phi_{PNC} = (5.75 \pm 8.27) \times 10^{-7} rad/m \tag{5.29}$$

Equation 5.29 shows the central value and statistical error for the final result of our measurement. Chapter 7 will discuss the systematic errors.

# Chapter 6

# Computer Simulation

## 6.1 Introduction

A Monte Carlo computer simulation has been developed to study the parity-violating neutron spin rotation experiment in which a transversely polarized cold neutron beam is passed through a liquid $^4He$ target. The main use of the simulation is to investigate the size of possible systematic effects in the measurement from residual magnetic fields and neutron scattering in liquid $^4$He. If the B field is time-independent and the motion of the liquid helium upstream and downstream of the $\pi$-coil does not produce any difference in the precession angle of the detected neutrons, then the subtraction of the rotation angle for the two target states isolates the the PNC signal.

There are a number of effects associated with the scattering of the neutrons in the liquid helium that can cause such a difference in precession angle and consequently give a false PNC angle. For the neutrons scattered at small angles, the solid angle subtended by the two target positions upstream and downstream of the $\pi$-coil is different, so there will be a different fraction of the scattered neutrons that make it to the detector, and since the trajectories of these neutrons may not sample the exact same magnetic field and/or will spend slightly different times in the field, the spin rotation angles will be different. This is

why we have to simulate the neutron transport through the polarimeter and the scattering in the liquid helium target to quantify any systematic effect. Section 7.3 will discuss the simulation with amplified magnetic fields to compare to measurements for systematic effects.

## 6.2 Neutron transport and spin rotation calculation

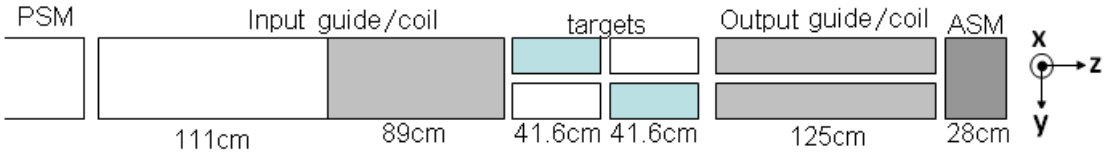


Figure 6.1: Top view of neutron transport through the apparatus

A schematic drawing of the experiment is shown in Figure 6.1. The simulation starts after the polarizing supermirror (PSM) and runs to the downstream end of the analyzing supermirror (ASM), where the detector is located. The ASM is not fully simulated, only its geometry and index of refraction (3 $mrad/\mathring{A}$) are used to determine the throughput. Rotations are calculated assuming a longitudinal field of 0.1mG, which is consistent with magnetic fields typically observed in the experiment. The initially vertically polarized neutrons pass through each component along the beam line and the spin rotation is the magnetic precession due to the longitudinal field:

$$\phi = \gamma_n B l / v \tag{6.1}$$

where $\gamma_n$ is the neutron gyromagnetic ratio, $l$ and $v$ are the path length and velocity in each beam component. In the target region, higher fields and gradients were applied to study various systematic effects. In the middle of the gap between the upstream and downstream targets, the rotation angle is reversed, simulating the effect of the $\pi$-coil.

The neutrons' starting positions are chosen randomly in the x and y directions (55 mm by 45 mm) downstream from the PSM and with isotropic trajectories within a given critical

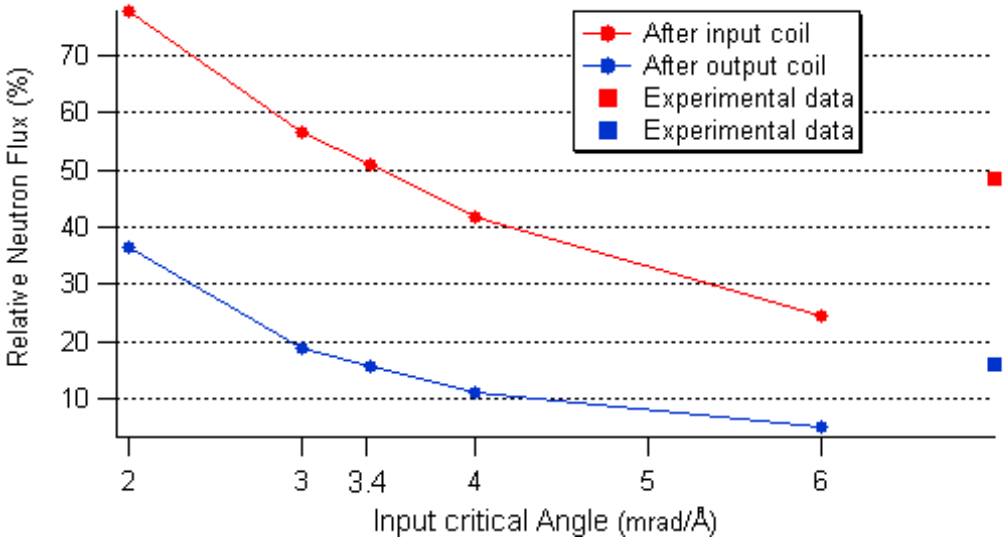


Figure 6.2: Relative neutron flux (100% after the PSM) vs. input critical angle. Both the experiment and simulated flux are with He gas in the target.

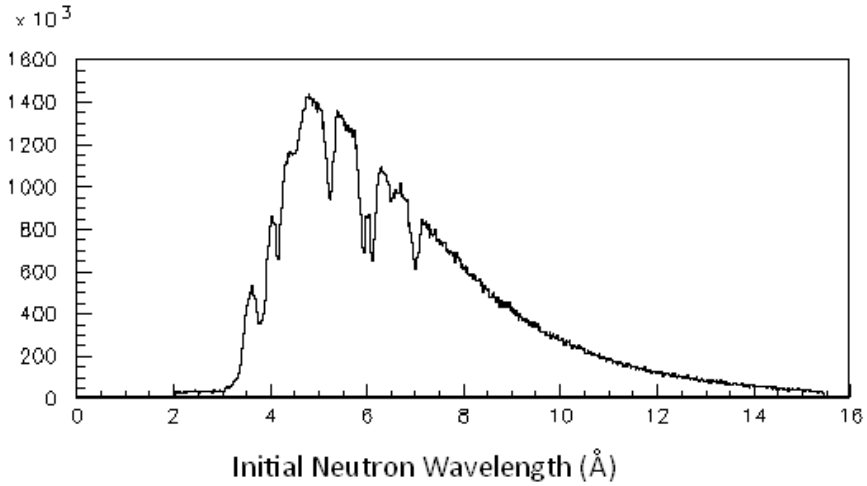


Figure 6.3: Initial neutron counts vs. wave length

angle. The critical angle is set to 3.4 $mrad/\mathring{A}$. This is larger than the NG6 value of 2 $mrad/\mathring{A}$, due to the increased divergence from reflection in the PSM. I chose the value of 3.4 $mrad/\mathring{A}$ to give rough agreement with the experimental results of the beam attenuation [18] after the input and output coils, shown in Figure 6.2. The initial neutron wavelength $\lambda$ is chosen from a distribution measured at NG6 [18] and shown in Figure 6.3. The initial energy and velocity are $(1/2m_n)(h/\lambda)^2$ and $h/(\lambda m_n)$, respectively.

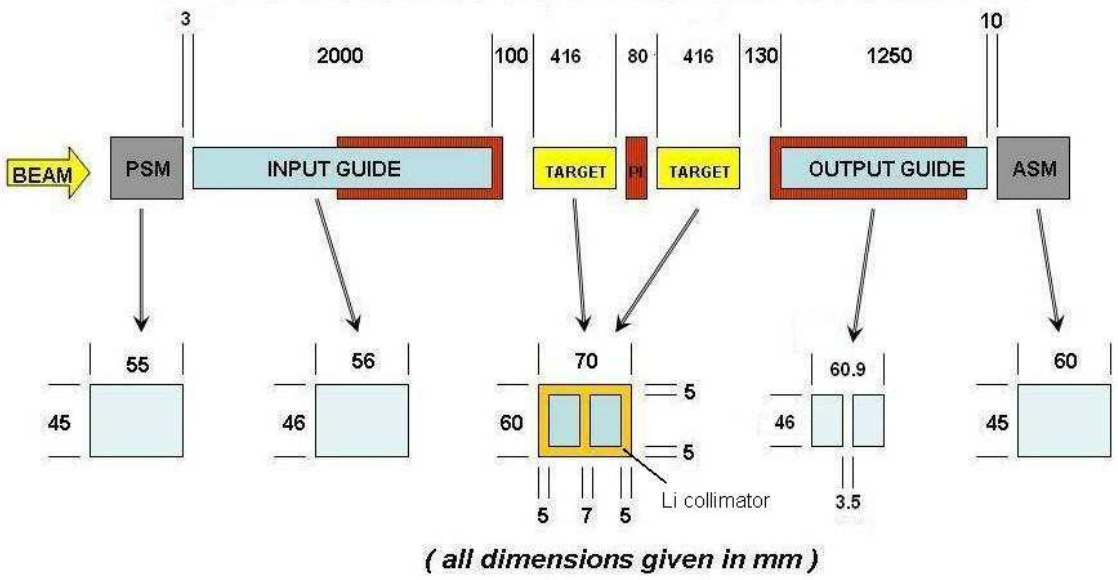


Figure 6.4: Cross-sectional dimensions of beam along apparatus

The neutrons then travel through the input guide, the upstream target, the $\pi$-coil region, the downstream target, the output guide, and the ASM before reaching the detector, where their spin rotation angles are tallied along with other parameters. Scattering in the air gaps between beam components and the Al windows was also simulated. Figure 6.4 shows the longitudinal and cross-sectional dimensions for each beam-line component and those values were used in the simulation. In the input and output guides, neutrons that hit the walls are mirror-reflected if their incident angle is less than the critical angle (1.2 $mrad/\mathring{A}$) and otherwise absorbed. In the experiment, the target has Li collimators to make sure no

neutron can be reflected back from the Al walls, as discussed in Chapter 2.6. To account for this in the simulation, any neutron that leaves the cross-sectional area of the target (26.5 mm $\times$ 50 mm side by side) will be lost. Both the target and the output coil have a septum in the middle so no East $\leftrightarrow$ West mixing can occur in those regions. This is also the case in the simulation.

## 6.3 Scattering in the liquid $^4$He target

The scattering of neutrons in the liquid He is problematic for the spin rotation experiment because some of the scattered neutrons will have a longer path length than the non-scattered neutrons, which means extra rotation due to the background B field. Since the detector acceptance angle is different for the upstream and downstream targets, this effect is target-state-dependent, which means it will produce a false PNC signal when we subtract the rotation of one side of the target from that of the other side. This is the main issue the simulation attempts to address. The simulation uses a polynomial fit to measured data [26] for the energy-dependent n-$^4$He total scattering cross section, shown in Figure 6.5.

The distance that neutrons travel before they scatter is defined by

$$D_r = -\frac{\ln(\frac{I}{I_0})}{\rho_{at}\sigma_{tot}} \tag{6.2}$$

where $I$ and $I_0$ are the number of non-scattered and incident neutrons respectively, $\sigma_{tot}$ is the fit to the total cross-section data in Figure 6.5 and $\rho_{at}$ is the atom number density for liquid He. A random number between 0 and 1 is used to express the ratio $\frac{I}{I_0}$. If $D_r$ is more than the target length (41.6 cm), the neutron won't scatter and will retain its energy and momentum. Otherwise it will scatter and obtain a new energy and momentum from the energy and momentum transfer values obtained in the method described in the next paragraph.

A simple model [20] for cold neutron scattering in liquid $^4He$ can be used to describe the differential cross section in terms of the dynamic structure factor $S(q,\omega)$ in Equation 6.3:

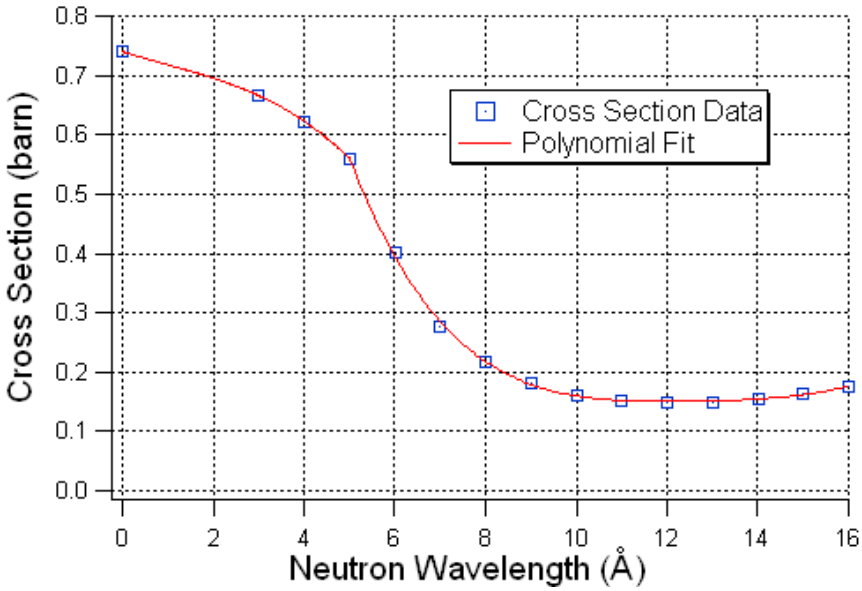


Figure 6.5: Neutron energy-dependent scattering cross section in liquid $^4$He.

$$\frac{d^2\sigma}{dEd\Omega} = b^2 \frac{k}{k_0} S(q,\omega) \tag{6.3}$$

where $b$ is the scattering length for a bound $^4He$ atom (3.077e-15 m), $k$ and $k_0$ are the wave numbers for the scattered and incident neutrons, and $\hbar\omega$ and $\hbar q$ are the energy and momentum transfer, respectively. Figure 6.6 shows a 3D plot of $S(q,\omega)$. The value of the dynamic structure factor is proportional to the probability of the corresponding $q$ and $\omega$, which in turn determines the momentum and energy transfer in the scatter.

The scattering in 4.2K $^4He$ gas, which fills the two empty target chambers, is also simulated, as well as scattering in the air gaps and Al windows along the beam. Cross sections for $^4He$ gas, Al and air (actually $^{14}N$, with a much bigger cross section than Oxygen) are obtained from Evaluated Nuclear Data File(ENDF)'s interpreted data.

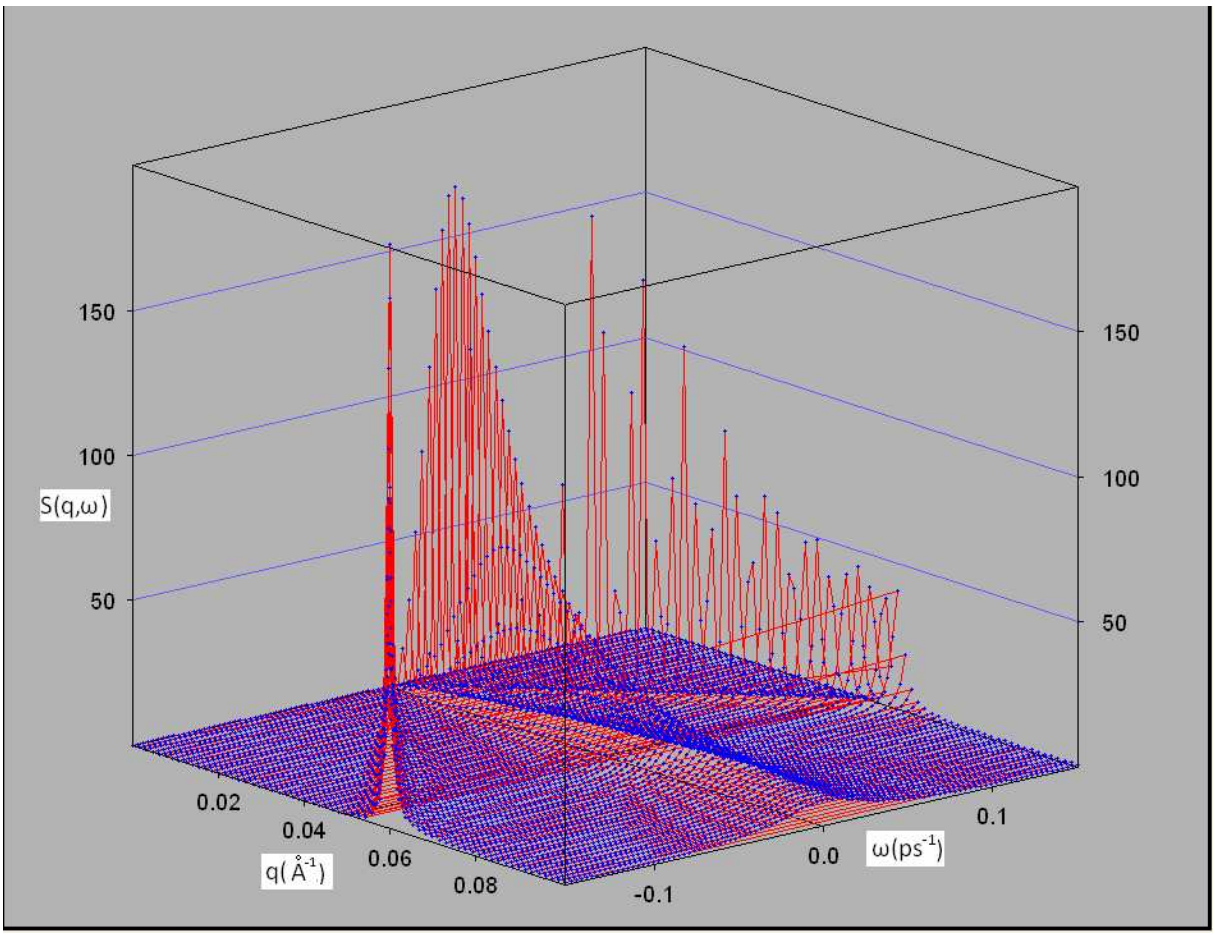


Figure 6.6: $S(q, \omega)$ 3D plot.

## 6.4 Ion chamber detector simulation

The ion chamber detector uses $^3$He gas to measure the neutron count-rate with the reaction shown in Equation 2.10. The depths of each of the four detector segments were measured to be 2.8, 6.4, 7.4 and 8.7 cm. The neutron counts as a function of energy before and after each segment were simulated as shown in Equation 6.4:

$$N_2(E_n) = N_1(E_n)e^{-\rho d\sigma(E_n)} \tag{6.4}$$

where $N_1$ and $N_2$ are respectively the neutron counts before and after each segment with energy $E_n$. $\rho$ is the number density of the $^3$He gas, $d$ is the depth of each segment and $\sigma(E_n)$ is the energy dependent n-$^3$He absorption cross section, as shown in Figure 6.7 [38].

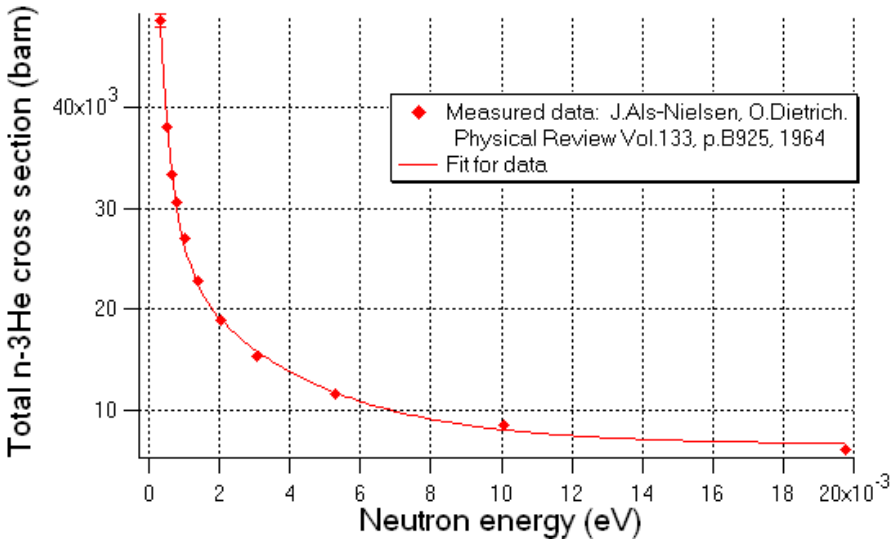


Figure 6.7: Measured n-$^3$He absorption cross section as a function of neutron energy with a fit to the data.

I used the simulated spectrum after the ASM as the input spectrum before the first (most upstream) detector segment to calculate the spectrum after each of the 4 segments with Equation 6.4. Figure 6.8 shows the simulated spectra after the 4 detector segments. The total number of neutrons entering and exiting each segment can be calculated by integrating the spectra before and after the segment. The difference between them is the number of

neutrons absorbed in that segment. Since the total number of neutrons entering the detector is known by integrating the spectrum entering the first segment, the segment-by-segment absorption ratio can be calculated.

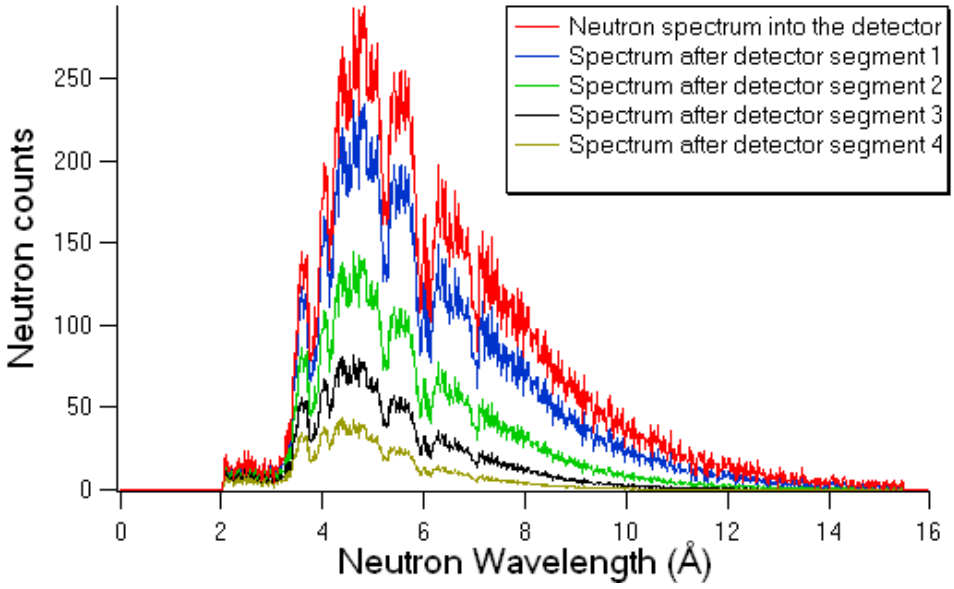


Figure 6.8: Simulated spectra into the detector and after each of the 4 segments.

Table 6.1 shows the simulated percentage of the neutron beam absorbed in each detector segment, in comparison with the data. The simulation is consistent with the data within a few percent for each segment.

Table 6.1: Percentage of neutron beam absorbed in each detector segment.

| Segment | 1 | 2 | 3 | 4 |
|---|---|---|---|---|
| Simulation | 25% | 35% | 20% | 11% |
| Data | 25% | 37% | 21% | 7% |

# Chapter 7

# Systematic Effects

There are many experimental conditions that will introduce systematic effects into our measurement of a PV spin rotation angle in the range of $10^{-7}$ to $10^{-6}$ rad/m. These sources of error can be classified into 3 groups: (1) the multiplicative effects that change the scale of the true PV rotation, (2) the effects that increase the measurement noise beyond $\sqrt{N}$, where $N$ is the total neutron counts, and (3) the systematic effects that produce a non-zero signal not due to the PV rotation. The first 2 groups are relatively straightforward to address while the discussion of systematic effects is more extensive and will be covered later in this chapter.

The multiplicative effects come from the non-ideal polarimeter for the measurement, which is accounted for in the polarization product, $PA$. With the expected size of PV neutron spin rotation in light nuclei being small and the intensity of our neutron source, it's hard to measure the spin rotation angle with better than 5% accuracy. So the polarization product need not be known to better than 5%, which is not difficult.

The two largest sources of noise above $\sqrt{N}$ statistics are neutron intensity fluctuations from reactor noise and extra noise in the ion chamber detector due to the current-mode measurement technique. The frequency band relevant to our spin rotation measurement is around 1Hz, from the output flipping coil. This is the frequency with which the spin

rotation angle is measured by alternating the projection of the spin vector into the analyzer (Equation 2.6). Although no precise measurements of reactor noise have been performed in this frequency range, both sub-beams for the east and west sides of the experiment come from the same guide so this noise source is expected to be common-mode to high accuracy and will be canceled by subtraction of one side from the other. This is indeed true as shown in Figure 7.1: the noise of the measured rotation angle is reduced by about an order of magnitude from the West-East subtraction.

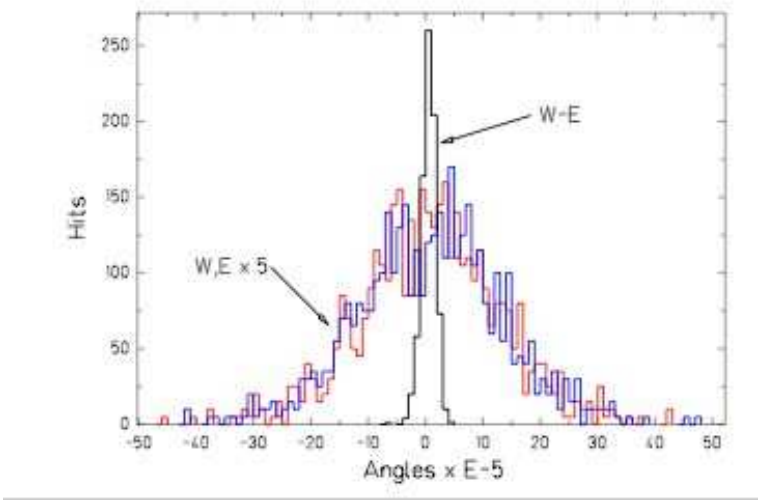


Figure 7.1: Measured spin rotation angles in the West (blue), East (red) and difference between West and East (black). Noise from beam intensity fluctuations is suppressed and width of W-E difference of rotation angles is $\sim \sqrt{N}$ statistics.

The extra noise added by the ion chamber in current mode can be calculated. Neutron capture in the $^3$He gas of the ion chamber produces about $2 \times 10^4$ ions per neutron, so the extra noise in the current signal is about 0.7% of the neutron counting statistics. In addition, the ion chamber is designed to absorb 90% of the incident neutron flux. Fluctuations in the fraction of the neutron beam absorbed in the ion chamber thus add about 3.2% extra noise above neutron counting statistics.

The dominant sources of experimental error for the PV spin rotation measurement are

the systematic effects that produce a false PV signal. The most serious systematic effects are associated, directly or indirectly, with residual longitudinal magnetic fields in the target area. Over the 1-meter long target area, the vertical spin of a $5\mathring{A}$ neutron will precess 2.5 mrad in a 100 $\mu$G longitudinal field, and estimates of systematic effects in the rest of this chapter will assume this residual field in the target area. If there is a $10^{-4}$ fractional difference in the B-field-induced spin rotation between the 2 target states, that effect is about the same size of our PV rotation. Chapter 7.2 will discuss a few manually induced magnetic fields under which measurements are taken to put upper bounds on B-field-induced systematic effects.

This chapter will discuss the systematic effects that can be analytically calculated or estimated, measurements taken to put upper bounds on systematic effects, as well as the computer simulation of some systematic effects.

## 7.1 Analytical calculation and estimation

### 7.1.1 Diamagnetism of liquid $^4$He

The presence of liquid helium changes the vacuum residual magnetic field due to its magnetic susceptibility, $\chi = -1.8914 \times 10^{-6} cm^3/mol$ [25]. For liquid $^4$He at 4.2K and 1 atm, the molar density is 0.0313 $mol/cm^3$. The resulting change in the residual field is $\Delta B/B = 5.9 \times 10^{-8}$. The spin rotation due to the diamagnetism of liquid He is less than $2 \times 10^{-10}$ rad/m, a factor of 1000 less than our PV rotation.

### 7.1.2 Optical potential of liquid $^4$He

The neutron optical potential in liquid $^4$He is about 10 neV. This means neutrons will slow down and spend more time in the liquid He, leading to more background rotation. For a $5\mathring{A}$ neutron with a kinetic energy about 3 meV, the fractional change in velocity with and

without the liquid helium is less than $2 \times 10^{-6}$. So this causes a systematic effect less than $5 \times 10^{-9}$ rad/m in the 100 $\mu$G longitudinal field. Again this is very small.

### 7.1.3 Shift in neutron energy spectrum

The neutron scattering cross section in liquid He is energy-dependent, which means the energy spectrum will shift slightly after the neutrons pass through the target. The magnitude of this shift also scales with the target length. From the known energy-dependent n-$^4$He total cross section [20] and our target length, the estimated average velocity shift is about 4%. The machining precision of the 41.6-cm long target chambers is 0.1 mm, which generates an effect less than $2.5 \times 10^{-8}$ rad/m with a 100 $\mu$G background field. This is less than a 1/10 of the PV rotation. Chapter 6 simulates the energy spectrum shift caused by scattering in the target to study the systematic effect on the PV rotation.

### 7.1.4 Small angle scattering

Not all neutrons pass straight through the liquid He target. A small fraction of neutrons scatter, elastically or inelastically, through small angles and reach the ion chamber detector. Since the distance between the target chambers and the detector is different for the chambers upstream and downstream of the $\pi$-coil, the solid angle subtended by the detector is different. This means the fraction of scattered neutrons depends on the location of the chamber filled with liquid He, so it's a target-state-dependent effect.

In addition, scattered neutrons travel a longer path in the residual magnetic field than those going straight through, so their rotation is also larger. This coupled with the target-state dependence of the fraction of scattered neutrons will give rise to a systematic effect. The size of this effect in general has to be calculated with the Monte Carlo simulation discussed in Chapter 6 to take into account the n-$^4$He scattering properties, neutron transport in the beam guides and the angular acceptance of the detector.

### 7.1.5 Change of neutron path due to gravity or reflection

There are factors other than scattering in the target that could change the neutron paths. If they are dependent on which target chamber is filled with liquid He, they may lead to a false PV rotation when coupled with the residual magnetic field. For example, the liquid He pressure is estimated to change by a factor of $10^{-3}$ over the height of the beam due to gravity. So there is a $10^{-3}$ change of liquid He density and the neutron optical potential. Obviously neither will give rise to any significant systematic effect. Another way for the neutron path to change is by reflection off the inner Al walls of the target chambers. Because the critical reflection angle is slightly different for the Al-liquid He interface and the Al-gas He interface, the fraction of reflected neutrons is target-state-dependent and their longer path length will cause a systematic effect. Chapter 2.6 has discussed the collimators inside the target chambers that are designed to block any reflected neutrons off the Al walls with wavelengths less than 20 $\mathring{A}$. According to Figure 4.1, our neutron spectrum ranges from 2 to 14 $\mathring{A}$, so the neutron reflection is totally suppressed in the target.

### 7.1.6 Non-uniformities in the polarization product

From Equation 4.4, the spin rotation angle is calculated from the measured neutron count-rate asymmetry divided by the polarization product $PA$:

$$\varphi = \frac{N_+ - N_-}{N_+ + N_-}/PA \tag{7.1}$$

Other than creating a multiplicative effect, the $PA$ could lead to systematic effects from its spatial non-uniformity and neutron energy dependence, as shown in Figure 4.3. If the polarization product is different for the east and west sides of the experiment, as shown in Figure 4.5, the two sides will have different rotation angles even with the same measured count-rate asymmetry. If that rotation angle difference between east and west is target-state-dependent, then it will have a systematic effect on the PV rotation angle.

In principle the size of the systematic effects from polarization product non-uniformities has to be simulated. This is especially important because the energy-dependent $PA$ is coupled with the target-state-dependent small-angle scattering, which is also energy-dependent. To give a rough estimation, consider this quantity

$$[(PA_E - PA_W)_{T0} - (PA_E - PA_W)_{T1}] \cdot F \tag{7.2}$$

where $PA_E$ and $PA_W$ are polarization products for the east and west sides, and T0 and T1 refer to target states 0 and 1, and $F$ is the fraction of scattered neutrons that reach the detector.

The quantity in Equation 7.2 indicates the fractional systematic effect from the non-uniform polarization product and small angle scattering. From Figure 4.5, the $PA$ difference between east and west is less than 5%, which is the same for both target states within 1%. The fraction of scattered neutrons that reach the detector is estimated to be less than 1%. The quantity in Equation 7.2 is estimated to be less than $5 \times 10^{-6}$. Multiplying that by the average rotation of scattered neutrons produces a systematic effect of $1.3 \times 10^{-8}$ rad/m, still small compared to the PV rotation.

## 7.2 Systematic measurements with liquid $^4$He

Most systematic effects discussed in section 7.1 directly couple with residual magnetic fields in the target area, so 10 trim coils were wrapped around the target insert to produce large B fields to study their effects. The current through each trim coil was individually controlled to generate any B field condition. Figure 7.2 shows the positions of the trim coils and the 4 fluxgate sensors on top of the two liquid He targets.

Liquid He runs were taken with the trim coils producing a large B field and a large B field gradient for systematic effect studies. Simulations were carried out to quantify any systematic effect due to those magnetic fields. The comparison of the simulated and

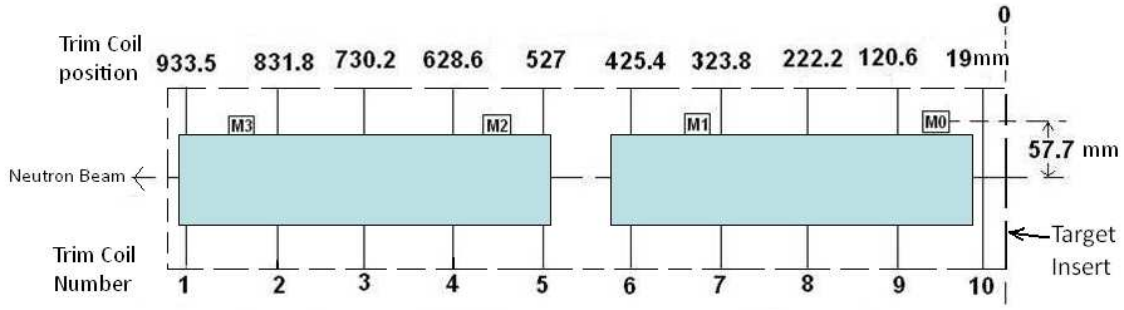


Figure 7.2: Trim coil positions relative to the liquid He targets. The 4 fluxgate sensors (M0, M1, M2 and M3) are located on top of the 2 targets.

measured results will be discussed later in this chapter.

### 7.2.1 Large B field

A current of 80 mA was applied through all trim coils to study the effects of a large field in the beam direction. For computer simulation purposes, a field spatial profile was calculated from the superposition of the fields generated by each trim coil's circular current with the Biot-Savart law:

$$B = \sum_{i=1}^{10} \frac{\mu_0 I a^2}{2[a^2 + (z - x_i)^2]^{3/2}} \tag{7.3}$$

where $I$ is the current through the trim coils, $a$ is the radius of the trim coils (14.4 cm), $z$ is the position along the beam and $x_i$ is the position for each trim coil. As shown in Figure 7.3, the calculated field matches the fluxgate readings well with 80 mA through the trim coils.

Figure 7.4 shows PNC angle measurements with 10, 5, and 2.5 mG fields in the target area. A line fit of the $\pi$-on PNCA limits the slope under $4 \times 10^{-10}$ rad/$\mu$G, which translates to $4 \times 10^{-8}$ rad/m with a 100 $\mu$G internal field.

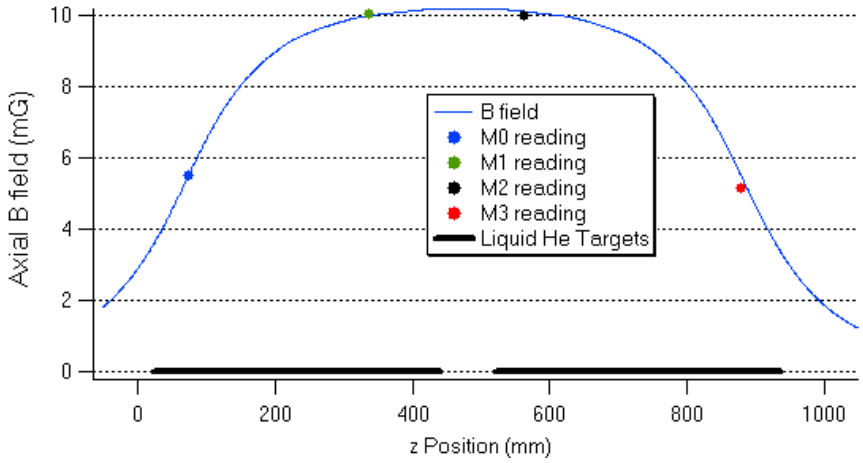


Figure 7.3: Large B field in the target area produced by trim coils.

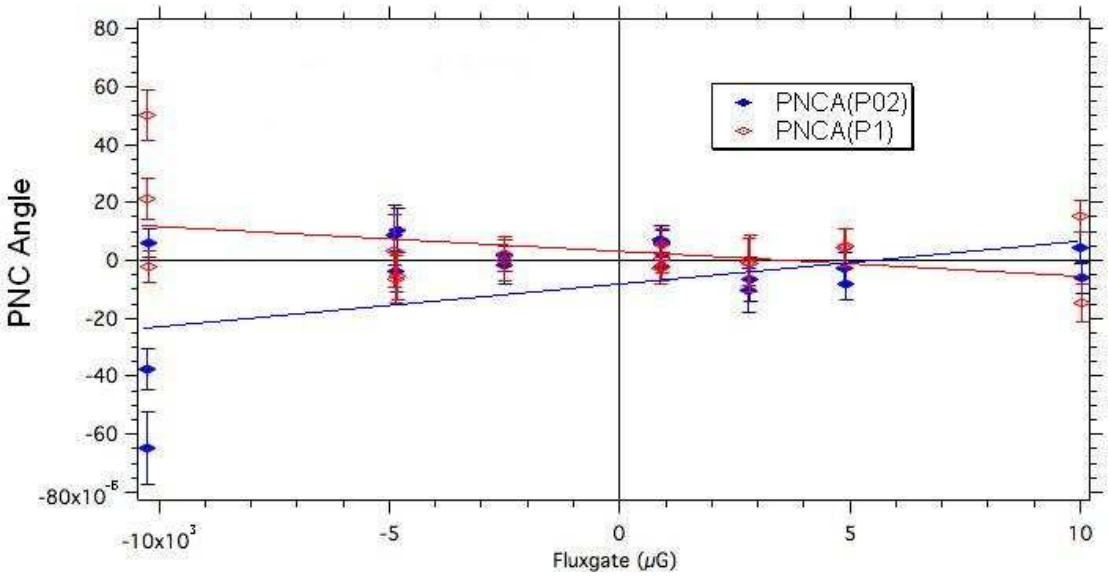


Figure 7.4: PNC angle measurements with large B fields in the target area.

### 7.2.2 Large B field gradient

Because the $\pi$-coil flips the sign of the neutron spin rotation angle, a magnetic field gradient with the 2 targets in B fields of opposite directions would lead to a larger overall rotation angle than a uniform field. To study the effects of gradient fields, a large field gradient was produced with each trim coil running a different current, as shown in Figure 7.5.

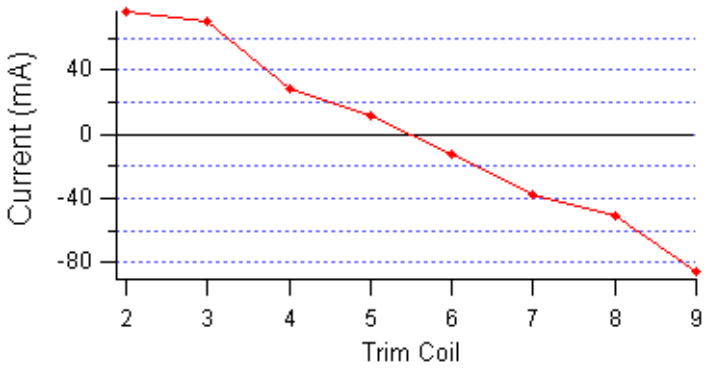


Figure 7.5: Current for each trim coil to produce a large B field gradient.

The gradient field calculated from those currents with Equation 7.3 matches the fluxgate readings well close to the upstream and downstream ends but not in the middle section of the target, as shown in Figure 7.6. This may be because the trim coils are very close to the innermost $\mu$-metal shield and may have magnetized it at the middle where the field changes direction.

Figure 7.7 shows the PNC angle measurements with the large gradient field produced by the trim coils. The weighted average of the $\pi$-on PNCA is $(-2.0 \pm 3.1) \times 10^{-6}$ rad/m. This applied gradient is 2 orders of magnitude larger than the average measured gradient in the data runs ($\sim$200 $\mu$G/m), so the upper bound of the systematic effects from internal B field gradient is $3 \times 10^{-8}$ rad/m.

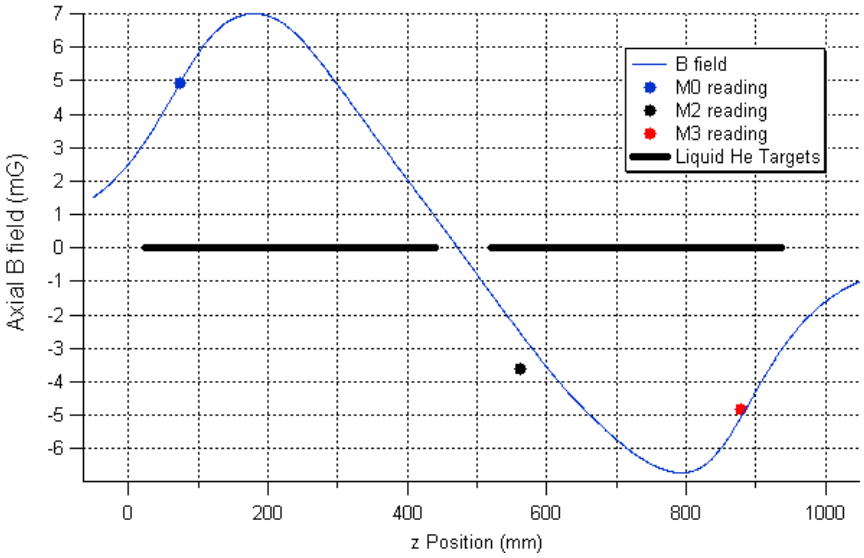


Figure 7.6: Large B field gradient in the target area produced by trim coils.

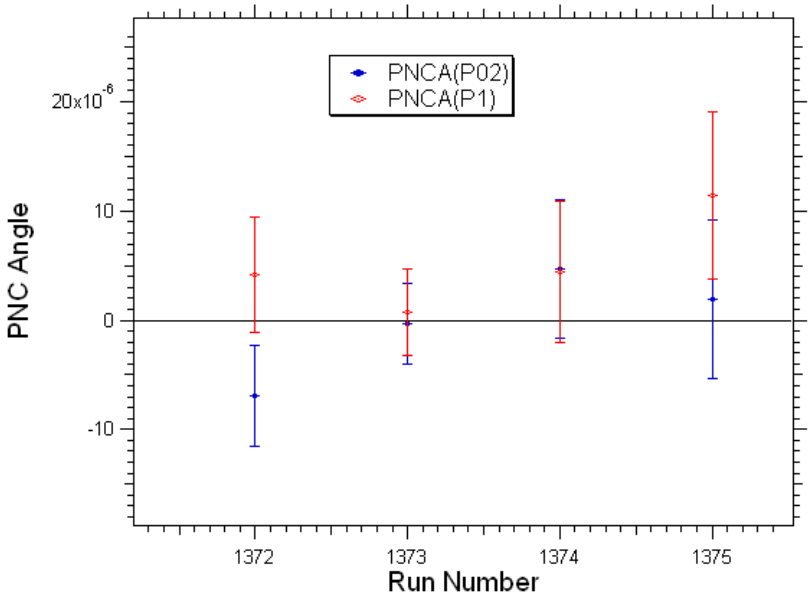


Figure 7.7: PNC angle measurements with a large B field gradient.

### 7.2.3 Polarization product non-uniformity

To amplify the effects of non-uniformities in the polarizing supermirror (PSM) and the analyzing supermirror (ASM), the output coil was rotated to introduce large known misalignments of the polarizer and analyzer axes. Figure 7.8 shows the PNC angle measurements with the output coils rotated at one extreme position (first 2 runs) and the other extreme position (last 2 runs). The difference between the two positions in weighted average PNC angles is $(4.6 \pm 4.9) \times 10^{-6}$ rad per 80 mrad misalignment. This scales down to a $6 \times 10^{-8}$ effect, with an average misalignment of 1 mrad in the production data runs.

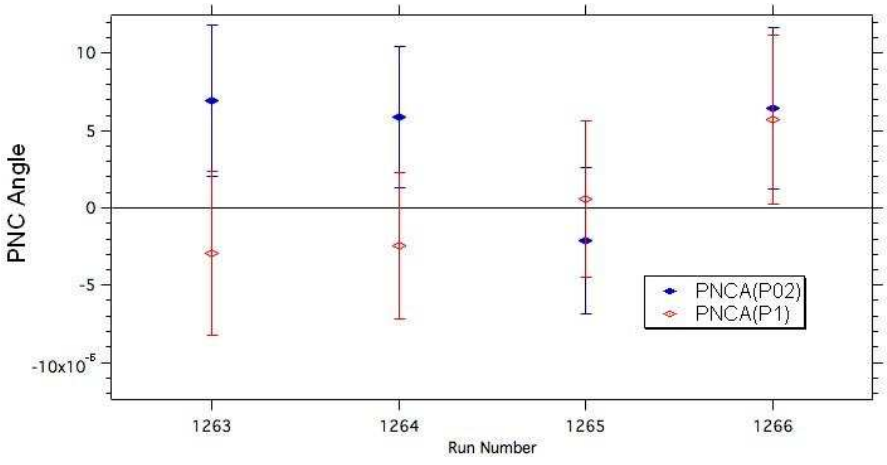


Figure 7.8: PNC angle measurements with a large B field gradient.

## 7.3 Simulation with magnetic fields

As mentioned before, due to different detector acceptance angles for target positions upstream and downstream of the $\pi$-coil, the number of scattered neutrons that make it to the detector depends on the target location from which they scatter. Their spin rotation, which is different from that of unscattered neutrons due to a different trajectory and amount of time in the B field, is target-state-dependent and might cause a false PNC signal. I applied amplified magnetic fields in the target area in the Monte Carlo simulation discussed in Chapter 6 to quantify their systematic effects and compare to our measurements in Section

7.2.

### 7.3.1 Simulation for gradient systematic runs

A large B field gradient was applied in the experiment so the upstream and downstream targets had longitudinal background fields in opposite directions. The gradient was produced by running current through the trim coils wrapped around the target insert. The trim coil positions are shown in Figure 7.2 and the current value for each trim coil is shown in Figure 7.5. The current going through the trim coils was set up symmetrically upstream and downstream of the $\pi$-coil with opposite signs, as shown in Figure 7.5. Unfortunately, at the time these data were taken, fluxgate M1 was not working. Readings of the remaining fluxgates were made immediately before the data were taken.

The B field spatial profile for the simulation is calculated with a superposition of the contributions from all trim coils. For each trim coil, the Biot-Savart Law for circular current is used to calculate the longitudinal field. Running current through the trim coil magnetizes the cryoperm shield around the target canister, so the field profile is magnified by a factor of 1.24 to agree with fluxgate readings, shown as the corrected field in Figure 7.9. The average gradient in the target is about 12 mG/m. The spin rotation is calculated with Equation 6.1. For non-scattered neutrons whose velocity doesn't change, $Bdl$ ($Bdz$ in Figure 7.9) is integrated from the upstream end of the target (point A in Figure 7.9) to the downstream end (point C) and for the corresponding range of the downstream target. In the gap between the upstream and downstream targets, the rotation is calculated from point C to the middle of the $\pi$-coil, rotated 180° around the vertical axis, and then is calculated from the middle of the $\pi$-coil to the upstream face of the downstream target.

Neutrons that scatter have different velocities before and after the scattering and the time they spend in a section of the B field differs accordingly (the simulation considers no

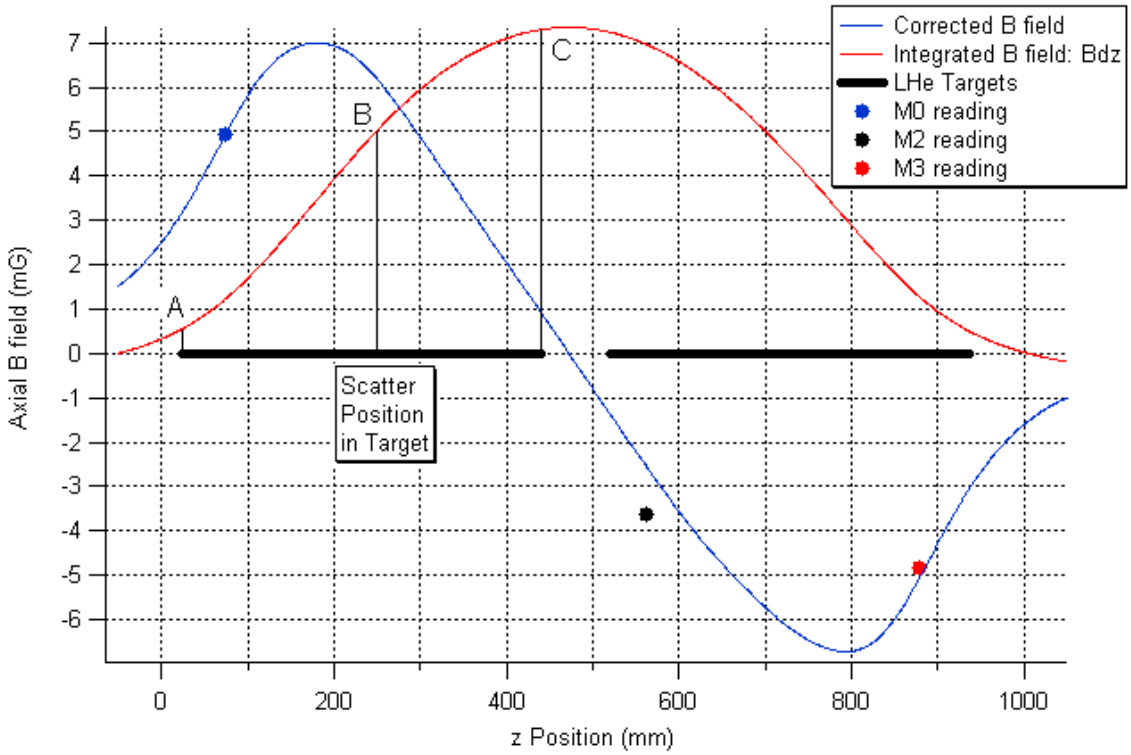


Figure 7.9: Field profile for gradient systematic runs. The calculated field from trim coil currents is corrected by multiplying a factor of 1.24 to match the fluxgate readings. The large scale of the integrated field $Bdz$ is reduced so it can be shown on the same figure. The target positions upstream and downstream of the $\pi$-coil are also shown.

more than 1 scatter in each target position). To account for this, the program integrates from A to the scatter position B, then from B to C, and uses Equation 6.1 twice with the velocities before and after the scatter. The simulated spin angle at the detector (120 mrad) is close to the measurement from data runs for this study (98 mrad). The PNC angle is calculated by dividing the spin rotation difference between west and east by 2. The simulated PNC angle is $(-0.7 \pm 2.7) \times 10^{-6}$ rad, consistent with the measured $(-2.0 \pm 3.1) \times 10^{-6}$ rad.

Simulation studies were also done to investigate the possible systematic effect of the non-uniform polarization product shown in Figure 4.3. The wavelength-dependent PA was used in the simulation at the end of the ASM as the probability for a neutron to survive and have its spin rotation tallied. The part of the ASM (east, middle, or west) where the neutron comes out also affects the PA, as shown in Figure 4.3. The simulated PNCA is $(-3.2 \pm 2.9) \times 10^{-6}$ rad with the wavelength-dependent non-uniform PA, consistent with the experimental result of $(-2.0 \pm 3.1) \times 10^{-6}$ rad, which indicates that the non-uniform polarization product does not cause a systematic effect, even with an large applied field gradient in the target area.

### 7.3.2 Simulation for a production data run with the greatest recorded field gradient

Among the data runs with all 4 fluxgate readings recorded, run 1154 has the greatest range. The average gradient between the most upstream and downstream fluxgates is 0.616 mG/m. The B field fit for the fluxgate readings, shown in Figure 7.10, is used as the field profile to simulate the spin angle and PNC angle.

Table 7.1: Simulated spin angle and PNC angle compared to data for run 1154

| | Simulation | data |
|---|---|---|
| Spin Angle (rad) | $(-1.54 \pm 0.02) \times 10^{-5}$ | $(-465 \pm 3.64) \times 10^{-5}$ |
| PNC Angle (rad) | $(-0.125 \pm 1.4) \times 10^{-7}$ | $(11.6 \pm 37.0) \times 10^{-7}$ |

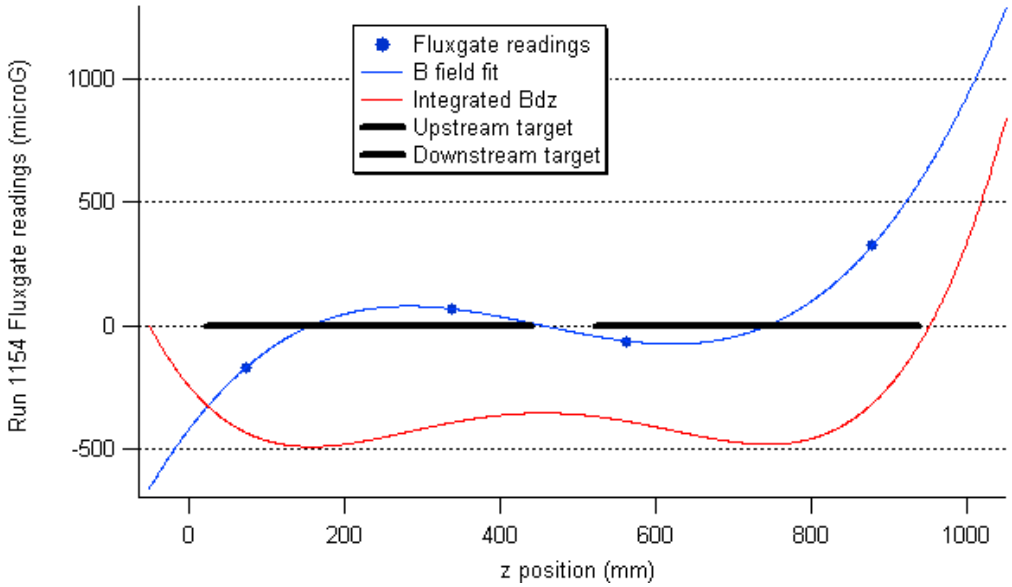


Figure 7.10: B field gradient for data run 1154. The fluxgate readings are fit with a 3rd order polynomial.

As shown in Table 7.1, the simulated PNC angle matches well with the experimental result but the simulated spin angle does not. Since data run 1154's gradient is 20 times smaller than what has been simulated for the gradient systematic runs, it's not surprising to have the simulated PNCA be zero within $1.4 \times 10^{-7}$ rad. Since the simulation assumes a 0.1 mG longitudinal field in the input and output guides as wells as the air gaps, the greater rotation from data could be caused by higher fields in those beam components other than the target.

### 7.3.3 Simulation for data taken with large uniform field

A current of 80 mA was applied through all the trim coils to study the effect of a large uniform field. To simulate those runs the field profile was again produced from a superposition of all trim coils with the Biot-Savart Law. It was then magnified by a factor of 1.09 to match the fluxgate readings, shown in Figure 7.11. The spin rotation for scattered and non-scattered neutrons are calculated the same ways as discussed in Section 7.3.1. Although

most of the target region has a field as large as 10 mG, the flipping of the $\pi$-coil reduces the overall rotation to about 2 mrad. The simulated PNCA is $(-1.67 \pm 0.60) \times 10^{-6}$ rad, consistent with the measured $(-0.88 \pm 2.24) \times 10^{-6}$ rad.

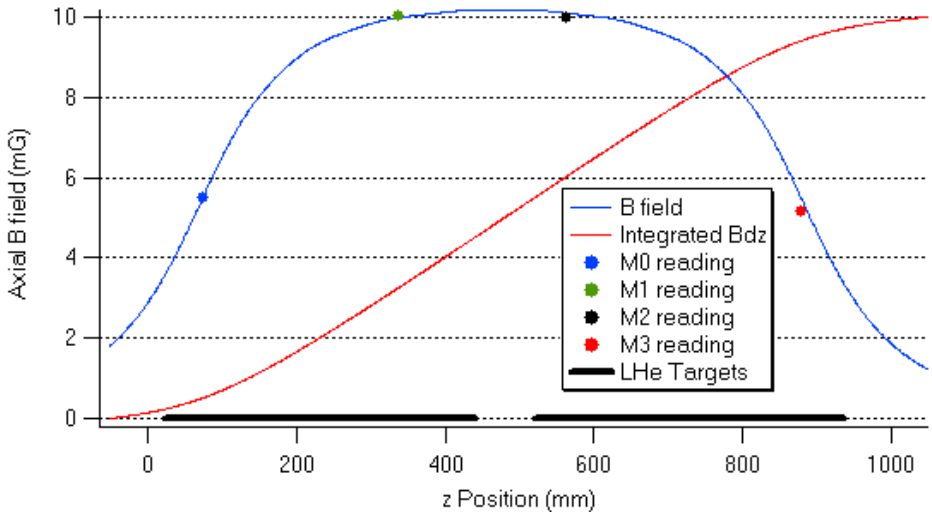


Figure 7.11: Field spatial profile for data runs with a large uniform field in the target region.

## 7.4 Simulation with misalignments

Two types of beam component misalignments were simulated to study their effects. One was with the target and all components downstream of it moved 0.5 cm to the west, shown in Figure 7.12. The other misalignment was with those components rotated 0.01 rad (0.57 degrees) around the vertical axis, as shown in Figure 7.13. To achieve the first type of misalignment, horizontal coordinates of the beam components from the target downstream are increased by 0.5 cm. To achieve the second type of misalignment, the elevation angle in the horizontal plane is increased by 0.01 rad. A longitudinal field of 0.1 mG was assumed in all beam components.

For the 0.5 cm misalignment to the west, the resulting PNCA is $(-6.3 \pm 3.4) \times 10^{-8}$ rad, which translates to $1.3 \times 10^{-8}$ rad/mm; For the 0.01 rad rotation to the east the resulting

PNCA is $(-23.8 \pm 3.8) \times 10^{-8}$ rad, which translates to $3.8 \times 10^{-7}$ rad/deg. Scattering in He was turned off to investigate the second misalignment type, and the resulting PNCA is $(2.3 \pm 3.1) \times 10^{-8}$ rad, which translates to less than $5.4 \times 10^{-8}$ rad/deg without scatter, compared to $3.8 \times 10^{-7}$ rad/deg with scatter. This indicates the neutron scatter with liquid He, when coupled with the misalignment, is responsible for the non-zero effect.

Our alignment is accurate to better than 2 mm for the translational misalignment, which causes an effect of $2.6 \times 10^{-8}$ rad. For the rotation misalignment, we are accurate to 0.05° with an effect of $1.9 \times 10^{-8}$ rad. So from the simulation the misalignments won't cause any systematic effects more than $3.2 \times 10^{-8}$ rad.

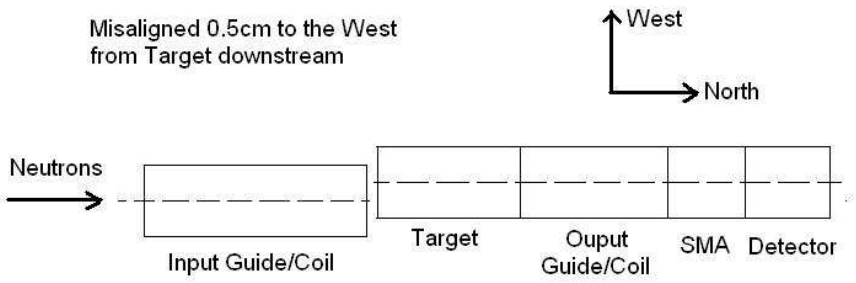


Figure 7.12: Top view of misalignment 0.5 cm to the west from target downstream.

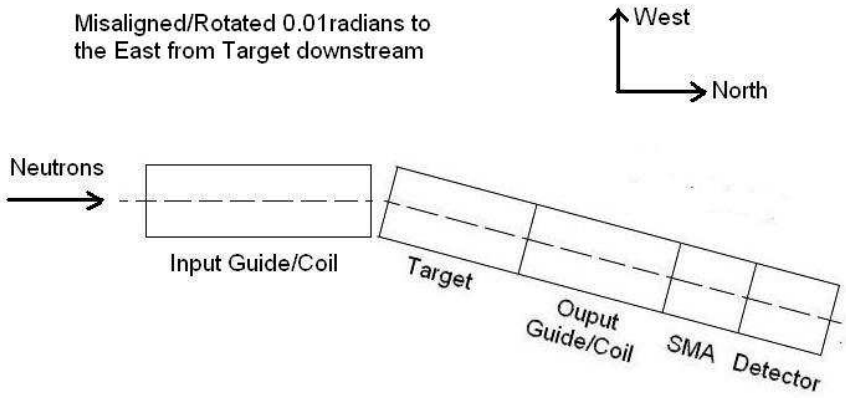


Figure 7.13: Top view of misalignment 0.01 rad to the east from target downstream.

## 7.5 Summary of errors

Table 7.2 shows the summary of experimental errors discussed in this chapter. The estimated sum of errors from multiplicative effects, extra measurement noise over statistics, and systematic effects with a 100 $\mu$G residual field is $5.8 \times 10^{-8}$ rad/m. The 3 types of measured systematic effects are not entirely independent from each other, so a straight sum was taken for the worse case scenario. The measurements put an upper bound of $1.3 \times 10^{-7}$ rad/m on the total systematic error. This is very good, considering the statistical error from our measurement is $8.3 \times 10^{-7}$ rad/m.

Table 7.2: Summary of experimental errors

| | Errors | Magnitude |
|---|---|---|
| Analytical calculation and estimation | | |
| Multiplicative effect | From polarization product | 5% of $\sqrt{N}$ |
| Measurement noise above $\sqrt{N}$ | Reactor fluctuation | Canceled as common mode noise in the 2 sub-beams |
| | Ion chamber detector electronic noise | 3.2% of $\sqrt{N}$ |
| Systematic effects (with 100 $\mu$G field) | Diamagnetism of liquid $^4$He | $2 \times 10^{-10}$ rad/m |
| | Optical potential of liquid $^4$He | $5 \times 10^{-9}$ rad/m |
| | Shift in neutron energy spectrum | $2.5 \times 10^{-8}$ rad/m |
| | Change of neutron path due to gravity or reflection | Less than $1 \times 10^{-10}$ rad/m |
| | Non-uniform polarization product coupled with small angle scattering | $1.3 \times 10^{-8}$ rad/m |
| | Sum | $3 \times 10^{-8}$ rad/m + 6% of $\sqrt{N}$ = $5.8 \times 10^{-8}$ rad/m |
| | | |
| Scaled from measurements | Large longitudinal B field | $4 \times 10^{-8}$ rad/m |
| | Large B field gradient | $3 \times 10^{-8}$ rad/m |
| | Polarization product non-uniformity | $6 \times 10^{-8}$ rad/m |
| | Sum | $1.3 \times 10^{-7}$ rad/m |

# Chapter 8

# Discussion

## 8.1 Final value and error budget

As discussed in Chapter 5 (Equation 5.29), the measured parity non-conserving (PNC) spin rotation of cold neutrons through a liquid $^4$He target is $(5.75 \pm 8.27) \times 10^{-7}$ radians per meter, where that uncertainty is the statistical error. Table 7.2 summarizes the systematic errors to be $5.8 \times 10^{-8}$ rad/m from analytical calculation and $1.3 \times 10^{-7}$ rad/m from measurements. The upper bound from measurements will be used as the systematic error for our experiment. The final value for the PNC neutron spin rotation in liquid $^4$He is

$$\phi_{PNC} = (5.8 \pm 8.3(stat) \pm 1.3(sys)) \times 10^{-7}\ rad/m \tag{8.1}$$

This is the most sensitive PNC spin rotation measurement to date.

Equation 8.1 indicates the statistical error is significantly larger than the systematic error. The measurement was limited by experimental conditions that caused a large portion of down time in the data-taking sequence. For every target state, the data-taking time was 300 seconds. But it took 300 to 350 seconds to drain and pump the liquid He to change target states. There was also a large amount of beam time when the apparatus became inoperable and needed to be fixed. Because of scheduling demands on NG6, the experiment

could not be extended to make up for the time lost to equipment problems. Section 8.3 will discuss the improvements for future measurements to reduce the statistical error.

## 8.2 Contribution of the measurement to understanding weak nucleon-nucleon (NN) physics

### 8.2.1 Theoretical predictions for PNC neutron spin rotation in $^4$He

Avishai predicted the $\vec{n}$ -$^4$He PNC spin rotation angle in 1982 with a non-relativistic hamiltonian and a simplified scattering amplitude dependence on the weak coupling strength. He predicted the PNC rotation angle $\phi_{PNC} \approx 7.3 \times 10^{-7}$ rad/m [27]. Avishai also predicted the neutron-electron weak interaction contribution to the $\vec{n}$-$^4$He spin rotation as $6 \times 10^{-8}$ rad/m, which is too small to discern from the nuclear contribution [27].

Dmitriev *et al.* calculated the spin rotation angle for transversely polarized neutrons in liquid $^4$He. That result was expressed in terms of a parity-violating NN interaction in the one-boson-exchange approximation, as derived by Desplanques, Donoghue and Holstein (DDH) [8]. Dmitriev and collaborators obtained an expression for the spin rotation in terms of the weak meson-exchange coupling coefficients described in Table 1.1 [28]:

$$\phi_{PNC}(\vec{n},\alpha) = -(0.97f_\pi + 0.22h^0_\omega - 0.22h^1_\omega + 0.32h^0_\rho - 0.11h^1_\rho)rad/m \qquad (8.2)$$

With the reasonable range and best values of the coefficients from DDH as shown in Table 8.1, Dmitriev *et al.* presented a result of $\phi_{PNC} = (-1 \pm 15) \times 10^{-7}$ rad/m. The DDH model uses the quark model and the SU(6) symmetry, and unifies the treatment of pion and vector meson vertices.

After DDH, more theoretical calculations have been done. In 1993 Kaplan and Savage estimated the strange-quark effects in the PNC pion-nucleon interactions [29]. In 1998

Table 8.1: Weak meson-exchange coupling coefficients predicted by Desplanques, Donoghue and Holstein [8]. Strengths are in units of the sum rule value $g_{\pi NN} = 3.8 \times 10^{-8}$.

| Meson-exchange coupling coefficient | DDH reasonable range | DDH best value |
|---|---|---|
| $f_\pi$ | 0 → 30 | 12 |
| $h_\rho^0$ | 30 → -81 | -30 |
| $h_\rho^1$ | -1 → 0 | -0.5 |
| $h_\rho^2$ | -20 → -29 | -25 |
| $h_\omega^0$ | 15 → -27 | -5 |
| $h_\omega^1$ | -5 → -2 | -3 |

Henley *et al.* used QCD sum rules to obtain the weak parity-violating pion-nucleon coupling constant $f_\pi$ [30]. Recent studies by Liu (2007) using the hybrid effective field theory (EFT) treatment found that the weak NN interaction at low energy, where $S$-$P$ transitions dominate, can be well specified by a set of six parameters [31].

### 8.2.2 Constraint from the measurement on weak meson-exchange coefficients

From the values of the weak meson-exchange coefficients in Table 8.1, the ranges of coefficients $h_\rho^1$ and $h_\omega^1$ are well defined and their strengths significantly smaller compared to the others. In addition, the expression of the PNC neutron spin rotation in liquid $^4$He in Equation 8.2 does not include $h_\rho^2$. It can be concluded that our measurement primarily puts constraints on coefficients $f_\pi$, $h_\rho^0$, and $h_\omega^0$.

Figure 8.1 plots the effective hadronic weak isoscalar ($h_\rho^0 + 0.6h_\omega^0$) and isovector ($f_\pi$) couplings. It shows the DDH reasonable range from Table 8.1 and the constraints on the coupling coefficients from our measurement in 2008 (Equation 8.1) and the 1996 measurement (Equation 1.1). The total uncertainty of the final result is reduced by 1/2 and we are significantly cutting into the DDH reasonable range. Our measurement is still consistent with the DDH reasonable range and its best value, but more data are needed to further constrain the coupling coefficients.

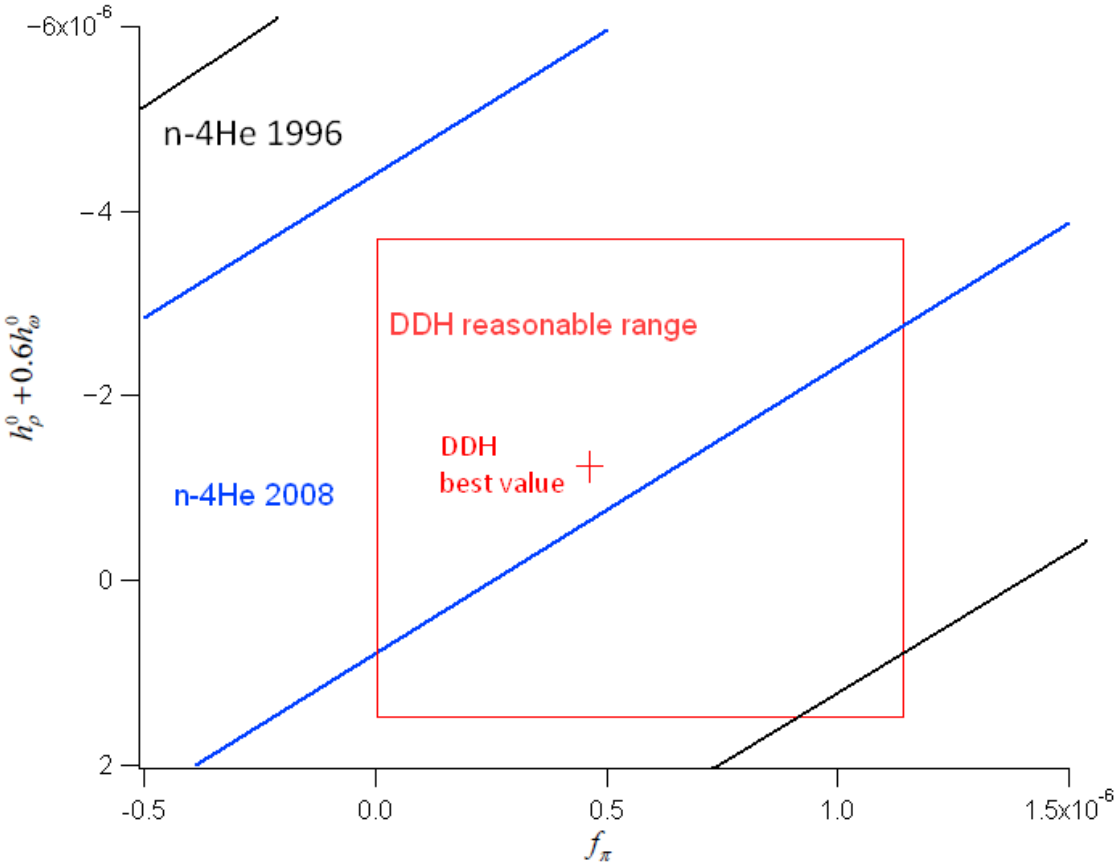


Figure 8.1: Experimental constraints on weak meson-exchange coupling coefficients from measurements of PNC neutron spin rotation in liquid $^4$He. Both measurements are consistent with each other and the DDH reasonable range.

## 8.3 Improvements for future measurements

### 8.3.1 Current experimental difficulties and possible remedies

Figure 8.2 shows how the 120 days of beam time at NIST were used. The time required to collect the production data is only about 1/6 of the total beam time. This was due to various experimental difficulties associated with the apparatus.

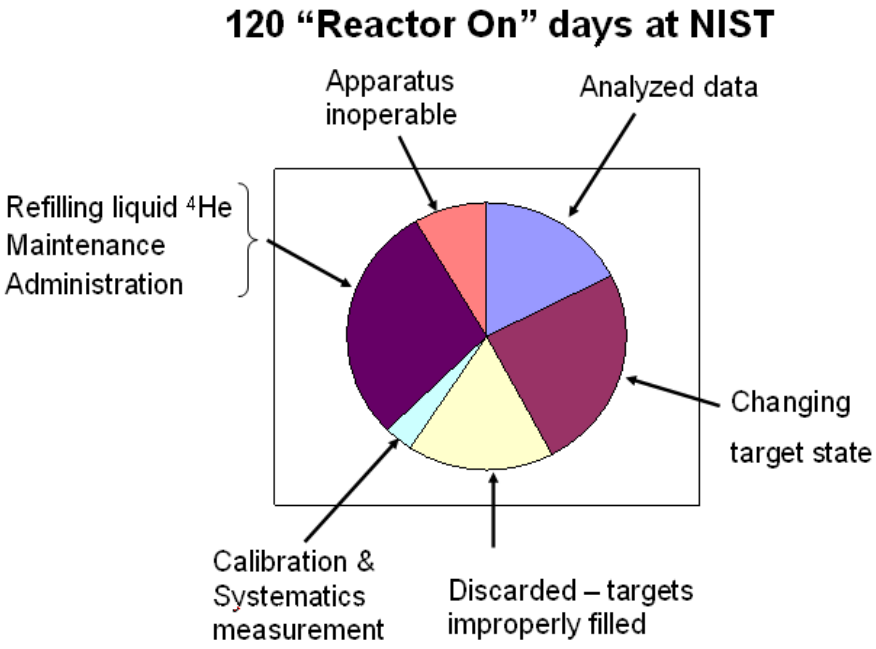


Figure 8.2: Use of the 120 days of beam time at NIST [32]. The time to collect the analyzed production data is about 22 days.

Changing target state and improperly filling targets cost us equal or more time than that used to take the analyzed data. To reduce the lengthy fill time when changing target state, the pump impeller would need to be in the vertical direction (pointing downwards), instead of the horizontal direction that was used in our experiment. With the impeller oriented vertically, the liquid pressure in the target insert will help the pumping. Additionally the impeller's lower position would enable it to pump liquid even when the level is low, and this

will reduce the amount of data discarded from improper filling caused by low liquid level in the target insert.

Another experimental difficulty is the high liquid $^4$He consumption. The high boil off rate in the target insert and the cryostat 4K volume not only required frequent refills (3 times a day) that reduced apparatus live time, but also increased the cost of the experiment. The heat load mostly comes from tubes into the target insert for liquid He filling, the pump drive shaft, and plumbing motion control strings. Increasing the heat conductivity between the tubes and the 4K and 77K heat shields will help reduce the heat load. Increasing the turbo pump speed and using shorter hoses will improve the cryostat main vacuum and also reduce boil-off rate.

### 8.3.2 Next generation neutron spin rotation at NIST

The NIST Center for Neutron Research (NCNR) expansion project is adding five cold neutron guides serving multiple experimental stations in the expanded guide hall, including a variety of fundamental physics stations requiring a large, high intensity end-position beam on guide NG-C. This provides an excellent opportunity for the next generation PNC n-$^4$He spin rotation measurements, as the new NG-C beam has a larger cross-sectional area (11 $\times$ 11 cm compared to 7 $\times$ 7 cm of NG-6) and $\sim$10 times more flux than the NG-6 beam line [37].

Simulation has shown a significant increase in neutron count rate with the new NG-C beam. As shown in Figure 8.3, this requires an upgrade of the target with a larger cross-sectional area and new larger input and output beam guides with larger m values. With an m value of 3 for the input and output guides, the neutron count rate is expected to plateau and using guides with higher m values would not be worth the added expense. If the new cryostat and target system are improved so that there is less down time, the next generation experiment could accumulate 100 times more neutrons and increase the sensitivity by an order of magnitude.

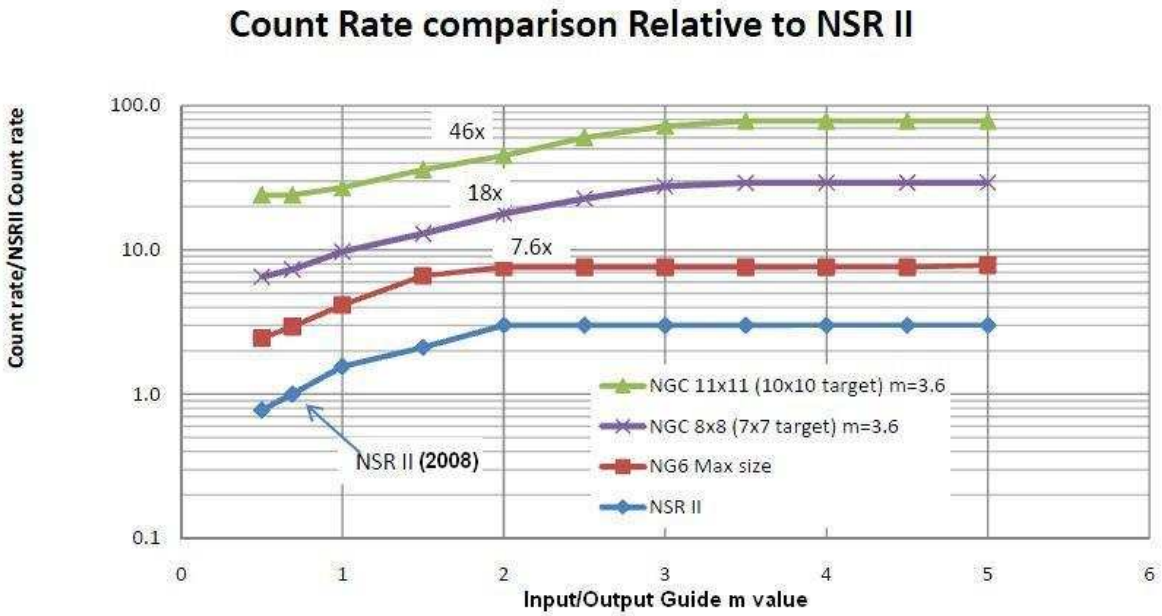


Figure 8.3: Count rate relative to the 2nd generation Neutron Spin Rotation (NSR II) measurement in 2008 with beam guide NG-6. NG-6 Max size uses the largest target that will fit with the NG-6 beam guide, 7 × 7 cm. A larger target (10 × 10 cm) will be needed to use the larger NG-C beam, as well as new input/output beam guides with larger m values to accommodate the larger NG-C m value of 3.6.

### 8.3.3 PNC neutron Spin rotation in liquid $^4$He at the Spallation Neutron Source (SNS)

The pulsed neutron beam at the SNS will have several advantages in future neutron spin rotation measurements.

First of all, the pulsed time structure of the beam will allow experiments to select neutrons with a narrow energy range. This will allow the $\pi$-coil field to precess the spin polarization of all neutrons by $\pi$ radians. At NIST, the $\pi$-coil field was set to precess neutrons at the average of their energy distribution, so it over-rotated the slower neutrons and under-rotated the faster neutrons. This resulted in a depolarization of the neutron beam and reduction of the polarization product. At SNS, the polarization product is expected to be close to 1, and that would automatically increase the measurement sensitivity by more than a factor of 1.6.

Secondly, the PNC spin rotation signal is independent of the neutron velocity for cold and thermal energies. However, the rotation due to residual magnetic fields is proportional to 1/v and is the most significant source of systematic error. The data can therefore be analyzed as a function of neutron time-of-flight to confirm the absence of magnetic field effects. Although a similar test is possible with the steady-state neutron source at NIST, it is much less sensitive, due to the broad range of neutron energies.

Lastly, a large number of polarized neutron beam instruments and sample environments produced large magnetic fields at NIST. They will not be present at the SNS, so the existing compensation system will be more than enough to suppress the fluctuating fields based on its performance at NIST.

### 8.3.4 PNC neutron spin rotation in liquid hydrogen

The np system is the most fundamental system to study weak nucleon-nucleon interactions and the theoretical calculation is the most direct. The isovector coupling coefficient $f_\pi$ is expected to dominate the PNC neutron spin rotation observable. The predicted spin rotation in parahydrogen is $(0-9)\times10^{-7}$ rad/m [33]. The neutron scattering in a parahydrogen target is larger than in helium, so that will reduce counting statistics. The absorption length is about 10 cm so a 15 cm long target is practical with a predicted PNC spin rotation of $(0-1.35)\times10^{-7}$ rad. The desirable measurement sensitivity would be $5\times10^{-8}$ rad.

# Bibliography

[1] T. D. Lee, C. N. Yang. *Question of parity conservation in weak interactions* Phys. Rev. 104, 254 - 258 (1956)

[2] C.S. Wu, E. Ambler, R. W. Hayward, D. D. Hoppes, and R. P. Hudson. *Experimental test of parity violation in beta decay* Physical Rev. 105, 1413 (1957)

[3] B. Heckel, N. F. Ramsey, K. Green, G. L. Greene, R. Gahler, O. Schaerpf, M. Forte, W. Dress, P. D. Miller, R. Golub, and J. Byrne. *A measurement of parity non-conserving neutron spin rotation in lead and tin* Physics letters B, 119B(4-6), 298-302 (1982)

[4] B. Heckel, M. Forte, O. Schaerpf, K. Green, G. L. Greene, N. F. Ramsey, J. Byrne, and J. M. Pendlebury. *Measurement of parity nonconserving neutron spin rotation in lanthanum* Physical Review C 29(6), 2389-2391 (1984)

[5] Diane M. Markoff. *Measurement of the Parity Nonconserving Spin-Rotation of Transmitted Cold Neutrons Through a Liquid Helium Target* Ph.D. Dissertation, University of Washington, 1997

[6] J.S. Nico et al., J. Res. Natl.Inst. Stand. Technol. 100, 137-144 (2005)

[7] Barry R. Holstein. *Weak Interactions in Nuclei* Princeton University Press, 1989

[8] B. Desplanques, J. F. Donoghue, and B. R. Holstein. *Unified treatment of the parity violationg nuclear force* Annals of Physics, 124(2), 449-495 (1980)

[9] E. G. Adelberger and W. C. Haxton. *Parity violation in the nucleon-nucleon interaction* Ann. Rev. Nucl. Part. Sci. 35: 501-558 (1985)

[10] F. Curtis Michel. *Parity nonconservation in nuclei* Physical Review, 133(2B), B329-349 (1964)

[11] L. Koester and A. Styerl. *Neutron Physics* Springer Verlag, 1977

[12] M. L. Goldberger and K. M. Watson. *Collision Theory* John Wiley, 1964

[13] D. J. Hughes. *Neutron Optics* Interscience Publishers, Inc., 1954

[14] D. J. Richardson, Robert Golub and Steve K. Lamoreaux. *Ultra-cold Neutrons* Adam Hilger, 1991

[15] Blayne R. Heckel. *Parity Non-Conserving Neutron Spin Rotation: The Tine Isotopes* PhD Thesis, Harvard University, 1981

[16] Christopher D. Bass. *Measurement of the Parity-Violating Spin-Rotation of Polarized Neutrons Propagating Through Liquid Helium* Ph.D. Dissertation, Indiana University, 2008

[17] Da Luo. *Measurement of the Parity Non-Conserving Spin Rotation of Cold Neutrons Through a Liquid Helium Target* Ph.D. Dissertation, Indiana University, 2009

[18] A.M. Micherdzinska et al., *Polarized neutron beam properties for measuring parity-violating spin rotation in liquid $^4He$* Nuclear Instruments and Methods in Physics Research, A. DOI: 10.1016/j.nima.2010.11.105 (2010)

[19] J. B. Hayter, J. Penfold, and W. G. Willaims. *Compact polarising Soller guides for cold neutrons* Journal of Physics E; Scientific Instruments, 11, 454-458 (1978)

[20] Y. Abe and N. Morishima, *Ultracold and cold neutron cross-sections of liquid helium at low temperatures down to 0.1 K* Nucl. Inst. and Meth. A, 459, 256 (2001)

[21] H.R. Glyde, *Neutron Scattering from Liquid* $^4$*He* J. of Low Temp. Phys., 87, 407 (1992)

[22] N.H. March and M.P. Tosi, *Atomic Dynamics in Liquids* John Wiley & Sons (1976)

[23] M. Schlapp et al., J. Phys. D: Appl. Phys. 37 2607 (2004)

[24] H.P. Mumm et al., Rev. Sci. Inst. 75, 5343 (2004)

[25] R.E. Glick, J. Phys. Chem. 65, 1552 (1961)

[26] H.S. Sommers et al., Phys. Rev. 97, 855 (1955)

[27] Y. Avishai, Physics Letters 112B(4,5), 311 (1982)

[28] V.F. Dmitriev et al., Physics Letters 125(1), 1 (1983)

[29] D.B. Kaplan and M.J. Savage, Nucl. Phys. A556, 653 (1993)

[30] E.M. Henley et al., Phys. Lett. B 367, 21 (1996)

[31] C.-P. Liu, Phys. Rev. C 75, 065501 (2007)

[32] H.E. Swanson, APS 2010 April meeting presentation, BAPS H8.00003

[33] Y. Avishai and P. Grange, J. Phys. G 10, L263 (1984)

[34] M.J. Ramsey-Musolf and S.A. Page, Ann. Rev. Nucl. Part. Sci. 56, 1(2006)

[35] S.-L. Zhu et. al., Nucl. Phys. A 748, 435 (2005)

[36] G.S. Danilov, Phys. Lett. 18, 40 (1965)

[37] J.C. Cook, Rev. Sci. Inst. 80, 023101 (2009)

[38] J. Als-Nielsen and O. Dietrich, Phys. Rev. 133, B925 (1964)